DIRECT COMPUTATIONS OF A SYNTHETIC JET ACTUATOR

A thesis Submitted for the degree of Doctor of Philosophy

by

Declan Hayes-McCoy

School of Engineering and Design, Brunel University

February 2012

LIST OF TABLES

4.1 Input parameters for the validation case...49

5.1 The computational cases of the axisymmetric simulations…..………......……...60

5.2 Input parameters for the jet optimised case………………...…………………...69

5.3 Velocity profiles for a half actuation cycle……………………………………...71

6.1 Input parameters for the 3*D* jet case…………..………………………......…...79

8.1 The computational cases of the 2*D* cross-flow simulations..............................133

LIST OF FIGURES

1. Schematic of a synthetic jet actuator........…………………………...….….……....3

3.1 Schematic of the physical problem of an axisymmetric synthetic jet...................40

3.2 Schematic of the physical problem of an planar synthetic jet………...................41

3.3 Waves entering and leaving the computational domain......................................43

4.1 Procedure for calculating the phase offset angle...50

4.2 Phase averaged *U* vs. phase angle after phase alignment....................................51

4.3 Time averaged *V* velocity along the x = 0.7874 line...52

4.4 Time averaged *U* velocity along the x = 0.7874 line...53

4.5 Phase averaged *V* velocity along the x = 0.7874 line at ϕ = 90°..........................54

4.6 Phase averaged *U* velocity along the x = 0.7874 line at ϕ = 90°.........................55

4.7 Phase averaged *V* velocity along the x = 0.7874 line at ϕ = 270°.......................55

4.8 Phase averaged *U* velocity along the x = 0.7874 line at ϕ = 270°.......................56

5.1 Streamwise centreline velocities at t = 80……………………………………......62

5.2 Momentum flux as a function of streamwise position for Case A-E....................65

5.3 Instantaneous vorticity contours at t = 80……………………………….……......67

5.4 Effect of Reynolds number: instantaneous vorticity contours at t = 80................68

5.5 Jet optimised case at t = 160………………………….…………………….........69

5.6 Instantaneous jet centreline velocity for a half actuator cycle…………...….........71

5.7 Time evolution of the vortex structures of the optimised case………....……......74

5.8 Centreline velocity history of the axisymmetric cases…..........…………………......75

6.1(a) Isometric view of the entire 3d flow-field……………………….……………....81

6.1(b) Partially rotated view of the flowfield with an enstrophy value of 1……….....81

6.1(c) Elevation of flowfield with an enstrophy value of 1……………….………......81

6.1(d) Partially rotated view of the flowfield with an enstrophy value of 0.5……......82

6.1(e) Elevation of flowfield with an enstrophy value of 0.5………….…………...82

6.1(f) Magnification of the vortex rings present with an enstrophy value of 0.5…......82

6.1(g) Partially rotated view of the flowfield with an enstrophy value of 0.25……....83

6.1(h) Elevation of flowfield with an enstrophy value of 0.1……………….…......83

6.1(i) Partially rotated view of the flowfield with an enstrophy value of 0.1……......83

6.2(a) Slices showing vortex rings present at x = 10……………….....................84

6.2(b) Slices showing vortex rings present at x = 15……………….....................84

6.3(a) z = 4.5 slice showing enstrophy of the fully developed jet case at t =165…....85

6.3(b) z = 5 slice showing enstrophy of the fully developed jet case at t =165……...85

6.3(c) z = 5.5 slice showing enstrophy of the fully developed jet case at t =165…....86

6.3(d) z = 6.0 slice showing enstrophy of the fully developed jet case at t =165…....86

6.3(e) z = 6.5 slice showing enstrophy of the fully developed jet case at t =165.........86

6.3(f) z = 7.0 slice showing enstrophy of the fully developed jet case at t =165…......87

6.3(g) z = 7.5 slice showing enstrophy of the fully developed jet case at t =165…....87

6.4(a) Jet centreline velocity, t = 62.5 to t = 68.75…………………….............89

6.4(b) Jet centreline velocity, t = 70.3125 to t = 75……………………...............90

6.4(c) Overall Jet centreline velocities, t = 62.5 to t = 75………….………….........90

6.5(a) Velocity vectors of the 3d jet evolution at t = 15……………………….....92

6.5(b) Velocity contours of the 3d jet evolution at t = 15…………...……….....92

6.5(c) Plan view of the velocity contours of the 3d jet evolution at t = 15...................92

6.6(a) Velocity vectors of the 3d jet evolution at t = 30……………………….....93

6.6(b) Velocity contours of the 3*d* jet evolution at $t = 30$……………………..…………....93

6.6(c) Plan view of the velocity contours of the 3*d* jet evolution at $t = 30$............ 93

6.7(a) Velocity vectors of the 3*d* jet evolution at $t = 50$……………………………......94

6.7(b) Velocity contours of the 3*d* jet evolution at $t = 50$……………………..…………....94

6.7(c) Plan view of the velocity contours of the 3*d* jet evolution at $t = 50$……………....94

6.8(a) Velocity vectors of the 3*d* jet evolution at $t = 70$……………………………......95

6.8(b) Velocity contours of the 3*d* jet evolution at $t = 70$……………………..…………....95

6.8(c) Plan view of the velocity contours of the 3*d* jet evolution at $t = 70$...................95

6.9(a) Velocity vectors of the 3*d* jet evolution at $t = 100$……………………………......96

6.9(b) Velocity contours of the 3*d* jet evolution at $t = 100$…..………………...……....96

6.9(c) Plan view of the velocity contours of the 3*d* jet evolution at $t = 100$.................96

6.10(a) Velocity vectors of the 3*d* jet evolution at $t = 120$…………………………......97

6.10(b) Velocity contours of the 3*d* jet evolution at $t = 120$…..………………...……..97

6.10(c) Plan view of the velocity contours of the 3*d* jet evolution at $t = 120$…..……..97

6.11(a) Velocity vectors of the 3*d* jet evolution at $t = 150$………………..………......98

6.11(b) Velocity contours of the 3*d* jet evolution at $t = 150$…..………………...……..98

6.11(c) Plan view of the velocity contours of the 3*d* jet evolution at $t = 150$…............98

6.12(a) Velocity vectors of the 3*d* jet evolution at $t = 165$…………………………......99

6.12(b) Velocity contours of the 3*d* jet evolution at $t = 165$…..………………...……..99

6.12(c) Plan view of the velocity contours of the 3*d* jet evolution at $t = 165$…............99

6.13 Non-dimensionalised Jet width………………………………………………101

6.14 Time averaged centreline velocity from $t = 50$ to $t = 165$……………………102

6.15(a) Cross-streamwise vector plot at $x = 10$ ……………………….................102

6.15(b) Cross-streamwise vector plot at $x = 15$ ……………………….................102

6.16 Perturbation case comparison at $t = 16$……………………………………105

6.17 Perturbation case comparison at $t = 50$……………………………………105

6.18 Perturbation case comparison at $t = 50$ (plan view)………………………….106

6.19 Perturbation case comparison, $x = 10$ slice at $t = 50$………………………….106

6.20 Perturbation case comparison, $x = 15$ slice at $t = 50$………………………….107

6.21 Perturbation case comparison, $x = 20$ slice at $t = 50$………………………….107

6.22 Perturbation comparison at $t = 70$…………………………………………108

6.23 Perturbation case comparison at $t = 70$, (plan view)……..…………………..108

6.24 Perturbation case comparison, $x = 10$ slice at $t = 70$………………………….109

6.25 Perturbation case comparison, $x = 15$ slice at $t = 70$………………………….109

6.26 Perturbation case comparison, $x = 20$ slice at $t = 70$………………………....110

6.27 DNS & NASA time averaged centreline velocity from $t = 50$ to $t = 165$........112

7.1 Jet centreline velocity at $t = 165$ of the 3*d* case……….......................……...115

7.2(a) Velocity vectors over one actuation cycle for the 3*d* and axisymmetric cases at $t = 62.5$……………………………………………………………117

7.2(b) Velocity vectors over one actuation cycle for the 3d and axisymmetric cases at $t = 64.0625$……..…………………………………………………117

7.2(c) Velocity vectors over one actuation cycle for the 3d and axisymmetric cases at $t = 65.625$…..…..……………………………………………………118

7.2(d) Velocity vectors over one actuation cycle for the 3d and axisymmetric cases at $t = 67.1875$....…..…………………………………………………118

7.2(e) Velocity vectors over one actuation cycle for the *3d* and axisymmetric cases at $t = 68.75$…....…..…………………………………………………118

6.1 7.2(f) Velocity vectors over one actuation cycle for the *3d* and axisymmetric cases at t = 70.3125....…..………………………………………………….119

7.2(g) Velocity vectors over one actuation cycle for the *3d* and axisymmetric cases at t = 71.875....…..……………………………………………………..119

7.2(h) Velocity vectors over one actuation cycle for the *3d* and axisymmetric cases at t = 73.4375....…..………………………………………………….119

7.2(i) Velocity vectors over one actuation cycle for the *3d* and axisymmetric cases at t = 75…....…..………………………………………….………...120

7.3(a) Time evolution of the vortical structures present in the 3*d* and axisymmetric cases at t = 30………………………………..........................……….121

7.3(b) Time evolution of the vortical structures present in the 3*d* and axisymmetric cases at t = 70……………………………………...……..............................122

7.3(c) Time evolution of the vortical structures present in the 3*d* and axisymmetric cases at t = 120………………………………..........................………..122

7.3(d) Time evolution of the vortical structures present in the 3*d* and axisymmetric cases at t = 165..……………………………………….............................123

7.4 Centreline velocity history of the axisymmetric and 3*d* cases……………….124

8.1 Vorticity contours of the planar case at t = 60...127

8.2 Vorticity contours with a cross-flow velocity of $v = 0.1u$...............................129

8.3 Vorticity contours with a cross-flow velocity of $v = 0.15u$.............................129

8.4 Vorticity contours with a cross-flow velocity of $v = 0.25u$.............................130

8.5 Cross-stream velocity profile for $v = 0.1u$..131

8.6 Cross-stream velocity profile for $v = 0.15u$..131

8.7 Cross-stream velocity profile for $v = 0.25u$..132

8.8 Vorticity contours of a synthetic jet in a cross-flow, indicating two vortex trajectories *St* = 0.04...135

8.8 Vorticity contours of a synthetic jet in a cross-flow indicating two vortex trajectories , *St* = 0.08...136

8.9 Vorticity contours of a synthetic jet in a cross-flow indicating two vortex trajectories , *St* = 0.04...136

NOMENCLATURE

NOTATION

A	amplitude of perturbation
e	internal energy per unit mass
f	$= \left(\frac{f^{*} r_{0}^{*}}{u_{x0}^{*}} \right)$, nondimensional frequency
f_0	pulsation frequency
f_1	external perturbation frequency
M	Mach number
p	pressure
Pr	Prandtl number
Re	Reynolds number
St	Strouhal number (non-dimensional frequency)
t	non-dimensional time
u	$= \left(\frac{u^{*}}{u_{x0}^{*}} \right)$, non-dimensional velocity component
u_x	axial velocity component of the axisymmetric case
u_r	radial velocity component of the axisymmetric case
u	axial velocity component of the 3*d* case
v, w	spanwise velocity components of the 3*d* case
W	non-dimensioanlised jet width
x, r	cylindrical coordinates in the axial and radial directions
x, y, z	cartesian coordinates in the axial and spanwise directions

GREEK SYMBOLS

φ	azimuthal angle
η	mapped radial direction
μ	dynamic viscosity
ρ	density
τ	viscous stress
ω	vorticity

SUPERSCRIPTS

$*$	dimensional quantities
‘	first derivative
‘’	second derivative

SUBSCRIPTS

0	domain inlet (jet nozzle exit) and centreline
j	grid index in the radial direction
x	axial direction for Cartesian & cylindrical coordinates
r	radial direction in the cylindrical coordinates
θ	azimuthal direction in the cylindrical coordinates
y , z	spanwise directions in the Cartesian coordinates

ABBREVIATIONS

2D	Two-Dimensional
3D	Three-Dimensional
CFD	Computational Fluid Dynamics
CFL	Courant-Friedrichs-Lewy
DNS	Direct Numerical Simulation
EXP	Experimental
IATA	International air Transport Association
LDA	Laser-Doppler Anemometry
LDV	Laser Doppler Velocimetry
LES	Large-Eddy Simulation
LODI	Local One-Dimensional Inviscid
MEMS	Micro-Electro-Mechanics Systems
NSCBC	Navier-Stokes Characteristic Boundary Condition
PIV	Particle Image Velocimetry
RANS	Reynolds Averaged Navier-Stokes
SA	Spalart-Allmaras
T-S	Tollmien-Schlichting
URANS	Unsteady Reynolds Averaged Navier-Stokes

ABSTRACT

Synthetic jet actuators have previously been defined as having potential use in both internal and external aerodynamic applications. The formation of a jet flow perpendicular to the surface of an aerofoil or in a duct of diffuser has a range of potential flow control benefits. These benefits can include both laminar to turbulent transition control, which is associated with a drag reduction in aerodynamic applications.

The formation and development of zero-net-mass-flux synthetic jets are investigated using highly accurate numerical methods associated with the methodology of Direct Numerical Simulation (DNS). Jet formation is characterised by an oscillating streamwise jet centreline velocity, showing net momentum flux away from the jet orifice. This momentum flux away from the orifice takes the form of a series of vortex structures, often referred to as a vortex train.

Numerical simulations of the synthetic jet actuator consist of a modified oscillating velocity profile applied to a wall boundary. The Reynolds numbers used vary from $85 \leq Re \leq 300$. A complete numerical study of both axisymmetric and fully three-dimensional jet flow is performed. A parametric axisymmetric simulation is carried out in order to study the formation criterion and evolution of zero-net-mass-flux synthetic jets under variations in actuator input parameters. From the results of these simulations the conditions necessary for the formation of the synthetic jet along with the input parameters that provide an optimal jet output are deduced. Jet optimisation is defined by the mass flow, vortex strength and longevity of the vortex train as it travels downstream. Further investigations are carried out on a fully three-dimensional DNS version of the optimised axisymmetric case. Comparisons between the jet evolution and flow-field structures present in both the axisymmetric and three-dimensional configurations are made.

This thesis examines the vortex structures, the jet centreline velocities along with time dependent and time averaged results in order to deduce and visualise the effects of the input parameters on the jet formation and performance. The results attained on altering the oscillation frequency of the jet actuator indicated that synthetic jets with zero mean velocity at the inflow behave significantly differently from jets with non-zero mean velocity at the inflow. A study into the evolution and formation of the train of vortex structures associated with the formation of a synthetic jet is performed. This study is accompanied with a series of time averaged results showing time dependent flow-field trends. The time history of the jet centreline velocity, showing the net momentum flux of the fluid away from the orifice of a fully developed synthetic jet, is analysed for both axisymmetric and three-dimensional cases. Differences in the fluid dynamics between the idealised axisymmetric configuration and the three-dimensional case have been identified, where three-dimensional effects are found to be important in the region near the jet nozzle exit.

The effect of a disturbance introduced into the three-dimensional simulation in order to break its inherent symmetry around the jet centreline is examined by altering the input frequency of the disturbance. It was found that the effect of this relatively minor disturbance had a major effect on the jet flow field in the region adjacent to the orifice. The effect of which was deemed to be caused by discontinuities in the surface of the jet orifice due to manufacturing tolerances. Although the effects of these disturbances on the jet flow-field are large, they seem to have been neglected from numerical simulations to date.

The effect of a synthetic jet on an imposed cross-streamwise velocity profile was examined. It was found that the synthetic jet flow-field resulted in a deformation of the velocity profile in the region downstream of the synthetic jet. It is suggested that this region of deformed flow could interact with coherent structures in a transitional boundary layer in order to delay flow transition to turbulence. The effect of varying the Strouhal number of a synthetic jet in a cross-flow is also analysed. It is clear from the results presented that, in the presence of a cross-flow velocity the Strouhal number effect on the synthetic jet flow field evolution, while dominant in a quiescent fluid is surpassed by the effect of the cross-flow.

TABLE OF CONTENTS

LIST OF TABLES i

LIST OF FIGURES ii

NOMENCLATURE viii

ABSTRACT xi

1. BACKGROUND 1

1.1 Introduction…………..……………………………………………………1

1.2 Transition Control……………………...…………………….................4

1.3 Receptivity & Boundary Layer Transition……………………....…………6

1.4 Experimental Studies…………………………………………….......11

1.5 Numerical Studies………………………………………….................14

1.6 The Synthetic Jet Actuator………………………………………………..16

1.7 Discussion…………………………………………………..................18

1.8 Motivation..……………………………...20

2. THE GOVERNING EQUATIONS...…………….……23

2.1 Introduction…………………………………………………………….23

2.2 Governing Equations of the Axisymmetric Case..24

2.3 Governing Equations of the Planar Case..26

2.4 Governing Equations of the Three Dimensional Case...................................27

2.5 Summary...29

3. NUMERICAL METHODS………………...30

3.1 Introduction……………………………………………………………….30

3.2 High Order Scheme for Time Advancement..31

3.3 Finite Difference Scheme for Spatial Discretisation....................................33

3.4 Grid Mapping…………………………………………………….............37

3.5 Boundary Conditions……………………………………......................…39

3.6 The Navier Stokes Characteristic Boundary Conditions...............................42

3.6.1 Inlet Velocity Profiles..45

3.7 Summary...47

4. CODE VALIDATION...48

4.1 Introduction…………………………………………………………..48

4.2 Results...50

4.3 Conclusion..56

5. AXISYMMETRIC SYNTHETIC JET SIMULATIONS…...................……58

5.1 Introduction……………………………………………………………….58

5.2 Simulation Details...59

5.2.1 Actuation Frequency……………………………………………....60

5.2.2 Reynolds Number Effects………………………………………....68

5.2.3 Optimal Jet Actuation Case……………………………………......69

5.3 Time Dependent Jet Evolution………………..……………….....................71

5.4 Jet Centreline Velocity History...73

5.5 Summary..75

6. THREE-DIMENSIONAL TEST CASES..……………………………..............78

6.1 Introduction…………………………………………………………….....78

6.2 Vortex Structures Present in the Flowfield…...…………………………......79

6.3 Jet Centreline Velocity…………………………………………………....88

6.4 Three-Dimensional Jet Evolution……………………………………….…...91

6.5 Time Averaged Flow-field Results...………………………………………100

6.6 Effects of Varying the Jet Perturbation……………………………………103

6.7 Summary……………………………………………………………….…...111

7. AXISYMMETRIC & 3D COMPARRISION……………………………………114

7.1 Introduction……………………………………………………………...114

7.2 Jet Centreline Velocity………………………………………………….…..115

7.3 Flow-field Evolution Over a Single Actuator Cycle……………………........116

7.4 Initial Jet Formation………………………...120

7.5 Summary…………………………………………………………….…...124

8. PLANAR SYNTHETIC JET SIMULATIONS............……………………........126

8.1 Introduction……………………………………………………………...126

8.2 Planar Case in Quiescent Air……………….............………….........127

8.3 Planar Case in a Cross-Flow.............................………………………......128

8.3.1 Cross-Flow Velocity Profile...130

8.4 Strouhal Number Variation of a Planar Synthetic Jet in a Cross-Flow.........132

8.5 Discussion..137

9. CONCLUSIONS & RECOMMENDATIONS……………………………………139

9.1 Conclusions…………………………………………………………...139

9.2 Recommendations for Further Work………………………………………142

9.2.1 Improved Actuator Modelling…………………………………...142

9.2.2 Other Types of Flow Control Actuator…………………………..143

9.2.3 Parametric Study on Perturbation effects.....................................143

9.2.4 Suitability of Synthetic Jets..144

BIBLIOGRAPHY…...…………………………………………………………...145

CHAPTER 1

BACKGROUND

1.1 INTRODUCTION

For many years, instability of laminar flow and the phenomenon of laminar - turbulent transition have been of constant interest due to their important relationship to drag. Potentially, there are many benefits from a successful control of turbulence, including improved combustion efficiency, suppression of flow related noise and reduction of the total wake drag and associated skin friction drag on a body moving through a viscous fluid. In terms of the skin friction drag, transition separates the low drag laminar flow region from the turbulent region where skin friction dramatically increases. Robert [1992] describes how, for a commercial transport aircraft, the skin friction drag represents about 50% of the total drag. Therefore, the potential to control or influence turbulence transition has the possibility to yield a net drag reduction and hence reduce the specific fuel consumption of an aircraft.

There have been a number of devices used in the application of transition control. In this thesis a single type of flow control actuator called a synthetic jet is simulated. Synthetic jet actuators are devices which provide a net momentum flux but zero net mass flux to a fluid within a working domain. The addition of this momentum flux to a moving fluid yields the possibility to control laminar to turbulent transition through the manipulation of a number of structures found in the flow field. Previous research has proven that these coherent structures are directly associated with the onset of turbulence transition. The ability of jet actuators to alter this turbulence production level, therefore yields the further possibility of skin-friction drag reduction, through the promotion of an extended region of laminar flow [Cater & Soria, 2002] [Rathnasingham, R. & Breuer, 2003] [Smith, B. L. & Glezer, A., 2002].

The synthetic jet actuator is an almost completely self contained device, requiring no external fluidic pipework. The only input required is a power source for the oscillating diaphragm. A generalised representation of this type of actuator produced by the Cattafesta *et al.* [2000] can be seen in figure 1. The ability of the synthetic jet to operate without the need of this fluidic pipework allows for a much greater flexibility in terms of the actuation control scheme used compared to many 'plumbed' systems such as continuous or pulsed jets. This is due to the fact that each individual actuator can be controlled completely independently in relation to neighbouring actuators in an array. Synthetic jets also yield benefits in terms of the overall size and mass of a complete array of actuators.

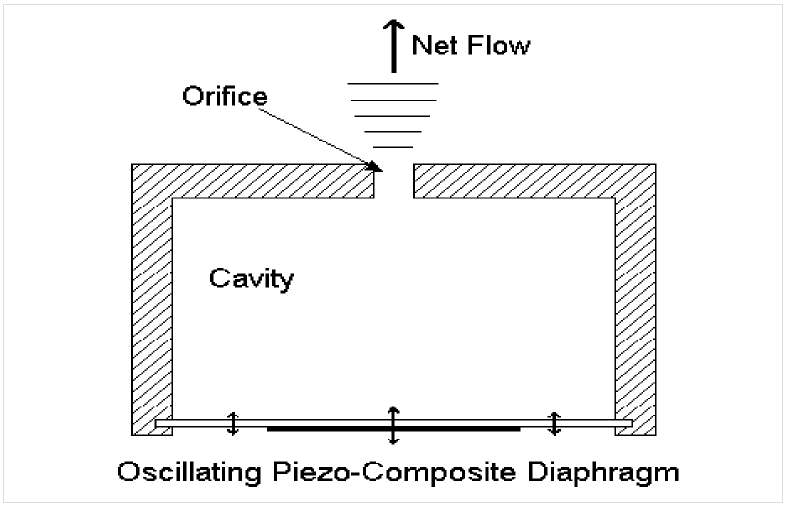

Fig. 1. Schematic of a synthetic jet actuator

As the synthetic jet can be used to directly apply momentum flux to the flow in an actively controlled manner, it has the advantage of being capable of adapting to various flow field variations. This method of active control of the actuator is known as targeted control, while methods not utilising a method of active feedback are known as passive control. Utilising this method of targeted control the actuator can be tuned to only applying a forcing to the flow when deemed necessary. In comparison, passive control methods, such as global suction over a large section of a wing surface, have enjoyed limited success, since they often expend more energy in applying the forcing than they save by successful flow control. Therefore, targeted control schemes have the advantageous ability to apply forcing only to the specific regions within the flow field that contribute directly or indirectly to high skin friction.

What follows is an overview of the relevant research in transition control in boundary layers along with a brief overview of some of the experimental and numerical work that has been carried out on flow control, specifically concentrating on synthetic jet actuators (Section 1.1 - Section 1.5). Focus is then placed on the physics of the synthetic jet actuator (Section 1.6). This provides a background to the current research project which is then finally introduced in Section 1.8.

1.2 Transition Control

The boundary layer generally exists in one of two states; laminar, where the fluid elements remain in a well-ordered non-intersecting layers (laminae), and turbulent, where fluid elements totally mix. Warhaft [1980] stated that, as a result of this mixing, the velocity gradient at the wall is higher than that seen in a laminar flow at the same Reynolds number. Therefore the shear stress at the wall is correspondingly larger, leading to an increase in skin friction drag.

Braslow [1999] noted that laminar flow is an inherently unstable condition that is easy to upset, therefore transition to turbulence may occur prematurely. This premature transition is a result of the amplification of disturbances emanating from various sources, such as surface roughness or free-stream turbulence. Many drag reduction strategies are therefore based around stabilising and prolonging this laminar boundary layer. Farrell & Loannou [1996] described how, the ultimate turbulence suppression is not the re-laminarisation of a turbulent boundary layer, but any successful attempt to preserve laminar flow by delaying the transition to turbulence.

Flow control devices utilised in promoting the longevity of laminar flow are not always strictly necessary. Laminar flow can be obtained passively over the leading edge of aerofoils with low sweep angles of less than 18 degrees. This is achieved by designing the surface cross-sectional contour of the aerofoil to produce a favourable pressure gradient from the leading edge towards the trailing edge. This passive flow control design is called natural laminar flow [Braslow, 1999]. It should be noted that any aerofoils designed to encompass natural laminar flow can still benefit from methods of active control in order to prolong the laminar flow region as the distance from the leading edge increases. Therefore, it can be noted that flow control devices such as synthetic jets can have possible applications in conjunction with other methods of laminar flow control.

Although the promotion of an extended region of laminar flow is the goal of many flow control techniques, laminar flow over an entire aerofoil surface may also not be desirable. A laminar boundary layer is more susceptible to flow separation in regions of an adverse pressure gradient than a turbulent boundary layer. This is explained by Subhasish & Tushar [2010] to be primarily due to the greater rate of energy and momentum exchange present within the turbulent boundary layer. Flow separation in regions such as close to the trailing edge of a wing leads to a large increase in wake drag due to the presence of a large turbulent wake associated with the separated flowfield. Separated flow also results in a decrease in the effectiveness of the lift produced by an aerofoil section, and also a reduction in the capability of any control surfaces located near the trailing edge. Therefore careful control of the transition point on a surface such as an aerofoil can result in a beneficial drag reduction while not having a detrimental effect on any control surfaces due to flow separation.

1.3 RECEPTIVITY & BOUNDARY LAYER TRANSITION

A number of different transition mechanisms of a laminar boundary layer to turbulence have been put forward over the years. What is clear is that the initial phase in the transition to turbulence is caused by a process known as 'receptivity'. Receptivity refers to the mechanism by which free-stream disturbances are internalised to generate boundary layer instability waves [King & Breuer, 2000]. The disturbances in the free-stream flow can take the form of free-stream turbulence or acoustic waves. Wũrz *et. al* [2003] examined the excitation and amplification of travelling waves known as Tollmein-Schlichting (T-S) waves in a boundary layer due to the scattering of an acoustic wave on a localised surface non-uniformity. Upon entering the boundary layer, a wide spectrum of disturbances such as acoustic waves are present. Many of these disturbances of smaller wavelength decay exponentially according to linear inviscid theory. Thus, the free-stream wavelength of the disturbance will be very long compared with the Tollmien-Schlichting waves. Goldstein & Hultgren [1989] noted that there are a number of different mechanisms by which the long wavelength free stream disturbances can be coupled to the relatively short wavelength of the Tollmien-Schlichting waves. These can involve direct scattering mechanisms associated with sudden changes in wall boundary conditions to the gradual wavelength reduction associated with viscous boundary layer growth. Choudhari & Kerschen [1990] investigated acoustic receptivity with three-dimensional (*3D)* roughness located at the wall boundary. They discovered a wedge shaped region of disturbance that formed several wavelengths downstream of the surface roughness.

Amplification of the T-S waves triggers the formation of a number of larger scale coherent structures in the laminar boundary layer, that have directly been associated with turbulent transition. Acarlar & Smith [1987] suggested that in the near-wall region the coherent structure that is generally considered being one of the most crucial elements in the production mechanism of turbulence is the hairpin vortex. At moderate flow speeds, hairpin vortices provide an example of an observable, organised transition process from a steady two dimensional laminar flow to unsteady three-dimensional turbulent flow. Smith [1984] put forward an initial formation process for hairpin vortices. He suggested that an initial vortex loop was formed due to a disturbance in the flowfield, such as that produced by the 'valley' nature of the T-S waves. Hon & Walker [1987 & 1991] further developed understanding of the formation process of hairpin vortices through experimental work involving injection of fluid into an essentially laminar boundary layer. They showed that the injected fluid interacts with the boundary layer to form an unstable shear layer which rolls up to form a single hairpin shaped vortex. These hairpin vortices are formed in the near wall region by the spreading and streamwise growth of the initial vortex loop noted by Smith [1984]. The vortex head that develops displays a self induced movement away from the wall. As the vortex moves away from the wall, it bends back on the shear flow, simultaneously the trailing portions of the vortex legs move downwards towards the wall forming the shape of a horseshoe or an arc. Symmetric hairpin vortices are formed from the stretching of these horseshoe shaped vortices by the wall shear layer, while Biot-Savart interactions amplify distortions already present within the vortex. Smith & Walker [1998] stated that lateral spreading of the initial disturbance is also present, causing subsidiary vortices, thus allowing the disturbance to spread and multiply in the spanwise direction. The combination of these influences results in the development of a hairpin shape. The portions of the hairpin vortices that move away from the wall are subject to extreme stretching by the local velocity of the flow, which increases through the boundary layer as the distance from the wall is increased. Yang, Meng & Sheng [2001] noted that low-momentum fluid is drawn away from the wall region and accumulated between the legs of the hairpin. This is due to the lateral pressure gradients created by the counter-rotating movement of the legs of the hairpin vortices.

The second coherent structure associated with turbulence transition and present in the near-wall region are the low-speed streaks. These structures are closely related to the hairpin vortices, and as noted by Yang, Meng & Sheng [2001], are generated and maintained owing to the low-momentum fluid region found between the legs. Hon & Walker [1987 & 1991] observed that, as a hairpin vortex moves downstream low-speed streaks were created near the surface beneath the hairpin vortex. For a symmetric hairpin vortex, where the legs are separated by a sufficient distance, two low-speed streaks are generally produced, one associated with each vortex leg. On the other hand, where the vortex legs are sufficiently close, the two streaks are seen to merge and give the appearance of a single streak.

It has been noted by Smith [1984] that a regeneration mechanism for streaks exists where a new vortex formed upstream overruns an existing streak, causing a refocusing or lateral movement of the streak. It is believed that the observed lateral motion of streaks is due to this regeneration mechanism. Smith [1984] also suggested that the coalescence of the stretched legs of multiple nested hairpin vortices is the mechanism by which low-speed streaks are preserved and redeveloped. This leads to streak lengths considerably longer than the observed streamwise length of any one hairpin vortex. As the streak is traced out in the wall-layer flow by a passing hairpin vortex, the leading edge of the streak moves downstream in phase with the vortex at a location below the leg and to the side where the vortex induced motion is away from the wall. This results in the lifting of the low-speed streaks away from the wall. Acarlar & Smith [1987] noted that the lifted up low-speed streaks appear to oscillate and are then rapidly carried away from the wall and downstream by a hairpin vortex.

Doligalski [1980] noted that a high-shear layer is generated at the interface between the low-momentum fluid lifted by a hairpin vortex and the higher speed outer boundary layer flow. A second high-shear layer is generated as the lower momentum fluid of the lifted low-speed evolves to a state where the streak is found riding over higher-speed fluid. This action results in the creation of strongly inflexional velocity profiles that are also associated with the creation of secondary vortices [Swearingen & Blackwelder, 1987]. It was suggested that this shear layer causes the formation of secondary vortices, which evolve and assume the shape of horseshoe or hairpin vortices. As these secondary hairpin vortices evolve, they begin to strongly interact and agglomerate with the original hairpins. The interaction of these secondary vortices with the hairpin vortices results in the generation of structures which suddenly eject away from the wall [Acarlar & Smith, 1987]. It is this interaction and the further amplification of these disturbances that results in the breakdown of the flow to turbulence.

Secondary vortices have also been noted to form on the outer edges of the legs of the hairpin vortices. Initially studies by Kim *et. al.* [1971] and Offen & Kline [1975], noted that the ejection of a low-speed streak is quickly followed by a sweep in which the high-speed fluid from upstream undercuts the erupting fluid. This ingestion of high-speed fluid towards the wall results in the local streamwise velocity exceeding the mean flow velocity. Acarlar & Smith [1987] described how these set of secondary vortices are formed by the distortion and intensification of vorticity by the inrush of fluid outboard of the counter-rotating legs of the original hairpin vortex. These secondary vortices entrain low momentum fluid away from the wall much in the same manner as the hairpin vortices, thus generating a further two low-speed regions on the outboard side of the legs of the hairpin.

The low-speed streaks are separated in the spanwise direction by the regions of high momentum fluid induced towards the wall during the sweep process known as high speed streaks. Swearengen & Blackwelder [1987] suggested that these high-speed streaks are of less importance than the low-speed streaks on the process of transition to turbulence due to their more stable velocity profile. However the high shear present between these high-speed streaks and the wall results in a high localised skin friction value.

There have been a number of varying interpretations of the effect of each of these coherent structures on the turbulence transition process, such as those put forward by [Smith *et al.* 1991] and [Swearingen & Blackwelder, 1987]. However it is generally agreed upon that the lift-off and subsequent break-down of low-speed streaks plays a key part in the transition to turbulence. The chaotic structures generated by the interaction of secondary vortices with the hairpin vortex can be noted to have many of the features of the 'bursting' process which is known to be one of the principal methods of turbulence regeneration in a turbulent boundary layer [Kim *et al.* 1971] [Offen & Kline, 1975].

The previous analysis of the effect of the low-speed streaks on the flow field suggest a number of possible methods of actuation of a synthetic jet actuator to achieve flow control. Firstly, a synthetic jet actuator can be used to prevent turbulent transition through the application of forcing beneath the low-speed streaks. The addition of fluid with a streamwise velocity less than that of the mean flow in the region of high-speed fluid beneath the low-speed streak can act to reduce the inflexional velocity profile of the boundary layer. This will in turn prevent the formation of the secondary vortices and thus promote the stabilisation of the low-speed streak.

Secondly, the application of forcing applied by a synthetic jet actuator beneath a high-speed streak can in theory reduce skin-friction drag. This can be accomplished by reducing the magnitude of the shear between the flow and the wall, through the injection of fluid with a low streamwise velocity component. This will have the effect of moving the high-speed streak away from the wall and reducing the skin friction component.

1.4 EXPERIMENTAL STUDIES

Experimental analysis into synthetic jet type of flow control devices can be traced back to early investigations into streaming motions by Meissner in 1926. His experimental work examined the attenuation of high frequency waves as they moved away from a wall boundary. The results obtained by Meissner [1926] into the dissipation of these high frequency waves, can be compared to the well documented features associated with the dissipation of the vortex rings formed by a synthetic jet actuator.

Gad-el-Hak and Blackwelder [1989] built on Gad-el-Hak and Hussain's [1986] previously utilised method of generating streaks and hairpin vortices by providing suction through a pair of holes. They successfully created a low-speed streak in a laminar boundary layer using this method. It was then demonstrated that the application of suction beneath this streak successfully stabilised the bursting phenomenon. Jacobson and Reynolds [1998] improved on this work by generating low-speed streaks in a laminar flow using a type of synthetic jet actuator. These low-speed streaks were successfully shown to cancel artificially generated high-speed streaks, thereby demonstrating the possible application of the synthetic jet actuator as a self contained flow control device. In a similar way, Ho and Tai [1996] reduced the shear stress underneath a stationary artificial high-speed streak using an oscillatory flap actuator.

Alongside the experimental work into the application of synthetic jet actuators, a number of experimental tests have been carried out into the detection of coherent structures in the flow field, an essential component in any targeted control scheme. The speed and accuracy of any detection method is also essential for the efficient implementation of any array based control scheme. Ho and Tai [1996] developed an array of micro-sensors capable of detecting the location of non-artificial streaks. This array of sensors was used in conjunction with their oscillatory flap actuator to accurately detect an artificially generated high-speed streak. Rathnasingham and Breuer [1997] improved on this method by developing a method using a linear feed-forward control algorithm based on the short term dynamics of the near-wall turbulent boundary layer to detect the randomly occurring streaks in a flow field. This control algorithm was then demonstrated to minimise turbulent fluctuations and wall pressure fluctuations when used in conjunction with an oscillatory actuator.

A number of experimental studies have been carried out to investigate the effect of a synthetic jet like flow field on coherent structures. However, a fully implemented synthetic jet actuator array with an accurate targeted control method is yet to be experimentally analysed. The experimental work carried out to date has mainly concentrated on the effect of actuation on individual artificially generated low-speed streaks and hairpin vortices. Smith & Glezer [2002] carried out a PIV analysis into the formation and evolution of synthetic jets, demonstrating the vortex train structure that is associated with synthetic jet flow fields. A worthwhile side note from the work of Smith & Glezer is a slight asymmetry found around the orifice centreline in their results. They went on to further examine this apparent abnormality and determined it to be due to a slight asymmetry present in the jet orifice itself, caused by manufacturing limitations. This potential symmetry of the synthetic jet flow field, (if manufacturing constraints are not considered) highlights the potential use of axisymmetric simulations for the correct prediction of a synthetic jet flow. This will be further examined later in this thesis.

1.5 NUMERICAL STUDIES

Many numerical simulations have been carried out into the use of synthetic jet like flow control devices and the modification of coherent structures. In this section three main areas have been concentrated on:

- The effect of the cavity modelling technique on the formation of a synthetic jet flow field.
- The control of artificially created coherent structures.
- The detection and modification of naturally occurring coherent structures.

Kral *et al.* [1997] have shown that a synthetic jet flow can be induced using sinusoidal oscillatory boundary conditions in place of the no-slip condition. In their numerical study the flow solution showed a good match with experiments, thus suggesting the suitability of this boundary type of boundary condition for the development of synthetic jet flow fields. This finding was also confirmed by Utturkar *et al.* [2003], who carried out a detailed two-dimensional computational study examining the sensitivity of the synthetic jet to the design of the jet cavity. They concluded that the design of the cavity had a limited effect on the jet flow field. Rizzetta *et al.* [1999] suggested a modified approach to representing the cavity flow. In their simulations they separately modelled the cavity and jet flow fields. The cavity flow was modelled by sinusoidally varying the position of the lower boundary. The velocity profile at the orifice was recorded once the cavity flow became periodic after a number of oscillation cycles.

This recorded orifice velocity profile was then applied to the external fluid domain in order to generate the synthetic jet flow field.

Numerical simulations of the control of coherent structures have enjoyed reasonable success, for example Choi *et al.* [1994] numerically demonstrated a drag reduction of 30% in a channel flow through selective blowing/suction applied at the wall. However numerical results such as this are highly idealised as they apply a forcing to an artificially generated coherent structure at a known spatial location. Catalano *et al.* [2002] demonstrated a net drag reduction in the flow over a cylinder using a modified velocity profile to model a synthetic jet actuator. Their numerical results used both 2*D* DNS methods and 3*D* LES, but did not directly model, or target any specific coherent structures.

As the turbulent transition process is intermittent in space and time, the effectiveness of pre-determined active control techniques can be limited. This is because forcing energy can be wasted in regions where it is not required, or indeed in regions where the outcome will be a net drag increase. Therefore the accurate spacial and temporal detection of coherent structures in a flow field, coupled with a targeted control scheme, can in theory lead to a net performance increase. Choi *et al.* [1994] utilised a DNS technique and a detection method for coherent structures based on sensors detecting velocity away from the wall to achieve a 6% reduction in skin friction drag using a selective suction or blowing method. This is a relatively low value compared to a reduction of 30% when control was globally applied, however, no comparison was carried out to the overall energy cost of applying a global control compared to their targeted reactive control method. Carlson and Lumley [1996] carried out a DNS investigation into the effect of a 'bump' type actuator on a naturally occurring high-speed streak. Their results demonstrated a successful detection and manipulation of the streak structure, while also going on to show the possible net skin-friction drag reduction benefit of flow injection beneath high-speed streaks.

1.6 THE SYNTHETIC JET ACTUATOR

Synthetic jets have been shown to be effective tools in flow control; applications have been shown by Uttukar & Holman *et. al.* [2003] to include, mixing enhancement, separation control and thrust vectoring. Its most common implementation is in the form of a piezoelectric disk bonded to a metal diaphragm, which is sealed to form a cavity. A jet orifice is enclosed on one side by this cavity, whose lower boundary is deformed in a periodic manner with the use of the oscillating diaphragm. As the diaphragm oscillates, fluid is periodically entrained and expelled from the orifice. Smith & Glezer [2002] proved that the interaction of the jet with the flow over the surface in which they are mounted can displace the local streamlines and induce a virtual change in the shape of the surface.

Tomar, Arnaud & Soria [2004] described a synthetic jet as a time averaged fluid motion generated by a sufficiently strong oscillatory flow at a sudden expansion. The synthetic jet, or the zero-net-mass-flux jet, has previously been proven to disrupt low-speed streaks [Smith & Walker, 1991], by either counteracting existing perturbations associated with turbulence production, or the stabilisation of the streak-like structures

[Schoppa & Hussain, 2000]. Smith & Glezer [2005] noted that the ability of synthetic jet actuators to be integrated into the flow surface without the need for external pipework and fluidic packaging makes them attractive tools for the control of both internal and external flows. Ritchie, Mujumdar & Seitzman [2000] demonstrated that synthetic jet actuators also have the advantage of a greater spreading rate than that of the equivalent continuous jet throughout the measured domain at the same time-averaged velocity, thus yielding a greater region of influence on the working domain.

Jet-like flows having complex spatial and temporal characteristics can be engineered in a quiescent medium by the convection and interactions of trains of discrete vortex structures [Glezer & Amitay, 2002]. The hydrodynamical impulse that is necessary to form each of these vortices is imparted at the flow boundary by the momentary discharge of slugs of fluid through an orifice [Glezer & Amitay, 2002]. The flow typically separates at the edge of the orifice and a vortex sheet is formed, which rolls into an isolated vortex that is subsequently convected away under its own self-induced velocity. These vortices ultimately break down and lose their coherence as they move away from the orifice.

The momentum flux away from the orifice is actually a train of vortex rings or vortex pairs being dispersed from the diaphragm during the compression stroke. A pair of these vortices can be seen parallel to each other on either side of the orifice in $2D$ & planar cases; each equal in magnitude but opposite in direction. If the self induced velocity is strong enough, this vortex pair is not ingested back into the orifice on the suction part of the cycle. Jet formation is governed by the Strouhal number of the flow and has also been defined by Uttukar & Holman *et. al.* [2003] as a mean outward velocity along the jet axis corresponding to the clear formation of shed vortices. The fluid is ejected from the cavity and separates from the orifice edge to form a coherent jet in the free-stream fluid.

Owing to the suction flow, the time averaged static pressure near the exit plane of a synthetic jet was noted by Glezer & Amitay [2002] to be typically lower than the ambient pressure, and both streamwise and transverse velocity components reversed their direction during the actuation cycle. Smith & Glezer [2005] noted that the time periodic reversal of the flow leads to the formation of a stagnation point on the centreline downstream of the orifice and confines the suction to a narrow domain near the exit plane.

1.7 DISCUSSION

There have been a number of theories explaining the cause of the high skin friction associated with a turbulent boundary layer. Although the exact cause is not certain, it is know that it is associated with the breakdown of coherent structures in the flow field that have been described in this chapter. Orlandi & Jimēnez [1994] suggested that this increased skin friction is a consequence of the non-linear nature of turbulence and is directly linked to both the low-speed and high-speed streaks present in the flow field. Alternatively, the inward rush of fluid during the 'sweep' phase could be responsible for high skin friction. Both these ideas were acknowledged by Jacobson and Reynolds [1998], who noted that, for the purposes of control, it was not essential to know the exact mechanism, since the target for control (the streaks and associated streamwise vortices) were the same in all cases.

Gad-el-Hak and Blackwelter [1989] suggested two possible mechanisms to influence the near-wall structure and thereby suppress the turbulent transition process. Firstly, to withdraw fluid from underneath the low-speed streaks to inhibit the ejection process. Swearingen & Blackwelder [1987] demonstrated that the disruption of the low-speed or high-speed streaks acts to reduce the spanwise variation of the streamwise velocity of a flow field. The creation of a region of low velocity fluid beneath the low speed streaks, acts to remove the inflexional velocity profile associated with the ejection process, thus stabilising the streak and preventing the formation of the secondary vortices associated with turbulence transition. The disruption of the secondary instability reduces skin-friction and delays the transition to turbulence. This control method is indirect as it aims to suppress an instability that will in turn create turbulence. The disadvantage of this method is that it directly increases the skin friction, as it draws high-momentum fluid towards the wall.

The second method suggested by Gad-el-Hak and Blackwelter was to inject fluid selectively under the high-speed regions. Application of the synthetic jet actuator to regions containing high-speed streaks can displace the local streamlines and induce a virtual change in the shape of the surface [Smith & Glezer, 2005]. This will have the effect of displacing the high-speed streaks away from the wall, thus directly reducing the wall shear. This method has the advantage of not directly increasing skin friction, a feature associated with the suction methods. This suggests that blowing is a more efficient method of drag reduction.

However, the low-speed streaks have been noted to have a more prominent role in the transition to turbulence. The stabilisation of these low-speed streaks may have an overall greater effect on the delay of turbulence production than targeting purely the high-speed streaks. Therefore, it is suggested that a combination of applying suction beneath the low-speed streaks and blowing beneath the high-speed streaks provides the optimum method of flow control.

The synthetic jet actuator has a possible role in applying a form of both types of drag reduction strategy suggested by Gad-el-Hak and Blackwelter. Application of the synthetic jet actuator in the regions below the low-speed streaks could be used as a method of transition control. The synthetic jet actuator acts to apply fluid with a low streamwise velocity component to the streamwise flow over an aerofoil.

1.8 MOTIVATION

It is of utmost importance to understand the flow field and formation criterion of synthetic jet actuators, since they have a potential to be utilised in flow control applications. However, our understanding of the true nature of the vortex structures present within a synthetic jet flow field is relatively limited due to the small length and time scales associated with a jet flow of this type.

The complexity of this type of flow field has previously been too pronounced for a complete computational treatment. Hence, a reduction of the computational burden of computationally modelling this type of flow field has been achieved through the use of a modelling approximation of the smallest length and time scales of the flow. These modelling techniques apply a time or ensemble averaging of the governing equations, thereby leading to a reduced capability to accurately calculate the unsteady flow field.

Experiments have also been utilised to complement numerical studies to a great extent. With the development of non-intrusive optical measurement techniques such as Laser-Doppler Anemometry (LDA), Laser-Doppler Velocimetry (LDV) and Particle Image Velocimetry (PIV), the measurements in complex flow fields have become increasingly possible. However, simultaneous measurement and processing of flow parameters with myriads of spatial and temporal scales is still an intimidating task for experimental tests.

Numerical simulation techniques yield the ability to investigate phenomena that are not easily examined using experimental techniques. Numerical approaches such as DNS for synthetic jet flows have become more feasible than before, mainly due to the rapid increase of computing power in recent years. DNS provides a method by which solutions of the governing equations to a high-degree of accuracy can be achieved for a wide variety of problems of technological and academic importance. DNS methods provide a tool by with which the flow unsteadiness and vortex structures produced by the synthetic jet can be accurately predicted.

A DNS methodology utilising highly accurate numerical methods to resolve all the length and time scales is used in this thesis. The first objective of this analysis was to quantitatively analyse the formation criterion for a Synthetic jet flow field. These criterion have generally been ignored in previous numerical analysis, with the concentration being placed upon low fidelity RANS analysis of a synthetic jet flow in a cross-flow. In this thesis a computational analysis of the flow field produced by a synthetic jet actuator in axisymmetric, planar and 3*D* domains is conducted. The axisymmetric & planar cases provide the computational advantage of using much less computational resources than fully 3*D* simulations, hence the formation criterion is established for the axisymmetric case.

Although the axisymmetric analysis provides a method by which the formation criterion of a synthetic jet flow field in a quiescent medium can be determined, the vortex stretching and interaction cannot be adequately predicted due to the absence of cross-streamwise vorticity. A second objective of the study is therefore to assess the limitations of both these axisymmetric simulations and previous *2D* numerical analysis of synthetic jets. Therefore, a comparative study of axisymmetric and fully 3*D* simulations has also been performed using identical input parameters, therefore allowing the 3*D* effects on the flow field to be analysed in isolation.

Finally, a planar *2D* analysis into the effects of a cross-flow velocity profile on the synthetic jet flow field has also been analysed. The aim of this analysis is to investigate if the optimum evolution parameters for a synthetic jet in a quiescent medium also apply to a synthetic jet in a cross-flow. The analysis of a synthetic jet in a cross-flow will also give insights into the applicability of synthetic jets as flow control devices. This will demonstrate a potential method of transition control such as described in chapter 1.2.

CHAPTER 2

THE GOVERNING EQUATIONS

2.1 INTRODUCTION

The governing equations used for the axisymmetric, 2*D* and 3*D* configurations are based on the conservation laws of mass, momentum and energy. There are three independent variables dealing with the *x, r* axisymmetric spatial coordinate system; three for the *x, y* planar coordinate system and four independent variables dealing with the *x, y & z* spatial coordinate system. In all three cases the time, *t* is the final independent variable. There are also four dependent variables for the axisymmetric and planar cases, and five dependent variables for the 3*D* case. These dependent variables are as follows: the pressure *p,* density ρ and three components of the velocity vector; *u, v* and the *w* component for the 3*D* case. Other non-dimensional quantities used in the formulation of the governing equations are: ρ , density; p , pressure; μ , viscosity; M , Mach number; Pr , Prandtl number and Re , Reynolds number.

2.2 GOVERNING EQUATIONS FOR THE AXISYMMETRIC CASE

The computational domain encompasses a cross-sectional slice of the axisymmetric jet. As symmetry conditions are imposed on the jet centreline the spanwise extent of the domain can be reduced by 50%. A cylindrical coordinate system is used to define the spatial location of all points within the domain. The coordinate system is represented as: (x, r, θ), where x is in the streamwise direction of the jet. The conservation laws for mass and momentum in the case of the axisymmetric jet are defined in Equations 2.1 – 2.6. This form of the conservation laws was defined by Anderson, [1995] in a non-dimensionalised vector form as,

$$\frac{\partial \mathbf{Q}}{\partial t} = -\frac{\partial \mathbf{E}}{\partial x} - \frac{1}{r}\frac{\partial (\mathbf{F} r)}{\partial r} - \mathbf{G} \tag{2.1}$$

where the vectors $\mathbf{Q}$, $\mathbf{E}$, $\mathbf{F}$ and $\mathbf{G}$ are defined as:

$$\mathbf{Q} = \begin{pmatrix} \rho \\ \rho\, u_x \\ \rho\, u_r \end{pmatrix} \tag{2.2}$$

$$\mathbf{E} = \begin{bmatrix} \rho\, u_x \\ \rho\, u_x^2 + p - \tau_{xx} \\ \rho\, u_x u_r - \tau_{xr} \end{bmatrix} \tag{2.3}$$

$$\mathbf{F} = \begin{bmatrix} \rho\, u_r \\ \rho\, u_x u_r - \tau_{xr} \\ \rho\, u_r^2 + p - \tau_{rr} \end{bmatrix} \tag{2.4}$$

$$\mathbf{G} = \begin{pmatrix} 0 \\ 0 \\ \dfrac{-p + \tau_{\theta\theta}}{r} \end{pmatrix} \tag{2.5}$$

In the case of the axisymmetric jet, the mathematical model is adjusted to account for the jet centreline, thus allowing for an exact application of the symmetry conditions. The governing equations at the centreline have been put into a special form developed by Jiang & Luo, [2000] and further extended by Jiang *et al.* [2004]. This formulation of the governing equations circumvents the singularity which usually occurs at the centreline of an axisymmetric simulation. The new set of governing equations at the jet centreline is expressed in a vector form as:

$$\frac{\partial \mathbf{Q}}{\partial t} = -\frac{\partial \mathbf{E}}{\partial x} - \frac{\partial \mathbf{F}}{\partial r} - \frac{\partial \mathbf{H}}{\partial r} \tag{2.6}$$

where the vector $\mathbf{H}$ is defined as:

$$\mathbf{H} = \begin{bmatrix} \rho u_r \\ \rho u_x u_r - \tau_{xr} \\ \rho u_r^2 - \tau_{rr} + \tau_{\theta\theta} \end{bmatrix} \tag{2.7}$$

In equations (2.3)-(2.5) and (2.7), the viscous stress components can be defined as

:

$$\tau_{xx} = -\frac{2}{3}\frac{\mu}{\mathrm{Re}}\left(-2\frac{\partial u_x}{\partial x} + \frac{\partial u_r}{\partial r} + \frac{u_r}{r}\right), \tag{2.8}$$

$$\tau_{rr} = -\frac{2}{3}\frac{\mu}{\mathrm{Re}}\left(\frac{\partial u_x}{\partial x} - 2\frac{\partial u_r}{\partial r} + \frac{u_r}{r}\right), \tag{2.9}$$

$$\tau_{\theta\theta} = -\frac{2}{3}\frac{\mu}{\mathrm{Re}}\left(\frac{\partial u_x}{\partial x} + \frac{\partial u_r}{\partial r} - 2\frac{u_r}{r}\right), \tag{2.10}$$

$$\tau_{xr} = \frac{\mu}{\mathrm{Re}}\left(\frac{\partial u_r}{\partial x} + \frac{\partial u_x}{\partial r}\right). \tag{2.11}$$

2.3 GOVERNING EQUATIONS FOR THE PLANAR CASE

For the simulation of the planar case the computational domain is formed by a two-dimensional Cartesian coordinate system (*x, y*). The governing equations are written as described by Anderson [1995]:

$$\frac{\partial \mathbf{Q}}{\partial t} = -\frac{\partial \mathbf{E}}{\partial x} - \frac{\partial \mathbf{F}}{\partial y} \tag{2.12}$$

where the vectors $\mathbf{Q}$, $\mathbf{E}$, $\mathbf{F}$ and S are defined as:

$$\mathbf{Q} = \begin{pmatrix} \rho \\ \rho\, u_x \\ \rho\, u_y \\ E_T \end{pmatrix} \tag{2.13}$$

$$\mathbf{E} = \begin{bmatrix} \rho\, u_x \\ \rho\, u_x^2 + p - \tau_{xx} \\ \rho\, u_x v_y - \tau_{xy} \\ (E_T + p)u_x - u_x\tau_{xx} - v_y\tau_{xy} \end{bmatrix} \tag{2.14}$$

$$\mathbf{F} = \begin{bmatrix} \rho\, u_y \\ \rho\, u_x v_y - \tau_{xy} \\ \rho\, v_y^2 + p - \tau_{yy} \\ (E_T + p)u_x - u_x\tau_{xx} - v_y\tau_{xy} \end{bmatrix} \tag{2.15}$$

In equations (2.13)-(2.15), the constitutive relations for viscous stress components are:

$$\tau_{xx} = -\frac{2}{3}\frac{\mu}{\mathrm{Re}}\left(-2\frac{\partial u_x}{\partial x} + \frac{\partial v_y}{\partial y}\right), \tag{2.16}$$

$$\tau_{yy} = -\frac{2}{3}\frac{\mu}{\mathrm{Re}}\left(\frac{\partial u_x}{\partial x} - 2\frac{\partial v_y}{\partial y}\right), \tag{2.17}$$

$$\tau_{xy} = \frac{\mu}{\mathrm{Re}}\left(\frac{\partial v_y}{\partial x} + \frac{\partial u_x}{\partial y}\right) \tag{2.18}$$

2.4 GOVERNING EQUATIONS FOR THE THREE DIMENSIONAL CASE

The 3*D* case utilises a Cartesian coordinate system to describe the working domain. The coordinate system is described by: *(x, y, z*), where the *x* axis is along the streamwise direction for the jet and the jet orifice is contained in the *y z* plane. The major reference quantities used are the same as those used in the axisymmetric simulations. The non-dimensional conservation laws for mass and momentum can be written in the following vector form:

$$\frac{\partial \mathbf{U}}{\partial t} + \frac{\partial \mathbf{R}}{\partial x} + \frac{\partial \mathbf{S}}{\partial y} + \frac{\partial \mathbf{T}}{\partial z} = 0, \tag{2.19}$$

where the vectors $\mathbf{U}$, $\mathbf{R}$, $\mathbf{S}$ and $\mathbf{T}$ are defined as:

$$\mathbf{U} = \begin{pmatrix} \rho \\ \rho\, u \\ \rho\, v \\ \rho\, w \end{pmatrix}, \tag{2.20}$$

$$\mathbf{R} = \begin{bmatrix} \rho\, u \\ \rho\, u^2 + p - \tau_{xx} \\ \rho\, uv - \tau_{xy} \\ \rho\, uw - \tau_{xz} \end{bmatrix}, \tag{2.21}$$

$$\mathbf{S} = \begin{bmatrix} \rho\, v \\ \rho\, uv - \tau_{xy} \\ \rho\, v^2 + p - \tau_{yy} \\ \rho\, uw - \tau_{yz} \end{bmatrix}, \tag{2.22}$$

$$\mathbf{T} = \begin{bmatrix} \rho\, w \\ \rho\, uw - \tau_{xz} \\ \rho\, vw - \tau_{yz} \\ \rho\, w^2 + p - \tau_{zz} \end{bmatrix}. \tag{2.23}$$

The viscous stress tensor components are:

$$\tau_{xx} = -\frac{2}{3}\frac{\mu}{\mathrm{Re}}\left(-2\frac{\partial u}{\partial x} + \frac{\partial v}{\partial y} + \frac{\partial w}{\partial z}\right), \tag{2.24}$$

$$\tau_{yy} = -\frac{2}{3}\frac{\mu}{\mathrm{Re}}\left(\frac{\partial u}{\partial x} - 2\frac{\partial v}{\partial y} + \frac{\partial w}{\partial z}\right), \tag{2.25}$$

$$\tau_{zz} = -\frac{2}{3}\frac{\mu}{\mathrm{Re}}\left(\frac{\partial u}{\partial x} - 2\frac{\partial v}{\partial y} + \frac{\partial w}{\partial z}\right), \tag{2.26}$$

$$\tau_{xy} = \frac{\mu}{\mathrm{Re}}\left(\frac{\partial v}{\partial x} + \frac{\partial u}{\partial y}\right), \tag{2.27}$$

$$\tau_{xz} = \frac{\mu}{\mathrm{Re}}\left(\frac{\partial w}{\partial x} + \frac{\partial u}{\partial z}\right), \tag{2.28}$$

$$\tau_{yz} = \frac{\mu}{\mathrm{Re}}\left(\frac{\partial w}{\partial y} + \frac{\partial v}{\partial z}\right). \tag{2.29}$$

2.5 SUMMARY

In this chapter the governing equations for the synthetic jet have been presented for the axisymmetric, *2D* planar and *3D* configurations. The conservation laws for mass and momentum have been introduced in a non-dimensional vector form.

CHAPTER 3

NUMERICAL METHODS

3.1 INTRODUCTION

Due to the small length-scales of the flow features associated with synthetic jets, typical Reynolds-averaged Navier-Stokes (RANS) methods do not provide sufficient detail to accurately represent the flow. This is due to the inherent inaccuracies produced by the time averaging of the governing equations by RANS techniques.

The DNS code used for this work has a sixth-order numerical accuracy for the spatial differentiation, which is performed by using a sixth-order order compact (Padé) finite difference scheme for evaluation of the spatial derivatives in all of the three directions [Jiang *et al*., 2006], [Lele, 1992]. The finite-difference scheme used allows for the use of a number of different boundary conditions, as described in Section 3.5 while retaining a high level of accuracy. It is sixth-order at all points within the domain, with the exception of a fourth-order accuracy at the points next to the boundary, and of third-order at the boundary. Compact finite differencing is utilised to attain the sixth-order accuracy within the domain. This Padé 3/4/6 scheme is fully described in Lele's journal document on compact finite difference schemes [Lele, 1992].

3.2 HIGH ORDER SCHEME FOR TIME ADVANCEMENT

A 3rd order Runge-Kutta scheme, as defined by Williamson [1980] is used for temporal integration of the governing equations, thus avoiding the accumulation of numerical errors over time. The main reference quantities used to normalise the equations are the maximum velocity in the streamwise direction at the location of the jet nozzle exit (domain inlet), the jet nozzle diameter, the ambient density and viscosity.

The solutions to the left hand side of the governing equations are given in Equations (2.2-2.5), (2.12-2.15) and (2.19-2.23). These solutions are integrated forwards in time using the three step compact-storage 3rd order fully explicit Runge-Kutta scheme [Williamson, 1980]. This type of scheme utilises only two memory locations for each time dependent variable and each time derivative per sub-step. Full details for the scheme can be found in Wray's journal paper [1986]. At the two memory locations the solution variables Q_1 and Q_2 are updated simultaneously as described by Sandham and Reynolds, [1989].

$$Q_1^{new} = a_1.R(Q)_1^{old}.\Delta t + Q_2^{old}, \qquad Q_2^{new} = a_2.R(Q)_1^{old}.\Delta t + Q_2^{old} \tag{3.1}$$

In Equation (3.1) two constants (a_1, a_2) are given fixed values corresponding to the solution sub step. These values are (0.66, 0.25) for the first sub step; (0.416, 0.15) for the second sub step, and; (0.6, 0.6) for the third sub step. At the start of each complete time step, Q_1 and Q_2 are equal. The data in Q_1 is used to compute the right hand side $R(Q)_1$ of equations (2.1), (2.6), (2.12) and (2.19). The value computed for $R(Q)_1$ is used to update the value of Q_1 from the previous time step. Equation (3.1) is then used to update Q_1 and Q_2 .

In equation (3.1), the time step is defined as Δt. This value is limited by the Courant-Friedrichs-Lewy (CFL) condition in order to maintain the stability of the solution. For the purposes of advancing the time step, the grid spacing in the streamwise direction is defined by: $\Delta x = L_x / N_x$. The same method is also used to define the spacing in both the Δy and Δz directions. The time-step can therefore be defined as:

$$\Delta t = \frac{CFL}{D_c + D_\mu} \tag{3.2}$$

where D_c and D_μ , in the *3D* configuration are given by:

$$D_c = \pi c\left(\frac{1}{\Delta x} + \frac{1}{\Delta y} + \frac{1}{\Delta z}\right) + \pi\left(\frac{|u|}{\Delta x} + \frac{|v|}{\Delta v} + \frac{|w|}{\Delta z}\right), \tag{3.3}$$

$$D_\mu = \frac{\pi^2 \frac{\mu}{\rho}}{(\gamma - 1) M^2 Re Pr}\left(\frac{1}{\Delta x^2} + \frac{1}{\Delta v^2} + \frac{1}{\Delta z^2}\right), \tag{3.4}$$

where the grid spacing in each of the Cartesian coordinate directions is defined by $\Delta x, \Delta y$ and Δz. The non dimensional speed of sound is defined as *c,* which can be expanded as shown in Equation (3.5).

$$c = \sqrt{\gamma\left(\gamma - 1\right)\left[\frac{e}{\rho} - \frac{1}{2}\left(u^2 + v^2 + w^2\right)\right]}.$$

(3.5)

By neglecting the *z* direction grid spacing and velocity terms involving *Δz* and *w* Equations (3.3), (3.4) and (3.5) can be easily adjusted for *2D* configurations

3.3 Finite Difference Scheme for Spatial Discretisation

A 6th order compact (Páde) finite difference scheme is used to achieve the spatial differentiation [Lele, 1992]. For the axisymmetric case symmetry conditions are applied to both the primitive variables and their first and second derivatives in the radial direction [Jiang, 2000]. This allows the Páde scheme to be extended to achieve the 6th order accuracy at the jet centreline.

For a variable *ΦJ* (where *J* defines a grid point in the radial direction), this Páde finite difference scheme can be written in the following form for the first and second derivatives.

$$\Phi'_{j-1} + a\Phi'_{j+1} = b\frac{\Phi_{j+1} - \Phi_{j-1}}{2\Delta n} + c\frac{\Phi_{j+2} - \Phi_{j-2}}{4\Delta n}, \tag{3.6}$$

where the constants *a, b* and *c* are defined as follows:

$$b = \frac{2 + 4a}{3} \qquad c = \frac{4 - a}{3}$$

(3.7)

The constant *a* defines the order of the scheme. For the first derivative this value is:

$a = 4.0$ *fourth-order,*

$a = 3.0$ *sixth-order.*

In the case of the 2nd derivative, the Páde 3/4/6 scheme can be written as:

$$\Phi''_{j-1} + a\Phi''_{j} + \Phi''_{j+1} = b\frac{\Phi_{j+1} - 2\Phi_{j} + \Phi_{j-1}}{\Delta n^2} + c\frac{\Phi_{j+2} - 2\Phi_{j} + \Phi_{j-2}}{4\Delta n^2} \tag{3.8}$$

where *b* & *c* are defined as:

$$b = \frac{4a-4}{3} \qquad c = \frac{10-a}{3}; \tag{3.9}$$

The constant *a* defines the order of the scheme for the second derivative as:

$a = 10.0$ *fourth-order*

$a = 5.5$ *sixth-order*

In equation 3.6 and equation 3.8, Δn is the mapped grid distance in the y (or in the r direction in the axisymmetric case). Φ can be any variable in the solution vector Q defined in equation 2.2 & equation 2.13 for the axisymmetric and planar cases. In the 3D case Φ can be a solution of the vector U defined in equation 2.20. The tridiagonal system of equations can be solved using a form of Gaussian elimination known as the Thomas algorithm [Conte & de Boor, 1972].

In the axisymmetric configuration, the condition applied to the symmetry boundary at the centreline of the jet is as follows:

$$\frac{\partial u}{\partial r}\Big|_{r=0} = 0 \tag{3.10}$$

Variables are mirrored about the jet centreline by applying a symmetry boundary condition to the *-r* components of pressure and velocity in the governing equations. This symmetry condition is also applied to the first and second derivatives of both components. Variables in the governing equations such as density do not undergo a sign change across the symmetry boundary.

The Páde 3/4/6 scheme includes a new set of tri-diagonal matrices to achieve the full 6th order accuracy at the symmetry boundary. A symmetry boundary located at $r = 1$ for the first derivative at $j = 1$ will yield:

$$\Rightarrow\ a\phi_1' + 0a\phi_2' = 0, \qquad \begin{matrix} \phi_0 = \phi_2, & \phi_{-1} = \phi_3, & \phi_0' = -\phi_2', \\ \dots & \dots & \dots \end{matrix} \tag{3.11}$$

$$\Rightarrow\ a\phi_1' + 2\phi_2' = b\frac{\phi_2}{\Delta n} + c\frac{\phi_3}{2\Delta n}, \qquad \begin{matrix} \phi_0 = \phi_2, & \phi_{-1} = \phi_3, & \phi_0' = -\phi_2', \\ \dots & \dots & \dots \end{matrix} \tag{3.12}$$

Based on this set of equations, the LHS of equation 3.11 and equation 3.12 forms a set of discretised tridiagonal equations. The coefficients of these equations can be represented by the following tridiagonal matrices:

$$\begin{pmatrix} 3 & 0 & & & & & \\ 1 & 3 & 1 & & & & \\ & 1 & 3 & 1 & & & \\ & & \cdots & \cdots & \cdots & & \\ & & & 1 & 3 & 1 & \\ & & & & 1 & 4 & 1 \\ & & & & & 4 & 2 \end{pmatrix}, \qquad \begin{pmatrix} 3 & 2 & & & & & \\ 1 & 3 & 1 & & & & \\ & 1 & 3 & 1 & & & \\ & & \cdots & \cdots & \cdots & & \\ & & & 1 & 3 & 1 & \\ & & & & 1 & 4 & 1 \\ & & & & & 4 & 2 \end{pmatrix}. \tag{3.13}$$

For the second derivative, the pressure and velocity components at j = 1 yield:

$$\Rightarrow a\phi_1'' + 2\phi_2'' = b\frac{2\phi_2 - 2\phi_1}{\Delta n^2} + c\frac{2\phi_3 - 2\phi_1}{4\Delta n^2}, \qquad \begin{matrix} \phi_0 = \phi_2, & \phi_{-1} = \phi_3, & \phi_0' = -\phi_2', \\ \ldots. & \ldots. & \ldots. \end{matrix} \tag{3.14}$$

$$\Rightarrow a\phi_1'' + 0\phi_2'' = b\frac{-2\phi_1}{\Delta n^2} + c\frac{-2\phi_1}{4\Delta n^2}, \qquad \begin{matrix} \phi_0 = \phi_2, & \phi_{-1} = \phi_3, & \phi_0' = -\phi_2', \\ \ldots. & \ldots. & \ldots. \end{matrix} \tag{3.15}$$

The accompanying tri-diagonal matrices for equation (3.14) & equation (3.15) can be written as:

$$\begin{pmatrix} 5.5 & 0 & & & & & \\ 1 & 5.5 & 1 & & & & \\ & 1 & 5.5 & 1 & & & \\ & & \cdots & \cdots & \cdots & & \\ & & & 1 & 5.5 & 1 & \\ & & & & 1 & 10 & 1 \\ & & & & & 11 & 1 \end{pmatrix}, \qquad \begin{pmatrix} 5.5 & 2 & & & & & \\ 1 & 5.5 & 1 & & & & \\ & 1 & 5.5 & 1 & & & \\ & & \cdots & \cdots & \cdots & & \\ & & & 1 & 5.5 & 1 & \\ & & & & 1 & 10 & 1 \\ & & & & & 11 & 1 \end{pmatrix}. \tag{3.16}$$

3.4 GRID MAPPING

For the *3D* configuration the computational grid has a constant distribution in the *x,y,z* directions. In the case of the axisymmetric and *2D* planar configurations the grid is stretched in the r or y direction while remaining constant in the x direction. This grid mapping technique was developed by Luo and Sandham [1997].

For the axisymmetric configuration, a *sinh* function is used to achieve a higher grid density in the region around the jet centreline. The mapping function is defined as:

$$r(\eta, r_0, b_r) = r_0 \left\{ 1 + \frac{sinh\left[b_r(\eta - B) \right]}{sinh(b_r B)} \right\}, \tag{3.17}$$

For equation (3.17) the variable B can be defined as:

$$B = \frac{1}{2b_r} ln \frac{1 + \left(e^{b_r} - 1\right)\left(\frac{r_0}{L_r}\right)}{1 + \left(e^{-b_r} - 1\right)\left(\frac{r_0}{L_r}\right)}. \tag{3.18}$$

In equation 3.17, η is the mapped coordinate location. The stretching factor of the grid is defined by b_r. Thus, the metrics given in equation (3.19) and equation (3.20) can be determined.

$$h' = \frac{\partial r}{\partial \eta} = r_0 b_r \frac{cosh\left[b_r (\eta - B) \right]}{sinh\left(b_r B \right)}, \tag{3.19}$$

$$h'' = \frac{\partial^2 r}{\partial \eta^2} = r_0 b_r^2 \frac{sinh\left[b_r (\eta - B) \right]}{sinh\left(b_r B \right)}. \tag{3.20}$$

The planar configuration uses a slightly modified version of the grid mapping scheme used in the axisymmetric case. Here y_0 is taken as the jet centreline. The mapping function is given as:

$$y(\eta, y_0, b_y) = y_0 \left\{ 0.5Ly \frac{sinh\left(b_y \eta \right)}{sinh\left(b_y \right)} \right\}. \tag{3.21}$$

In equation 3.21, η is the mapped coordinate and b_y is the stretching parameter in the y direction, defined by:

$$h' = \frac{\partial y}{\partial \eta} = 0.5Lyb_y \frac{cosh(b_y\eta)}{sinh(b_y)}, \qquad (3.22)$$

$$h'' = \frac{\partial^2 y}{\partial \eta^2} = 0.5Lyb_y^2 \frac{sinh(b_y\eta)}{sinh(b_y)}. \qquad (3.2$$

3.5 BOUNDARY CONDITIONS

For the axisymmetric case, the computational domain is formed by a *2D* rectangular box, one side of which is the jet centreline. The extent of the computational domain used is $L_x = 100$ and $L_r = 40$ for all cases. Non-reflecting characteristic boundary conditions (NRCBC) based on the Navier-Stokes characteristic boundary condition formulation are applied at the side boundary in the radial direction and the streamwise directions [Jiang, 2006]. Symmetry conditions are applied along the jet centreline, which forms the central axis of the cylindrical axisymmetric domain. The Navier-Stokes characteristic boundary condition (NSCBC) developed by Poinsot & Lele [1992] has been utilised to model the oscillating inflow boundary condition at the jet orifice [Jiang, 2004]. The details of the NSCBC condition are given in Chapter 3.6.

The five boundary conditions for the axisymmetric case are defined as follows:

1. The symmetric boundary at the jet centreline $r = 0$;
2. The far side non-reflecting boundary in the radial direction $r = Lr$;
3. An inflow boundary at the domain inlet $x = 0, \ r \leq 1$;
4. Non-slip boundary adjacent to the domain inlet $x = 0, r > 1$;
5. A non-reflecting boundary downstream of the computational domain $x = Lx$.

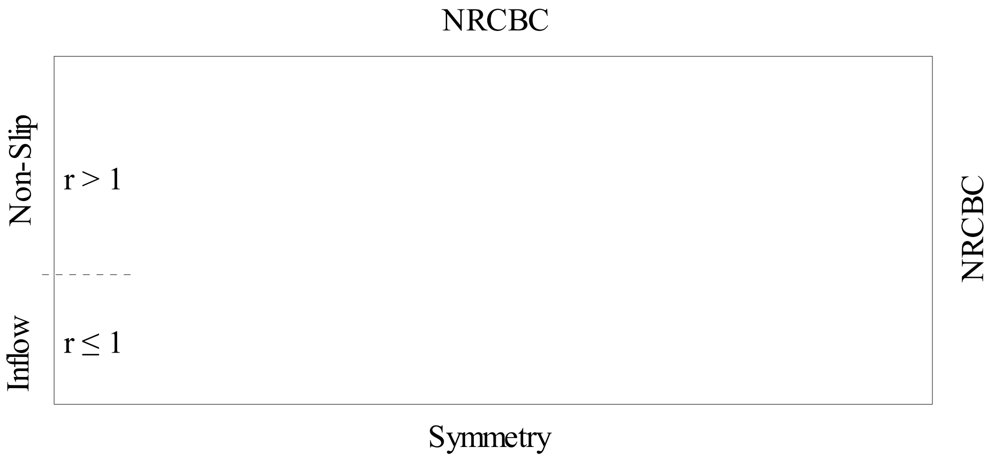

Fig. 3.1 Schematic of the physical problem of an axisymmetric synthetic jet

For the planar case, the computational domain is also formed by a two-dimensional rectangular box representing a cross-section of the physical problem. The extent of the computational domain used is $L_x = 100$ and $L_y = 80$. There are five boundaries for the computational domain. Non-reflecting boundary conditions are applied at all boundaries with the exception of the jet inflow and wall. A NSCBC has been utilised to specify both the boundary layer type velocity inlet profile and the sinusoidally oscillating inflow boundary condition at the jet orifice.

The five boundary conditions for the planar case are defined as follows:

1. The non-reflecting boundary / Inflow in the direction $y = -Ly/2$;
2. The far side non-reflecting boundary in the direction $y = Ly/2$;
3. An inflow boundary at the domain inlet $x = 0,\ -0.5 \le y \le 0.5$;
4. A non-slip boundary adjacent to the domain inlet $x = 0,\ 0.5 > y\ \&\ y < -0.5$;
5. A non-reflecting boundary downstream of the computational domain $x = Lx$.

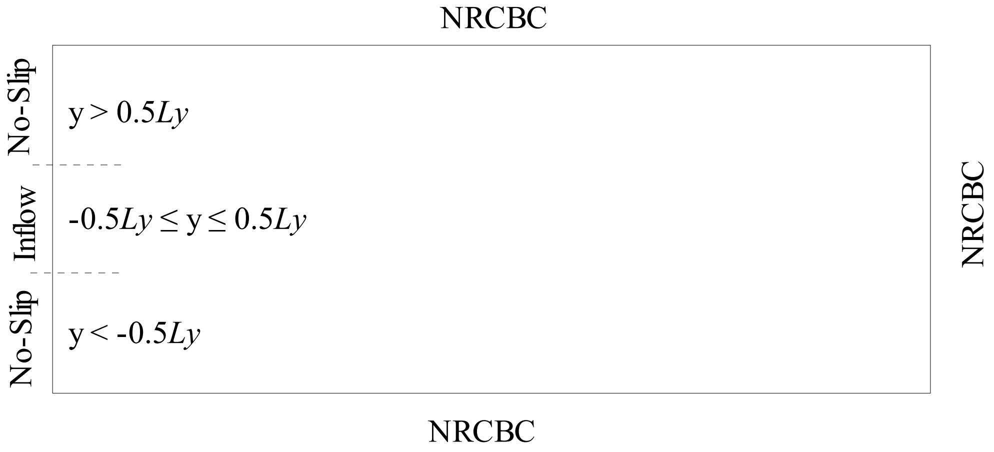

Fig. 3.2 Schematic of the physical problem of a planar synthetic jet

There are seven boundaries for the computational domain of the three-dimensional test case. The domain is rectangular in shape with a circular jet orifice located at $x = 0$, $y,z \le 1$. The extents of the coordinate domain, non-dimensionalised by the orifice diameter are: $y = 12$, $z = 12$, $x = 30$. The actuator orifice is located flush with the y z

coordinate plane. The time-dependent velocity profile of the pulsating jet at the inlet is specified based on the mean velocity and an additional sinusoidal pulsating component which is described in Chapter 3.6.

The seven boundary conditions for the 3*D* case are defined as follows:

1. The non-reflecting boundary in the direction $y = -Ly/2$;
2. The far side non-reflecting boundary in the direction $y = Ly/2$;
3. An inflow boundary at the domain inlet $x = 0, \; -0.5 \leq y \leq 0.5, -0.5 \leq z \leq 0.5$;
4. A non-slip boundary at the domain inlet $x = 0, 0.5 < y \;\; \& \, y < -0.5, z = 0$;
5. A non-slip boundary downstream of the computational domain $x = Lx$.
6. The non-reflecting boundary in the direction $z = -Lz/2$;
7. The non-reflecting boundary in the direction $z = Lz/2$.

3.6 THE NAVIER STOKES CHARACTERISTIC BOUNDARY CONDITIONS

The Navier-Stokes characteristic boundary condition (NSCBC) as formulated by Poinsot and Lele [1992] has been utilised for the specification of the inflow boundary conditions for all cases. The NSCBC avoids unstable numerical calculations and associated wave reflections from the computational boundaries by solving the Navier-Stokes equations with the correct number of boundary conditions [Jiang, 2000]. For the NSCBC, the Local

One-Dimensional Inviscid (LODI) relations developed by Lele [1992] have been used to provide compatible relations between the physical boundary conditions and the amplitudes of characteristic waves crossing the boundary [Jiang, 2006]. For a synthetic jet, the amplitudes of the characteristic waves at the inflow boundary are estimated by the LODI relations. At the boundary located at $x_1 = L$, the waves entering and leaving the domain in the *x* direction are shown in figure 4.2. The one-Dimensional inviscid LODI relations represented in figure 4.2 are expanded into a multidimensional viscous form for use simulating the synthetic jet flow field.

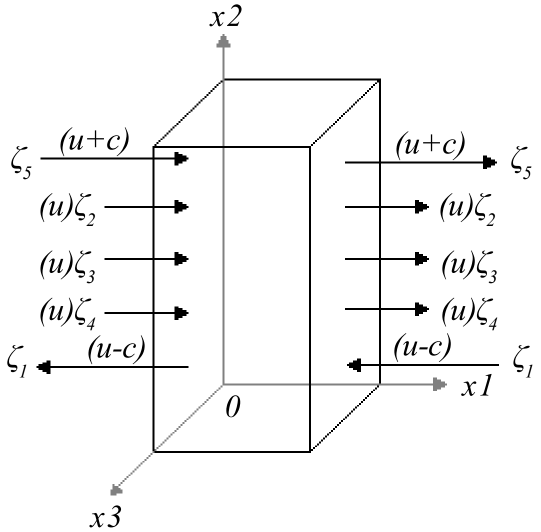

Fig. 3.3 Waves entering and leaving the computational domain

The wave amplitudes can be specified as:

- $\zeta_1 = (u - c)\left(\frac{\partial p}{\partial x} = \rho c \frac{\partial u}{\partial x}\right),$ (3.24)
- $\zeta_2 = u\left(\frac{\partial p}{\partial x} = c^2 \frac{\partial \rho}{\partial x}\right),$ (3.25)
- $\zeta_3 = u\frac{\partial v}{\partial x},$ (3.26)
- $\zeta_4 = u\frac{\partial w}{\partial x},$ (3.27)
- $\zeta_5 = (u + c)\left(\frac{\partial p}{\partial x} = \rho c \frac{\partial u}{\partial x}\right),$ (3.28)

The LODI primitive variables, can be written as:

- Density: $\frac{\partial \rho}{\partial t} + \frac{1}{c^2}\left[-\zeta_2 + \frac{1}{2}(\zeta_5 + \zeta_1)\right] = 0$ (3.29)
- Pressure: $\frac{\partial \rho}{\partial t} + \frac{1}{2}(\zeta_5 + \zeta_1) = 0$ (3.30)
- Velocity: $\frac{\partial u}{\partial t} + \frac{1}{2\rho c}(\zeta_5 - \zeta_1) = 0$ (3.31)
- Subsonic Flow: $\zeta_5 = \zeta_1 = 2\rho c\frac{\partial u}{\partial t}$ (3.32)

3.6.1 INLET VELOCITY PROFILES

At the domain inlet (jet nozzle exit), the streamwise mean velocity has been specified as a hyperbolic tangent profile given by:

$$\bar{w} = \left\{1 - \tanh\left(\left(\frac{r_0}{4} \times \frac{1}{\delta}\right) \times \left(\frac{r}{r_0} \times \frac{1}{r + \Delta}\right) \times \left(\frac{x_1 - x_x}{x_1}\right)\right)\right\} \tag{3.33}$$

where:

$$r = \sqrt{(y - 0.5L_y)^2 + (z - 0.5L_z)^2} \tag{3.34}$$

In equation 3.34, r is the radial variable originating from the centre of the inlet domain ($0 \leq y \leq Ly,\ 0 \leq z \leq Lz$), and Δ is set to be equal to $\Delta = 1 \times e^{-9}$. The coefficients used in the above equation describing the velocity profile define the jet initial momentum thickness. The cross-streamwise mean velocity components at the domain inlet $x = 0$ are given by $\bar{u} = 0$ and $\bar{v} = 0$. The periodic pulsating streamwise velocity profile at the inlet is specified as:

$$W_x = \left[\cos(2\pi f_0 t)\right] \tag{3.35}$$

For the 2*D* planar case with a cross-streamwise velocity profile has been applied at the -*Ly*/2 boundary, which is specified as follows:

$$bv = \left\{ \tanh\left(\left(\frac{\Delta}{4} \times \frac{1}{bl} \right) \times \left(\frac{x_x}{\Delta} - \frac{\Delta}{x_x + \Delta} \right) \right) \times v \right\} \tag{3.36}$$

In equation 3.36, *x* is the location in the jet streamwise direction and *v* is the cross-streamwise velocity. The imposed thickness of the velocity profile is defined as *bl*, which in the cases analysed was specified so the entire vortex train of the synthetic jet was within the *bv* velocity profile.

For the 3*D* synthetic jet case, a sinusoidal disturbance is added to the oscillating inlet velocity profile. The purpose of this disturbance was to break the 3*D* symmetry of the jet associated with an undisturbed hyperbolic top-hat velocity profile. The inlet velocity profile has been perturbed by two small helical disturbances [Danaila & Boersma, 2000], [Uchiyama, 2004]. The velocity components of these perturbations at the nozzle exit $x = 0$ are shown in equations 3.37 , 3.38 and 3.39.

$$u = \overline{U} + A\sin\left(m\varphi - 2\pi f_0 t \right), \tag{3.37}$$

$$v = \overline{V} + A\sin\left(m\varphi - 2\pi f_0 t \right), \tag{3.38}$$

$$w = \overline{W} + A\sin\left(m\varphi - 2\pi f_0 t \right), \tag{3.39}$$

In this case A represents the amplitude of the disturbance, which was defined as 1% of the peak value of the mean streamwise velocity $\overline{U}$. Two helical modes of m = 1 and m = -1 were superimposed on the temporal disturbance, where φ is the azimuthal angle [Jiang & Luo, 2000]. The non-dimensional frequency of the unsteady excitation is defined as f_0.

In the simulations performed, the flow field is initialised using a velocity field that varies linearly between its value at the domain inlet and that at the wall boundary [Jiang, 2006]. The initial conditions utilised did not affect the results of the developed synthetic jet flow field. At the jet centreline, the singularity associated with the symmetry boundary at $r = 0$ can be overcome through the use of l'Hôspital's rule with the term u_r/r.

3.7 SUMMARY

In this chapter the high-order finite difference schemes for the time advancement and spatial discretisation that are used to simulate the synthetic jets are described. The governing equations for both the axisymmetric and three-dimensional analysis are outlined and their method of implementation in the code is shown. This section also includes a description of the boundary conditions for both the axisymmetric, planar and 3*d* cases, highlighting the differences between the three schemes.

CHAPTER 4

CODE VALIDATION

4.1 INTRODUCTION

In order to ensure that the DNS code used was accurately predicting the flow field, a comparative study was made between the synthetic jet code and previously validated work on synthetic jet actuators. This comparative study was based on work compiled during the 2004 NASA Synthetic jet validation workshop held by the NASA Langley Research Centre [Rumsey, 2007]. The work presented for this workshop was found to be the most complete and relevant study of modelling *2D* synthetic jet actuators using CFD and comparing these results directly with experimental data. The first of the cases presented in the validation work presented by Rumsey was the modelling of a synthetic jet issuing into quiescent air. Comparisons were carried out with both the Particle Image Velocimetry (PIV) experimental data presented by Rumsey and also a set of CFD results of the same test case. By completing this comparison study with previously validated data, a level of confidence in the solution data produced by the synthetic jet code can be assumed. Therefore further modifications to the input parameters of the jet code; or indeed the modification of the jet code to solve a jet flow in a fully three-dimensional fluidic domain can be determined to produce accurate results.

A comparative study was made for the time averaged and phase averaged velocity profiles of a synthetic jet run for two complete actuator cycles (i.e. two 360° phases (ϕ)). The 2nd order CFD results presented by Rupesh *et al.* [Rupesh *et al.,* 2004] were also compared with the present DNS results in order to increase the confidence level in the latter.

The numerical methods used by Rupesh *et al.* involved the unsteady incompressible Navier Stokes equations. The solutions were integrated forward in time utilising the fractional step method. A 2nd order Adams-Bashforth scheme was employed for the convective terms while the diffusion terms were discretised using an implicit Crank-Nicolson scheme [Rupesh *et al.,* 2004].

The planar code was run up to a point where two full phases had been completed using a time-step value shown in Table 4.1. The average jet velocity provided by Laser Doppler Velocimetry (LDV) work was taken as *Uj* = 10.5 m/s, the actuation frequency was ω = 2794 rad/s, and the orifice diameter was d = 1.27mm [Rupesh *et al.,* 2004]. The input parameters for the cases considered are displayed in Table 4.1.

#	***Re***	**2*D*/3*D***	**Exterior Domain Size**	**Grid Size**	**Time Steps / cycle (N)**	$\Delta t = \frac{2\pi}{\omega N}$
Rupesh	750	2*D*	30d x 30d	220 x 132	$1.4 \times e^{4}$	$1.16 \times e^{-3}$
DNS	750	2*D*	30d x 30d	301 x 10000	$4.895 \times e^{10}$	$1.28 \times e^{-10}$

Table.4.1 Input parameters for the validation case

The phase averaged *U*-velocity was calculated at a point $x = 0.07874d$. At this point the same methodology as used by Rupesh *et. al* was used to align the DNS results with the PIV results presented by Rupesh *et. al.* The procedure of calculating the 'phase set angle' used for the alignment of the data is outlined in Fig 4.1. The phase set angle was calculated by this method for both the DNS and PIV results. The DNS results were then shifted by the offset between the two 'phase set angles'. In all cases the non dimensionalised jet velocity of the DNS case was dimensioned in terms of the orifice diameter '*d*' and time '*t*'.

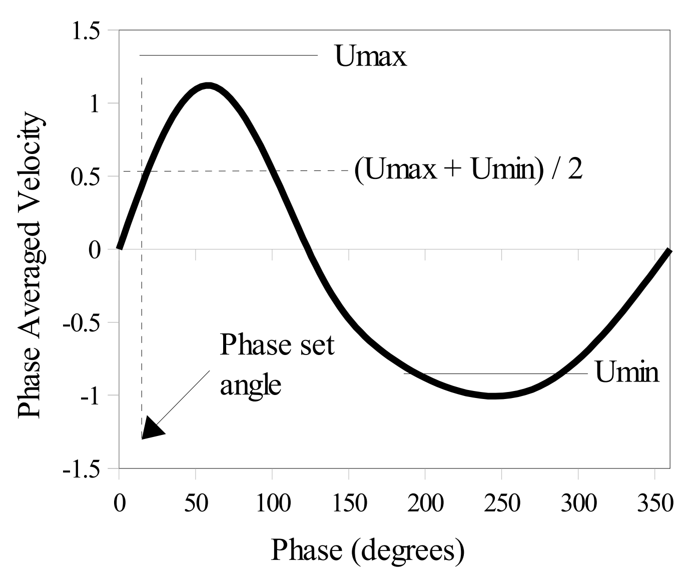

Fig 4.1 Procedure for calculating the phase offset angle

4.2 RESULTS

Figure 4.2 shows the plot of phase averaged *U*-velocity vs. phase angle ϕ after the phase alignment has been carried out. In this case the DNS results are presented alongside both the CFD results calculated by Rupesh *et. al* and the PIV experimental results. Rupesh *et.*

al noted a 'reasonable' agreement between their CFD results and the PIV data. In this case it can be noted that the present DNS code results are more consistent with the PIV data than Rupesh's CFD results, the DNS results yielding a cumulative deviation from the PIV data of 37.89% less than the results calculated by Rupesh *et. al.*

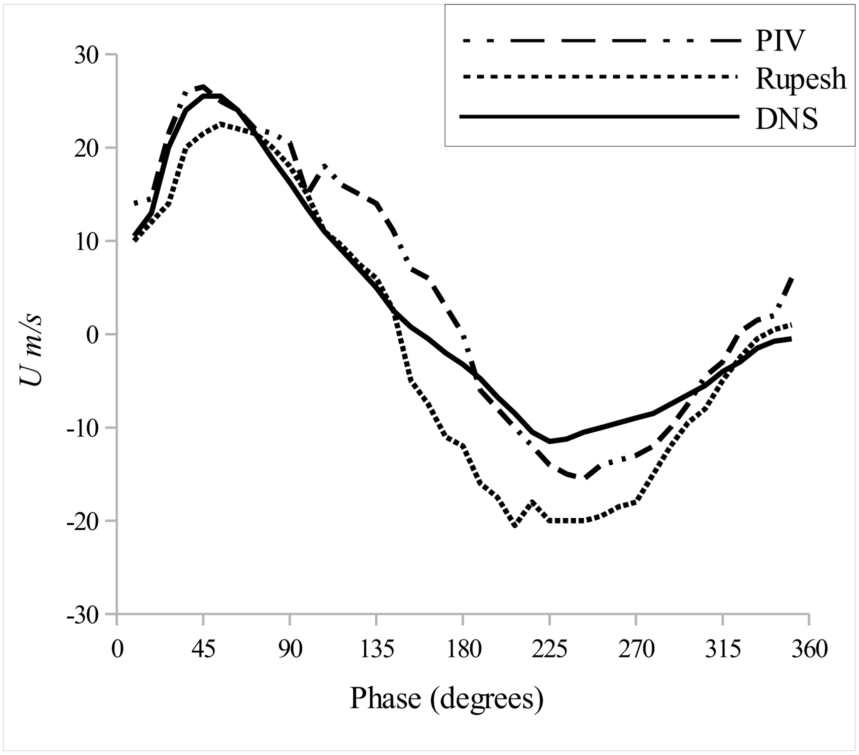

Fig 4.2 Phase averaged *U* vs. phase angle after phase alignment.

Figure 4.3 shows the cross-streamwise (*V*) velocity profiles for the DNS, PIV and Rupesh's CFD case, time averaged over the complete two actuator cycles. It can be seen that all cases presented in figure 4.3 follow a similar profile of a lateral movement away from the orifice in the region -4 < y/d < 4. The profile of this *V* velocity is in agreement with the expected velocity profile of a passing vortex structure, with the peak of this *V* velocity component predicted in the region y/d = ±1.

Figure 4.4 shows the time-averaged streamwise jet velocity for all three cases. Again, in this case the DNS results were found to be in closer agreement with the experimental PIV results than the CFD results calculated by Rupesh. In both cases the CFD and DNS results predict a stronger recirculation in the region adjacent to the actuator orifice than the PIV results. This can be indicated by the larger negative streamwise velocity component shown by the results calculated by Rupesh & DNS results in the region -1 < y/d < 1. The DNS results can be seen to be in closer agreement with the PIV results in predicting the maximum time-averaged centreline velocity of the synthetic jet.

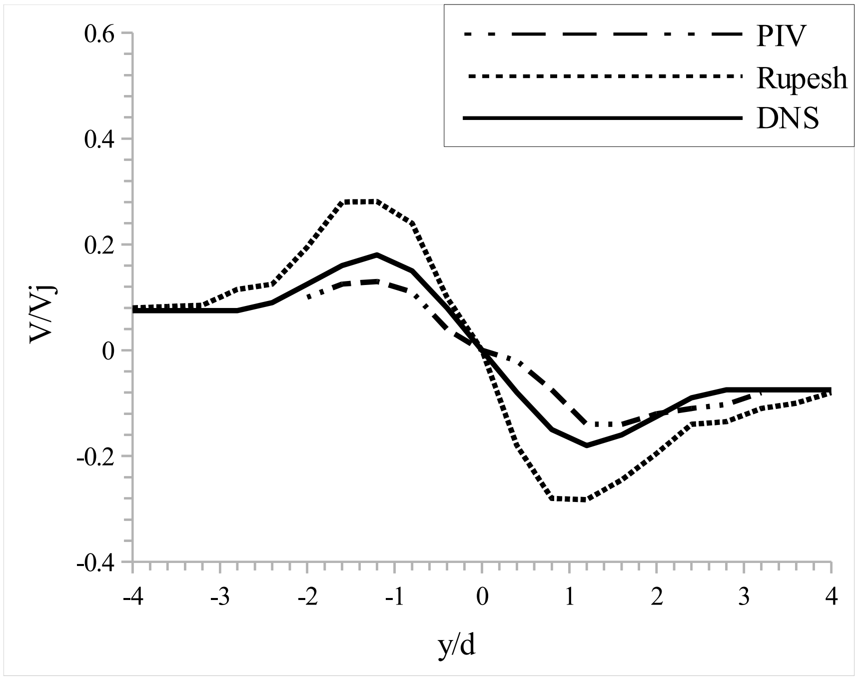

Fig 4.3 Time averaged V velocity along the x = 0.7874 line.

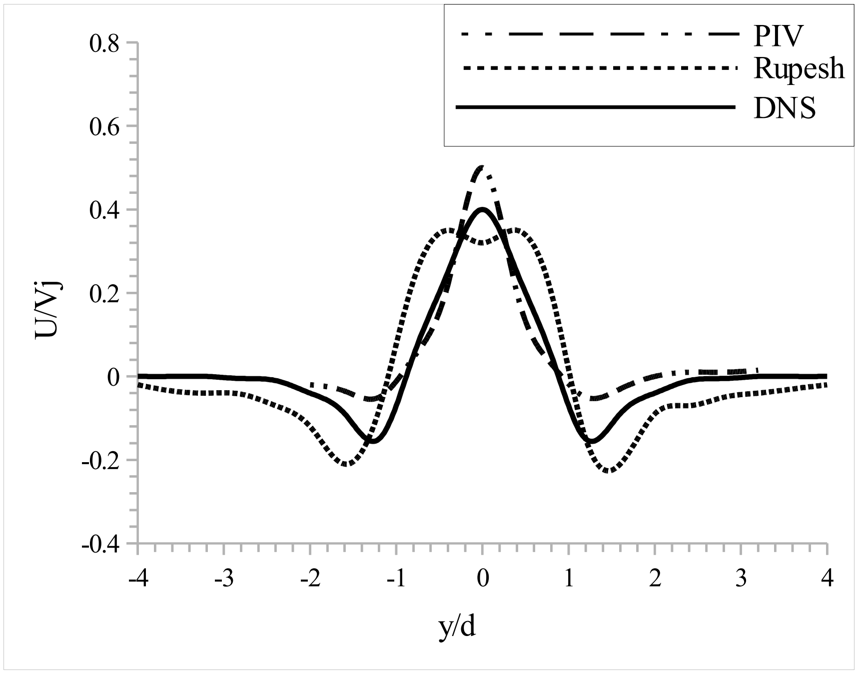

Fig 4.4 Time averaged U velocity along the x = 0.7874 line.

Figure 4.5 to Fig. 4.8 show the phase averaged *U* & *V* velocity profiles at phase angles of ϕ=90° and ϕ=270°, i.e. at the full expulsion and suction phases of the actuator cycle. It should be noted that the results presented by Rupesh *et. al* actually correspond to phase angles of ϕ=91° and ϕ=271°. As can be seen in figure 4.5, the DNS code and Rupesh's CFD code again predict a stronger recirculation region in the region close to the jet orifice during the expulsion phase of the actuation cycle. Figure 4.6 shows the jet centreline streamwise velocity; in this case the DNS and PIV results can be noted to be in close agreement in the region -1 < y/d < 1.

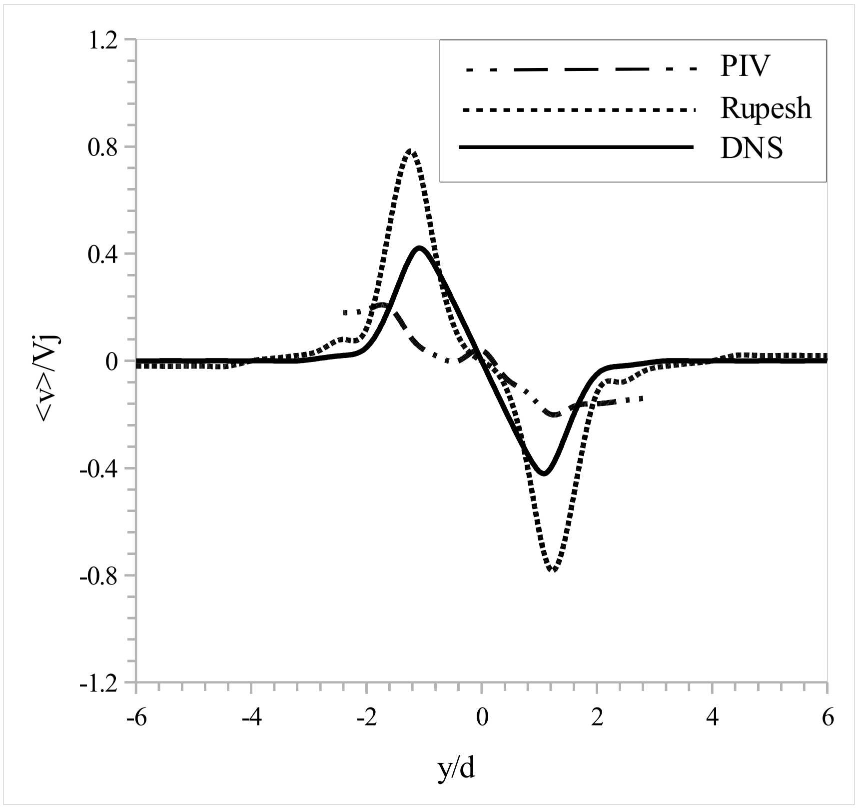

Fig 4.5 Phase averaged *V* velocity along the *x* = 0.7874 line at $\phi = 90°$

In figure 4.7 & figure 4.8 the phase averaged results for all three cases at a phase angle of $\phi = 270°$ are presented. In figure 4.7 the DNS, PIV and the results presented by Rupesh *et. al* can be seen to agree well in the region -1 < y/d < 1. There were no PIV results available for the region y/d < -2.5 & y/d > 2.5. However the DNS results can be seen to be following a similar trend to the PIV results and are in close agreement with them in the region 0.5 < y/d < 2.5. The CFD results presented by Rupesh seem to over predict the magnitude of the *V* velocity in the regions further away from the orifice compared to both the PIV and DNS results. Causes of possible errors such as this are discussed later in this chapter.

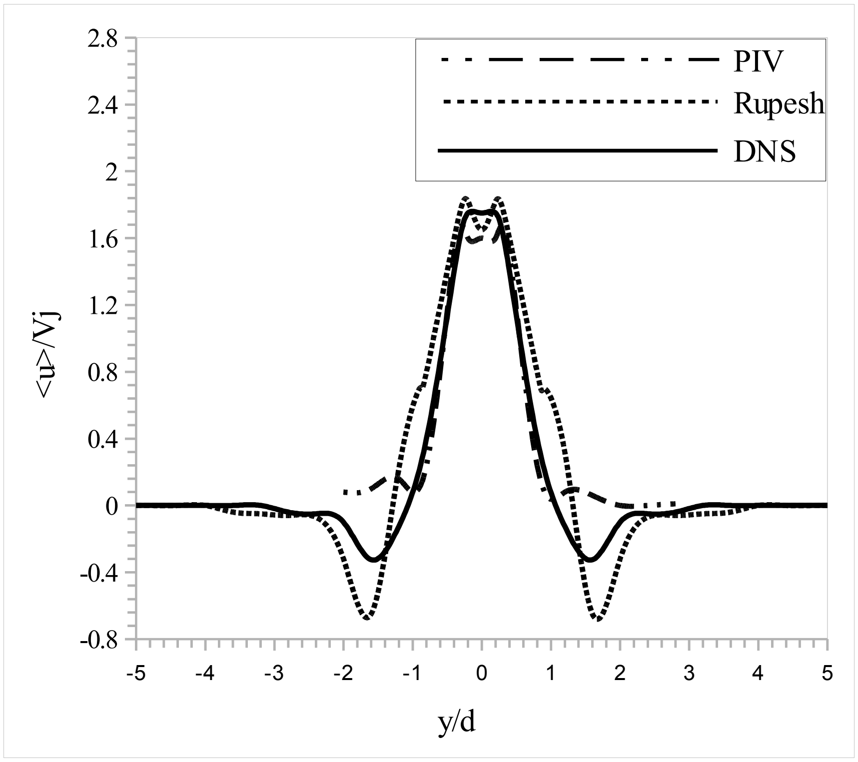

Fig 4.6 Phase averaged *U* velocity along the *x* = 0.7874 line at ϕ = 90°

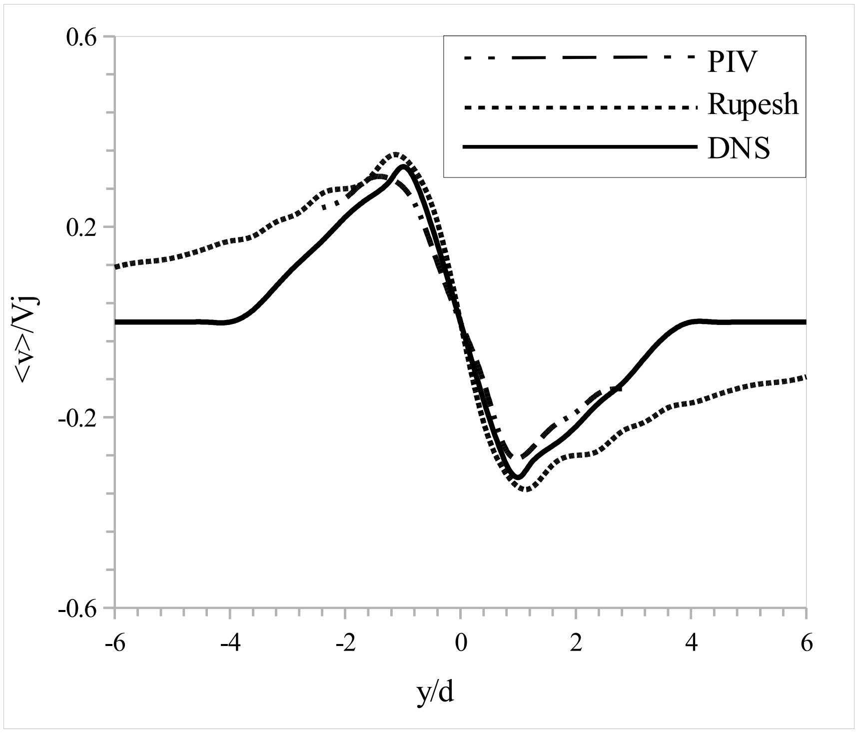

Fig 4.7 Phase averaged *V* velocity along the *x* = 0.7874 line at ϕ = 270°

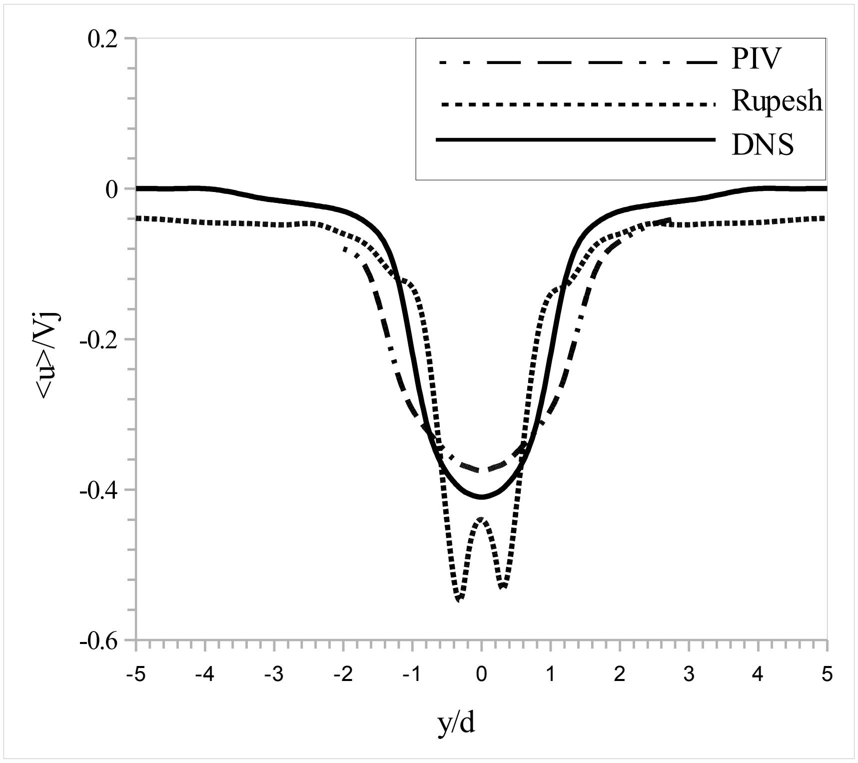

Fig 4.8 Phase averaged *U* velocity along the *x* = 0.7874 line at ϕ = 270°

4.3 CONCLUSION

This comparison of the DNS results with the previously validated CFD model presented by Rupesh *et. al* and with the PIV results, allows a confidence level in the accuracy of the DNS case to be assumed. Similar velocity profile trends and flow features were identified in all three cases analysed in this comparative exercise. In all cases the DNS results could be seen to be closer to the experimental PIV results than the results calculated by Rupesh *et. al*. This would be expected as the CFD code used by Rupesh *et. al* was of 2nd order accuracy. It is also worth noting that the DNS and Rupesh's CFD results are 2*D* solutions, whereas the PIV results present a 2*D* visualisation of a 3*D* flow field. Therefore some deviation in the results is to be expected. However as shown in this validation exercise, this was negligible in the region near the orifice where the results were calculated, possibly due to the 2*D* nature of the jet flow in the near-wall region [Tang & Zhong, 2005].

There are a number of possible sources of error in PIV experimental results that are worth noting when making a direct comparison for validation purposes. The velocity vectors calculated by PIV are based on a cross-correlation of the intensity distributions in finite regions of the flow field. The velocity field produced by PIV is a spatial average of the actual velocity field, thus effecting the accuracy of the spatial derivatives of the velocity field. Romano [2003] also noted a source of possible errors in near wall regions, where high noise levels are present due to the scattering of the light on the wall. He also noted possible errors in flows with high vorticity regions such as the jet flow field of a synthetic jet actuator.

The level of symmetry about the jet centreline axis of the velocity profiles presented by Rupesh *et. al* is also worth noting. In their CFD case the entire 2*D* jet cavity and orifice was modelled. The results presented by Rupesh *et. al* for the velocity profiles in the region close to the wall show a comparable level of flow symmetry with the DNS case, thus suggesting that the sinusoidal velocity profile applied in the DNS case, is an accurate approximation of a fully modelled CFD synthetic jet orifice flow.

CHAPTER 5

AXISYMMETRIC SYNTHETIC JET SIMULATIONS

5.1 INTRODUCTION

In this chapter a DNS analysis is carried out on an axisymmetric synthetic jet actuator. Several computational cases have been examined; both to determine the simulation parameters required to achieve accurate flow field results, and to optimise the jet formation parameters. The formation of a true jet flow, characterised by the formation of a vortex train, may be influenced by $3D$ effects. Therefore it is beneficial to complete an axisymmetric analysis of the jet flow field as the first step of a comparative study analysing the influence of this three-dimensionality on the jet evolution.

The input parameters determined during the optimisation of the jet actuator for the axisymmetric case will then be used as the corresponding inputs for the $3D$ case. It was essential to optimise the jet formation criterion in the axisymmetric case due to the large computational burden of the fully $3D$ case. These simulations also provide a valuable insight into the vortex dynamics of the flow over a large range of parameters. The effect of varying each of the parameters can also be viewed independently; a benefit of using numerical methods which is difficult to achieve in experimental testing. For example, Kotapati *et al.* [2007] noted the work of Smith & Gleezer [2005] in analysing the effect on a synthetic jet of altering the amplitude of a piezo-electric actuator diaphragm.

This, however, simultaneously increased both the jet Reynolds number and Strouhal number proportionately while at the same time keeping the Stokes number the same.

5.2 SIMULATION DETAILS

Several computational cases have been analysed in order to investigate the formation criterion and evolution of a synthetic jet flow field. A parametric study was performed to investigate the effects of varying the actuator frequency. Tests were also carried out to deduce the Reynolds number effects on the jet development. From this parametric study, an optimised set of input parameters to produce a jet flow field with a maximum mass flow, vortex intensity and longevity.

The maximum time-step is dependent on the CFL number, which also relates to the mesh density. Investigations into the effect of varying the CFL number resulted in a value of 10.0 being used. This CFL value gave results independent of time-step, while also not resulting in excessive simulation run times. Both instantaneous and time-averaged flow results were obtained and used to analyse both the flow structures present and the evolution of the flow field.

5.2.1 ACTUATION FREQUENCY

For different pulsating frequencies applied at the inflow, the axisymmetric jet displays significantly different vortex structures. As stated by Jiang *et al.* [2006], there is an optimum frequency at which an axisymmetric disturbance undergoes maximum amplifications in the jet flow. The optimum frequency is related to both the flow conditions and Strouhal number. The optimum Strouhal number is primarily in the range $St = 0.3 - 0.5$, with the most commonly value being $St = 0.3$. Table.4.1 gives an outline of all the actuation frequencies for the synthetic jets analysed in this study. The Reynolds number used in all cases was $Re = 300$.

Case	A	B	C	D	E
Strouhal number	0.02	0.04	0.08	0.16	0.32
Reynolds number	300	300	300	300	300
CFL number	10	10	10	10	10

Table 5.1. The computational cases of the axisymmetric simulations

Figure 5.1 and figure 5.2 show the effect of the actuator oscillation frequency on the instantaneous flow characteristics of the zero-net-mass-flux synthetic jets. figure 5.1 shows the instantaneous jet centreline velocities at $t = 80$ for the five cases listed in Table. 5.1. It can be noted that the centreline streamwise velocities of different cases behave very differently. There are large variations in the velocity profiles and these variations occur at different locations with different amplitudes. These velocity oscillations are associated with the formation and convection of large-scale vortex structures in the flow field. In Case E, with a Strouhal number of $St = 0.32$, no oscillation in the centreline velocity is present. This is due to re-ingestion of the expelled flow on the return stroke of the jet actuator, before it has travelled a sufficient distance downstream to remain unaffected. In this case the centreline velocity can be noted to drop quickly away from the orifice, with almost no trace of the previous velocity slug remaining.

Figure 5.3 shows the instantaneous vorticity contours at $t = 80$ of all five cases. Case A, and Case B operate at a low frequency oscillation of $St = 0.02$ and $St = 0.04$ respectively. These two cases do not exhibit true "jet like" characteristics as the oscillation frequency is below the level required to form a vortex train. In these cases only a single vortex pair visible in the flow field; the vortices produced by previous actuator oscillation have completely dissipated by the time the actuator completes the successive actuation cycle. It can be noted however that although only a single vortex is produced by the actuator when operating at these low frequencies, the vorticity magnitude and size of the vortex produced are considerably larger than those of the vortices produced at higher actuation frequencies.

Case C and Case D which operate at an actuator frequency of $St = 0.08$ & $St = 0.16$ respectively, are the only two cases in this study in which a true jet stream is created. It can also be noted that the velocity oscillations for the $St = 0.08$ case are lower in amplitude and decay more rapidly than the $St = 0.04$ case, as shown in figure 5.3. This is assumed to be due to partial re-ingestion of the velocity slug with the higher actuator frequency. At a location just beyond $x = 10$ the streamwise oscillation can be seen to be completely damped out.

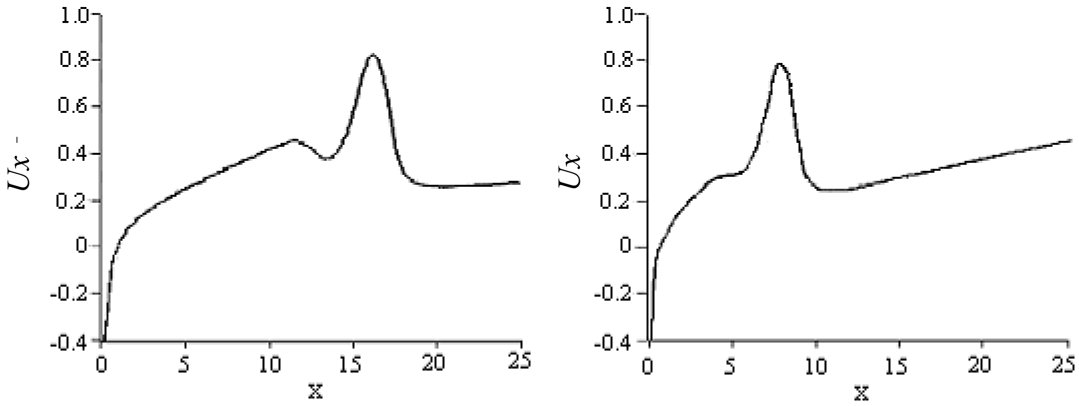

(a) Case A (b) Case B

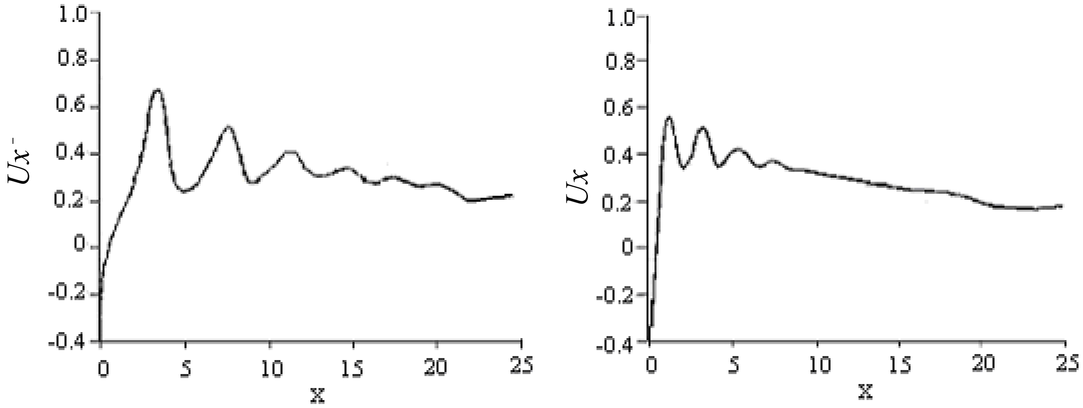

(c) Case C (d) Case D

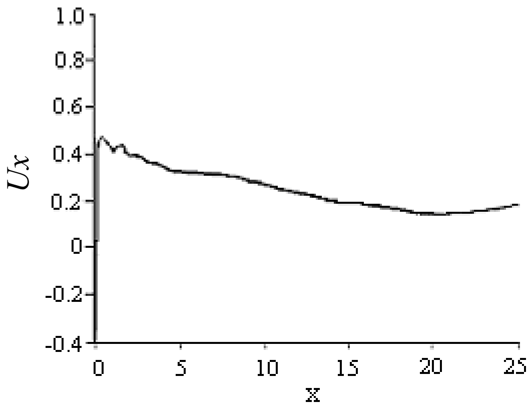

(e) Case E

Fig. 5.1. Streamwise centreline velocities at $t = 80$.

The lack of any large scale vortex structures can also clearly be noted for the *St* = 0.32 case. This was determined to be caused by the re-ingestion of the majority of the ejected fluid slug by the suction phase of the synthetic jet actuator. It can be noted that in figure 5.2 that the jet centreline streamwise velocity present is Case E reaches a peak value of *Uf* = 0.45. This maximum velocity peak can be seen to decrease as the actuation frequency increases. This decrease in maximum streamwise velocity can be related to the lack of a true vortex train at high actuation frequencies. In these cases the fluid slug ejected from the orifice on the expulsion phase of the actuation cycle does not have a sufficient downstream velocity to prevent being re-ingested into the actuator cavity on the suction stroke of the successive actuation. Both the reduction of the streamwise velocity of the fluid slug and the more rapid actuation frequency results in a fluid slug that moves more slowly downstream and has less time to reach a 'safe' distance from the orifice and therefore prevent re-ingestion. Therefore the ability to form a true vortex train decreases rapidly once the actuation frequency has been increased beyond its optimal value.

In figure 5.3, it was seen that larger pulsating frequency leads to smaller scale vortex structures and a corresponding reduction in the streamwise distance between the vortex scores. At higher pulsating frequencies a further reduction in the vortex size occurs, resulting in the rapid deterioration of the vortex structures as they move downstream.

In order to quantitatively analyse the effect of varying the actuation frequency and reinforce the selection of an optimum input parameter the jet momentum flux was deduced for each case. The method of calculating the momentum flux was specified by

Fugal, Smith & Spall [2005], who calculated the period averaged momentum flux per unit mass 'J' as:

$$J = \int_0^T \int_{-\infty}^{\infty} u^2 du dt \qquad (5.1)$$

where T is the actuation period and u is the mean streamwise velocity. For the case of a top-hat velocity profile and sinusoidal velocity flow equation 5.1 can be normalised by equation 5.2:

$$J_0 = u_{max}^2 \frac{r}{2} \qquad (5.2)$$

where u_{max} is the maximum mean streamwise velocity and r is the orifice radius.

Plotting the momentum flux as a function of streamwise distance from the orifice allows for a quantitative evaluation of the effect of varying the Strouhal number on the synthetic jet mass flow, as can be seen in figure 5.2.

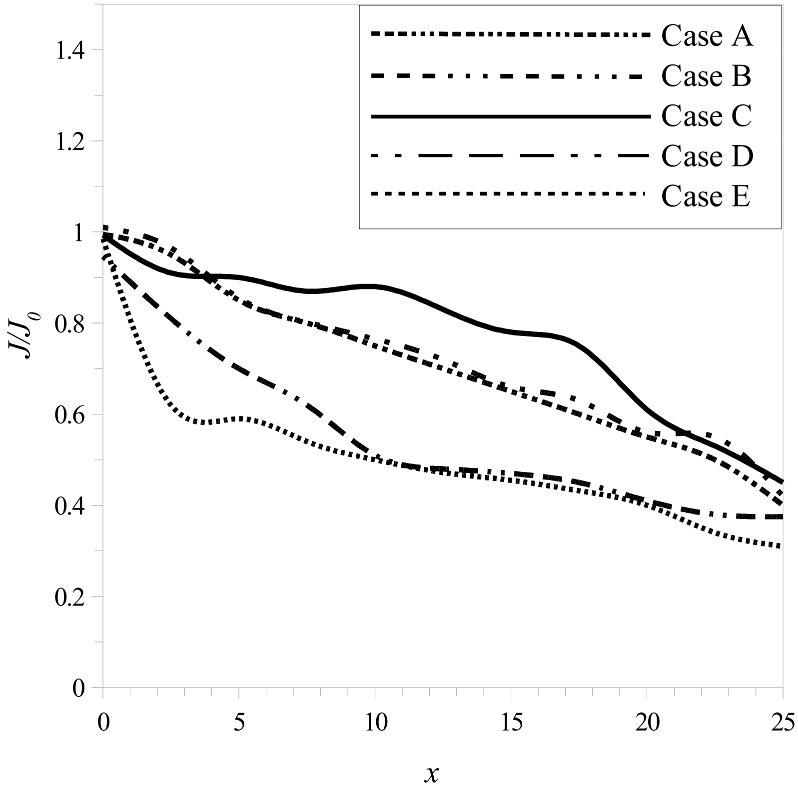

Fig. 5.2. Momentum flux as a function of the streamwise position for Case A-E.

From figure 5.2 it can be noted that Case C provides the largest magnitude momentum flux to the background fluid, when compared to the other four test cases. The two cases with the highest Strouhal number (Case D & Case E) display a rapid decrease in momentum flux as the streamwise distance from the orifice increases. Case C has been noted from figure 5.1 to display the characteristics of a true synthetic jet flow field. A clearly identifiable streamwise velocity oscillation can be noted extending from the actuator orifice, which can be associated with the formation of a vortex train. Case A & Case B display an almost linear decrease in momentum flux when the single vortex structure present gradually dissipates as it moves away from the orifice. Although the individual vortex structure present in Case A & Case B have been noted to be of a larger size than the cases with a higher Strouhal number; the lack of formation of a true vortex train results in a lower overall momentum flux than Case C.

An important observation as can be noted from figure 5.3 is that a synthetic jet does not display strong vortex structures for the frequency range at which the Strouhal number is greater than St = 0.16. A Strouhal number above St = 0.16 leads to jet preferred mode of instability for pulsating jets with non-zero mean velocity at the domain inlet [Jiang *et al*., 2006]. For a synthetic jet with zero mean velocity at the inlet, the jet developed discernible vortex structures at significantly lower actuation frequencies than those displayed by the non-zero mean velocity pulsating jets.

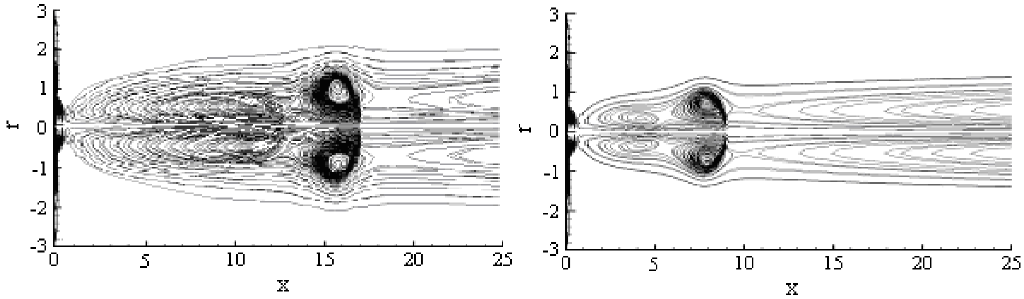

(a) Case A (b) Case B

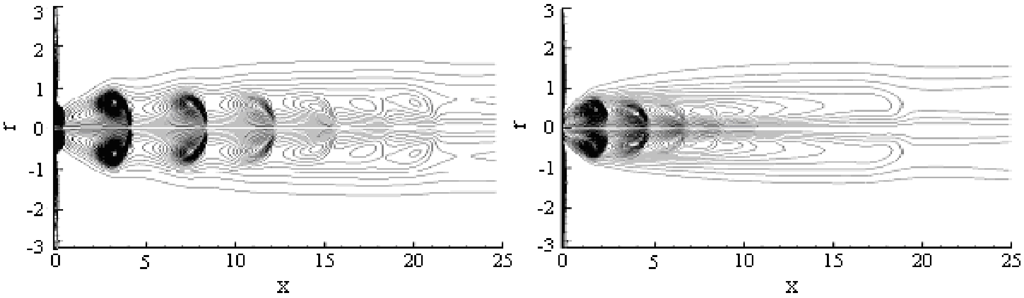

(c) Case C (d) Case D

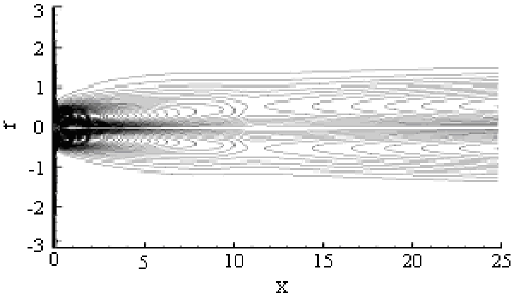

(e) Case E

Fig. 5.3. Instantaneous vorticity contours at $t = 80$.

5.2.2 REYNOLDS NUMBER EFFECTS

As the Reynolds number increases, smaller scales of the flow are visible. In the larger Reynolds number cases there is not as much viscosity present in the flow to dissipate the motions of the small scale eddies. Reynolds number is defined as the point at which the kinetic energy cascade from large scale eddies to progressively smaller eddies reaches a point for which the scale is small enough for viscous forces dissipate the kinetic energy in the flow. It is at these small scales where the dissipation of energy by viscous action finally takes place.

Experimentation with varying Reynolds number has a number of implications for determining both the Reynolds number range in which the simulation is valid and the optimum value with respect to maximising vorticity flux. As the Reynolds number decreases the number of grid points required to achieve converged results decreases. Figure 5.4 shows the instantaneous vorticity contours at *t* = 80 at two different Reynolds numbers. It can be seen that an increase in the Reynolds number leads to increased intensity and longevity of the vortex structures due to the smaller length scales present in the flow field.

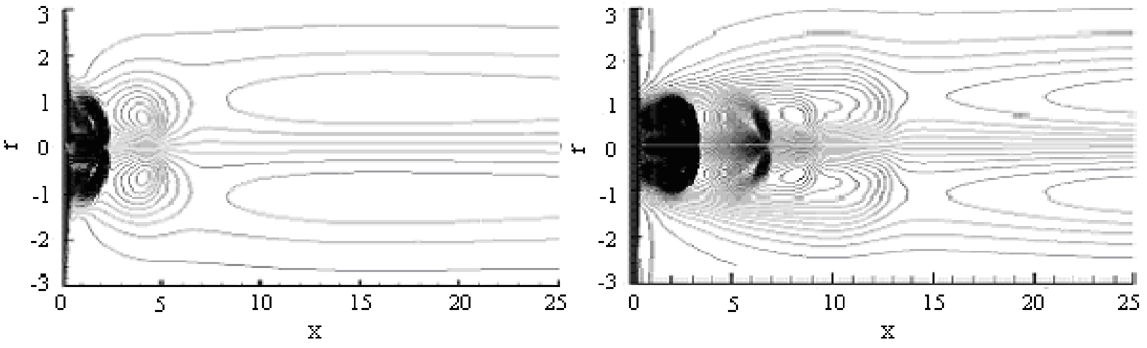

(a) ***Re*** **= 85** **(b)** ***Re*** **= 165**

Fig.5.4. Effect of Reynolds number: instantaneous vorticity contours at *t* = 80.

5.2.3 OPTIMAL JET ACTUATION CASE

The insights into the effects of the input parameters on the production of a true jet flow and maximised mass flow were used to create an optimal case in terms of maximum longevity and vortex strength. The input parameters used are shown in Table 5.2.

Figure 5.5 shows the instantaneous vorticity contours of the optimised case at *t* = 160. The vortex structures in this case can be seen to gradually reduce in magnitude as they move downstream. Close comparisons can be made with figure 5.3(b), which uses the same input parameters, but the analysis run to *t* = 80. It can be seen that there is no further progression of the vortex structures downstream during the time progression from *t* = 80-160.

Strouhal No.	0.08
Domain extent (Lx, Lr)	60, 6
Number of cells (millions)	1
Reynolds number	300

Table 5.2. Input parameters for the jet optimised case

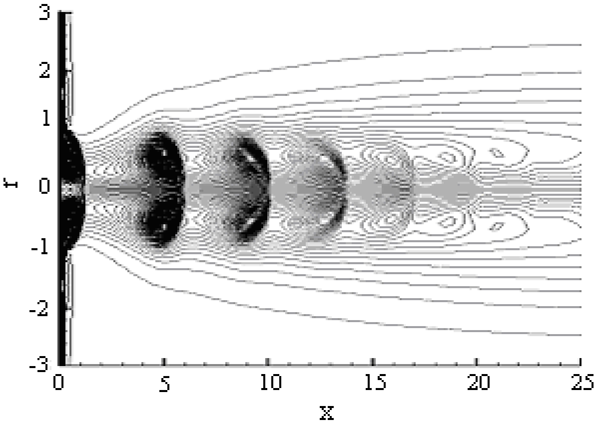

Fig. 5.5 Jet optimised case at *t* = 160.

Figure 5.6 shows the jet centreline velocity within a half actuator cycle of the optimised case, where the line styles used to represent different time instants are described in Table. 5.3. In figure5.6 the half actuation cycle can be seen to commence at t = 150, at which time the velocity at the orifice exit plane is negative. However, the velocity profile can be seen to rapidly increase and show a positive velocity moving away from the orifice at x = 1. This can also be seen to be the case at t = 152, when the actuator is at its 50% negative phase of -0.5. At both instances when the actuator is operating at its positive, blowing phase (t = 154 & t = 156) the streamwise velocity can be noted to drop rapidly in the region immediately downstream of the actuator orifice. However the jet flow field continues to exhibit a positive net streamwise velocity away from the orifice throughout the working domain in both these cases. This is also the case when the actuator is at its stagnant phase at t = 153. At this time instant the orifice velocity is zero, however the flow field continues to exhibit a positive downstream velocity. In figure 5.6 the unsteadiness of the flow field can be noted, as there are significant oscillations in the flow at locations near the jet orifice but less significantly oscillations at the downstream locations. This is because the downstream flow field does not respond as quickly to the oscillations at the inflow.

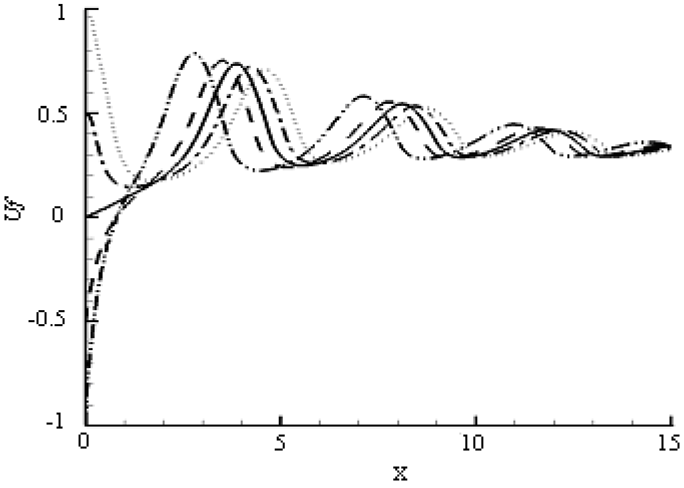

Fig. 5.6. Instantaneous jet centreline velocity for a half actuator cycle.

Designator	Time instant
—··—··—	*t* = 150
---------	*t* = 152
———	*t* = 153
—·—·—·	*t* = 154
…………	*t* = 156

Table 5.3. Velocity profiles for a half actuation cycle

5.3 TIME DEPENDENT JET EVOLUTION

An analysis of the evolution of a synthetic jet for the optimal case outlined in Section 5.2.3 at *Re* = 300 was carried out. For this analysis the simulation was stopped at regular time intervals so that the vorticity distributions and flow structures at the particular time instants could be analysed as they developed. In this case the analysis was stopped at six unit time intervals between the initial conditions at *t* = 0 and a time when a train of vortex structures was clearly present, at $t = 60$. Through this study the formation, convection of each vortex structure associated with the outward expulsion of fluid from the actuator is shown. Corresponding to the jet frequency of $St = 0.08$, the oscillating velocity profile at the domain inlet has completed almost five cycles when the time instant reaches $t = 60$.

The reduction in vortex intensity as the fluid slug moves downstream is also evident and is shown in a sequence of vorticity distributions in figure5.7. The synthetic jet flow established downstream of the jet exit plane is dominated by the time-periodic formation and advection of discrete vortices as can be seen in figure5.7. The outward ejection of five slugs of fluid, corresponding to five oscillations of the actuator is presented. From these figures it is clear to see that the initial vortex produced after the actuator has been activated is present and begins to move away from the orifice at $t = 20$. As can be seen in figure5.7(a) no discernible vortex structures are present in the flow at $t = 10$.

In figure 5.7 the initial vortex can be seen to continue to move downstream and is not appreciably affected by fluid being drawn into the actuator during its suction stroke. As time advances subsequent vortex structures can be seen to be developed by the actuator at each outward ejection phase. Each of these subsequent vortices can be seen to form behind the preceding vortex and to travel downstream with it.

As each vortex moves downstream it can be seen to reduce in intensity as it slowly dissipates. As was shown in figure5.5 these structures have almost completely dissipated at $x = 20$ due to mixing with the ambient background fluid [Jiang *et al.* 2006]. At this point they can be determined to no longer being phased locked with the actuator oscillation [Smith & , Glezer 2005].

5.4 JET CENTRELINE VELOCITY HISTORY

In order to further indicate the periodic behavior of the flow field at a later stage of the flow field evolution, the centreline velocity history of this case after t = 80, for two locations x = 0 and x = 15 respectively was examined (figure 5.8). The periodic variation at the domain inlet x = 0 reflects the zero mean velocity of the synthetic jet and therefore a zero net mass flux. At a slightly downstream location x = 15, the flow shows a positive mean velocity, indicating a net momentum flux away from the orifice. In figure 5.8 it also can be observed that the velocity variation at a downstream location becomes smaller than that at the domain inlet, which is due to the mixing of the jet with the ambient background fluid.

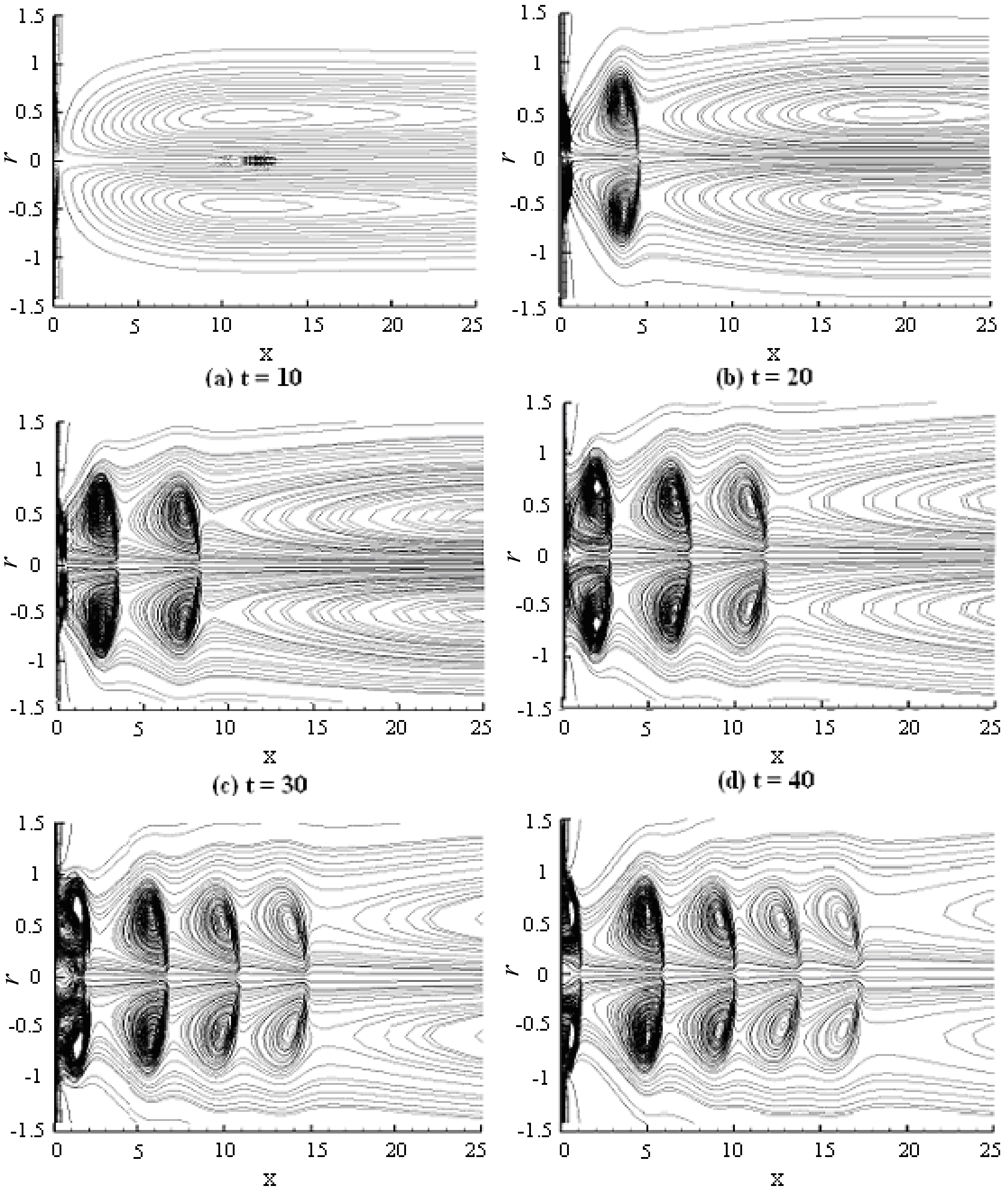

(a) t = 10

(b) t = 20

(c) t = 30

(d) t = 40

(e) t = 50

(f) t = 60

Fig. 5.7 Time evolution of the vortex structures of the optimised case.

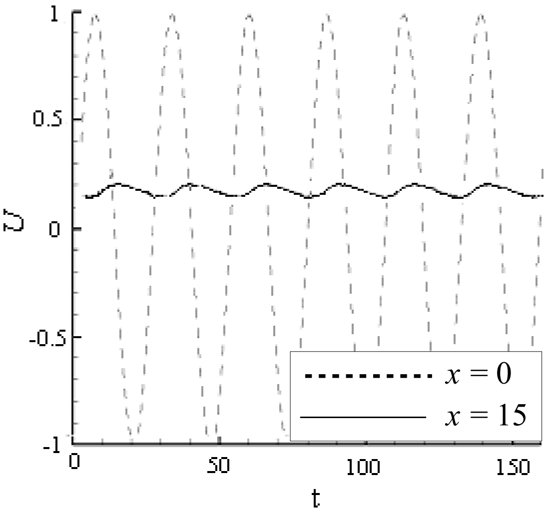

Fig. 5.8 Centreline velocity history of the axisymmetric case.

5.5 SUMMARY

The optimisation of various input parameters of an axisymmetric synthetic jet actuator has been carried out, along with a study into the formation and development of the vortex train associated with synthetic jets. A highly accurate direct numerical simulation based upon the Padé scheme has been used to compute vortex structures produced due to an oscillating velocity input applied at the jet orifice. Analysis of the mean centreline jet velocity at the orifice compared to data recorded at a downstream location has also shown the development of the positive streamwise momentum flux from the initial zero mean velocity of the jet actuator at the domain inlet.

The results attained have allowed a number of assertions to be made about the input characteristics which yield the optimal streamwise vortex train in terms of mass flux, vortex size and longevity.

Throughout the range of physical parameters examined, various vortex structures have been observed in the flow field. The input parameter which was noted to have the greatest effect on jet formation was the actuator oscillation frequency. At low actuation frequencies the vortex structures present in the flow field were noted to be of a larger size; however a true ‘vortex train’ was not produced as the vortex structures were noted to travel downstream as a lone vortex ring. At high frequencies the jet was noted to be under expanded, in the region near the actuator. In this case vortex structures in the flow field were less coherent and did not persist in the downstream region. As previously stated, this has been determined to be due to re-ingestion of the expelled fluid from the actuator on the subsequent suction stroke. More importantly, the results showed that synthetic jets with zero mean velocity at the inflow behave significantly differently from jets with non-zero mean velocity at the inflow. For a synthetic jet with zero mean velocity at the inlet, the jet developed significant vortex structures at much lower frequencies than comparable pulsed jets.

Investigation into the effect of varying the Reynolds number showed the propagation of the vortex structures further downstream with higher Reynolds numbers, as expected. Analysis of the evolution of the optimised jet case at regular time intervals shows the initial development and propagation of the individual vortex rings which make up the fully developed synthetic jet. The jet can be defined as being fully developed at a time when increasing the overall run time simulation will result in no further downstream propagation of the vortex structures present in the flow. The jet evolution study shows that in this optimised case the jet can be defined as fully developed beyond t = 60. The evolution study also shows the gradual decrease in vortex intensity of each individual vortex pair with time as they move downstream away from the orifice due to mixing of the jet flow with the ambient background fluid.

The centreline velocity of a fully developed synthetic jet shows that a mean positive velocity profile is present at a location downstream of the orifice to which a zero mean velocity profile has been applied. Although the magnitude of the velocity variation is reduced from the initial amplitude of the actuator, a clear non-zero mean velocity is present showing the net momentum flux of the fluid away from the orifice.

The complexity of the overall flow optimisation problem has been reduced by simply simulating the jet orifice as a sinusoidal oscillating velocity input, instead of a full simulation of the entire synthetic jet cavity flow. This initial investigation also uses an idealised axisymmetric configuration in place of a full three-dimensional direct numerical simulation. Due to the nature of the axisymmetric simulation, there is a lack of three-dimensional vortex stretching and interaction resulting in an inability to predict the flow features present due to the small scales. These small scales are of increasing importance in the downstream region, resulting in a possible premature dissipation of the vortex train in this region. However the results attained give a valuable insight into the formation and evolution of the synthetic jet along with optimal values for the actuator design.

CHAPTER 6

THREE-DIMENSIONAL TEST CASES

6.1 INTRODUCTION

The axisymmetric test cases analysed in Chapter 5 give a good qualitative view of the development of the vortex structures present in the flow. However due to the 3*D* nature of the flow, it is useful to analyse the 3*D* vortex topology. In flows that are effectively 3*D* the deformation and stretching of small regions of the fluid allows mixing and increases the rate of kinetic energy cascade when compared to 2*D* solutions.

Identical input parameters were used with a *3D* version of the code in a rectangular 3*D* domain, in order to directly compare the vortex structures present in the flow field. The spreading rate of the jet was shown by Kotapati & Mittal *et al.* [2007] to be directly related to the presence of three-dimensionality. Therefore a useful insight can be drawn into these effects by directly comparing the axisymmetric and 3*D* flow fields.

The actuator orifice used for the 3*D* car is circular in shape and has a non-dimensionalised diameter of 1. The coordinate system is defined as follows: The origin is defined at the bottom corner of the domain. The y and z coordinates are defined along both spanwise directions, while the x coordinates are defined in the streamwise direction. The extents of the coordinate domain, non-dimensionalised by the orifice diameter are: $x = 12$, y = 12, z = 30. The actuator orifice is located flush with the y,z coordinate plane.

The Reynolds number used for the simulation is $Re = 300$ and the time advancement uses a CFL number of 10. The actuator is based on a sine wave oscillation with a non-dimensionalised frequency of $St = 0.08$.

The 3*D* computational grid uses 256 grid points in both the y and z coordinate directions and 512 grid points in the x streamwise direction. Thus giving a total of over 33.5 million grid points

*Jet frequency (*St*)*	0.08
Domain extent (*Lx, Ly, Lz*)	30, 12, 12
Number of cells (millions)	33.5
Reynolds number (*Re*)	300

Table.6.1. Input parameters for the 3*D* jet case

6.2 VORTEX STRUCTURES PRESENT IN THE flow field

Three dimensional vortex structures are identified by plotting a 3*D* isosurface of the velocity gradient. In this method the vortex structures are identified as regions where rotation is dominant over strain, and so they correspond to circular streamlines in the planes normal to the axis of these structures [Schoppa & Hussain, 2000]. Figure 6.1 depicts the isosurfaces produced from a fully evolved 3*D* synthetic jet at $t = 165$. The figure clearly depicts the train of vortex structures formed by the actuator in the presence of the normally quiescent background fluid. This vortex train can be seen emanating from the actuator orifice on the left hand side of the plot.

As can be seen from figure6.1(a) and figure6.1(b), the structures present in the flow exhibit a clear asymmetry around the jet centre-line. From figure6.1(b) it can be noted that there is an unexpectedly large gap in the vortex train between the first and second vortex rings. This can be noted between the structure present adjacent to the orifice, at the left hand side of the plot and the second structure in the *x* direction.

Figure 6.1(c) and figure 6.1(d) represent the same flow solution and viewing perspective as figure 6.1(a) and figure 6.1(b), the altered variable being the enstrophy value used for post-processing the data. In these figures an enstrophy value of 0.5 was used, compared to a value of 1 which was used in figure 6.1(a) – figure 6.1(c). This reduction in enstrophy value serves to further highlight the extent of the vortex features associated with the jet flow field. By further decreasing this enstrophy value to 0.25 and then to 0.1, (figure 6.1(g), figure (6.2(h) & figure 6.1(i)), the full extent of the 3*D* jet flow becomes visible.

Figure 6.1(f) is an isometric enhancement of a section of the vortex train at an enstrophy value of 0.5. In this figure the gradual dissipation of the vortex train as it moves downstream can be noted. The ring-like nature of the structures can be seen from the second structure, which is further downstream, and thus of lower intensity than the first. The third structure on the right-hand side of the figure can be seen to have been almost completely dissipated and is largely indistinguishable from the background fluid.

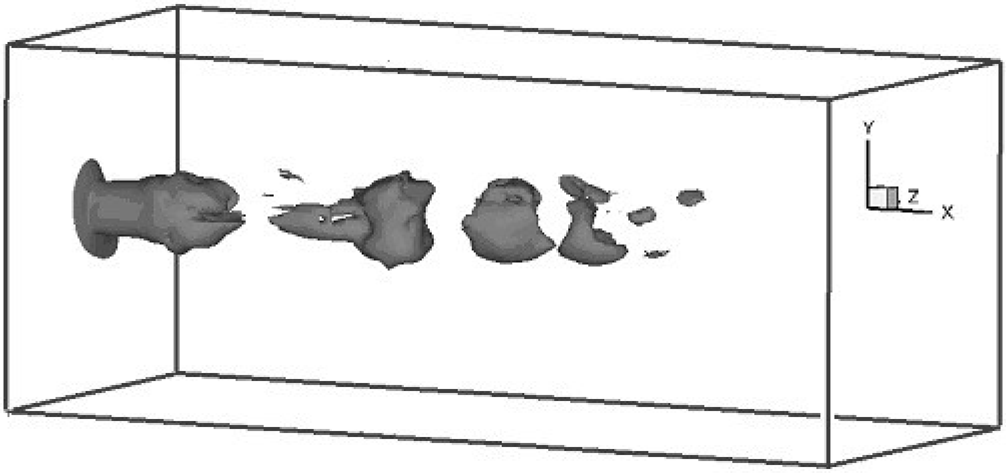

Fig. 6.1(a) Isometric view of the entire flow field

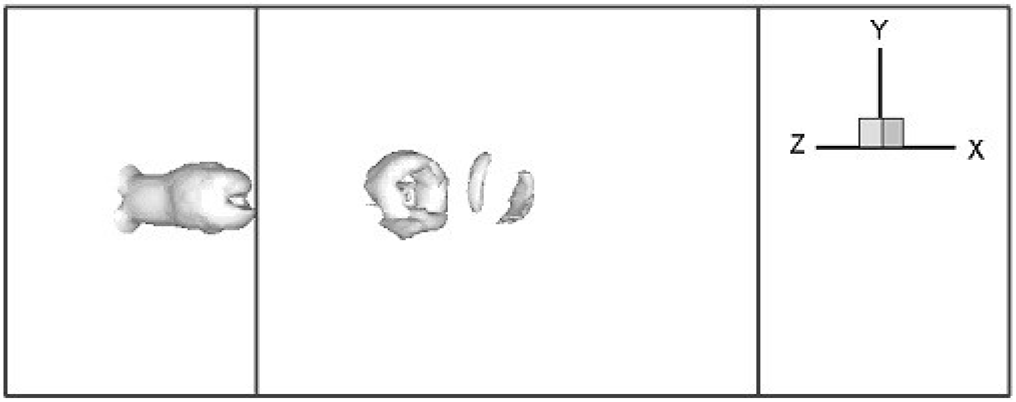

Fig. 6.1(b) Partially rotated view of the flow field with an imposed enstrophy value of 1.

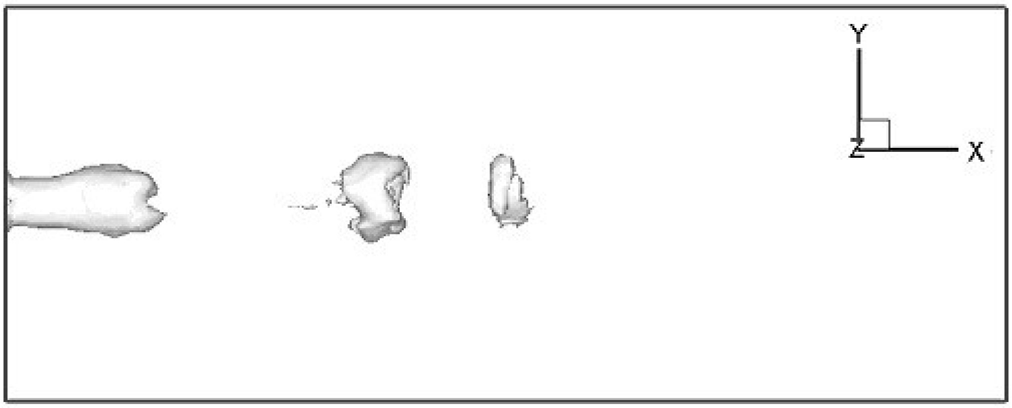

Fig. 6.1(c) Elevation of the flow field with an imposed enstrophy value of 1.

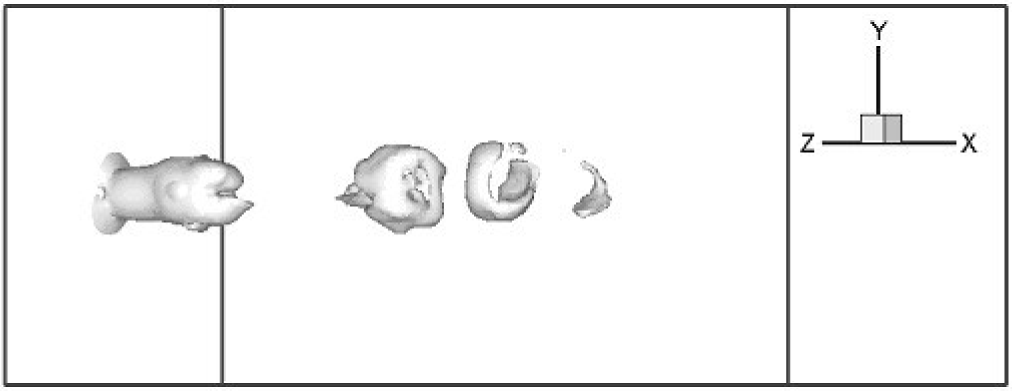

Fig. 6.1(d) Partially rotated view of the flow field with an enstrophy value of 0.5.

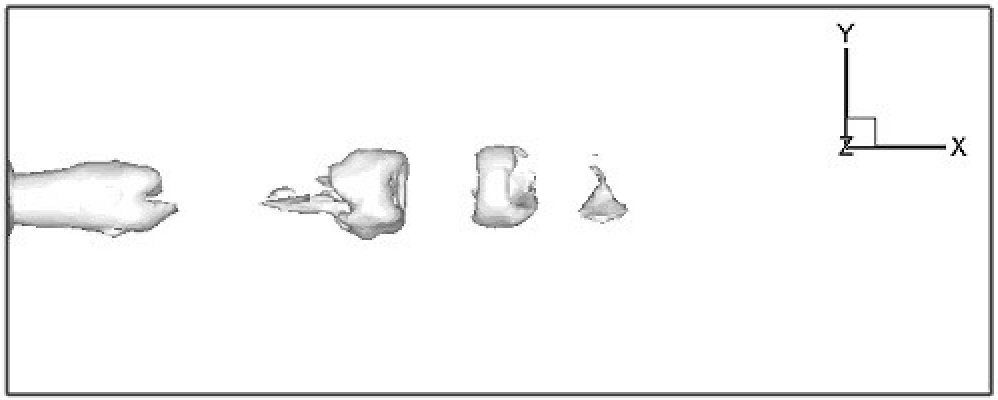

Fig. 6.1(e) Elevation of flow field with an imposed enstrophy value of 0.5.

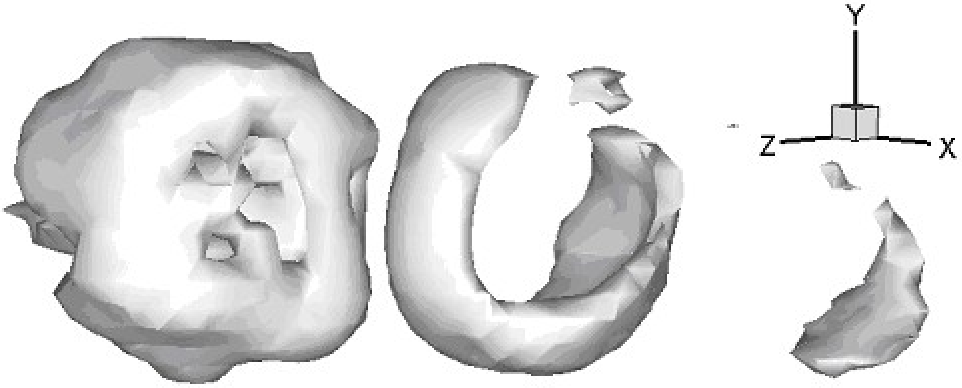

Fig. 6.1(f) Magnification of the vortex rings present with an enstrophy value of 0.5.

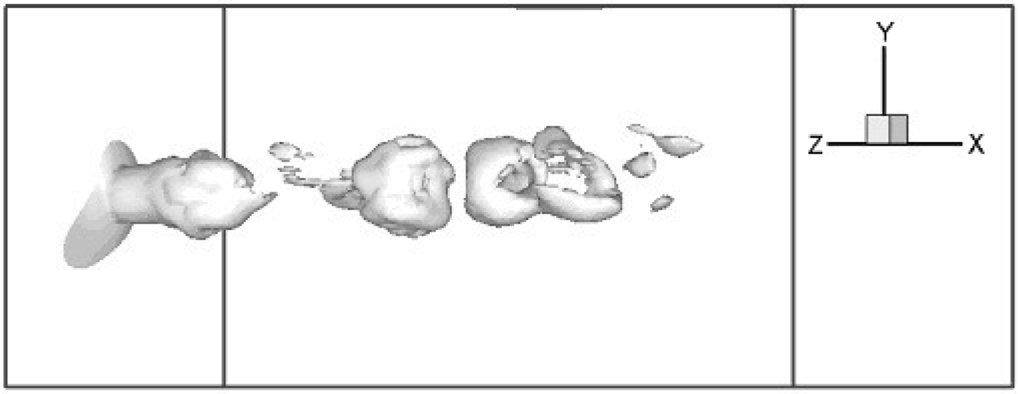

Fig. 6.1(g) Partially rotated view of the flow field with an enstrophy value of 0.25.

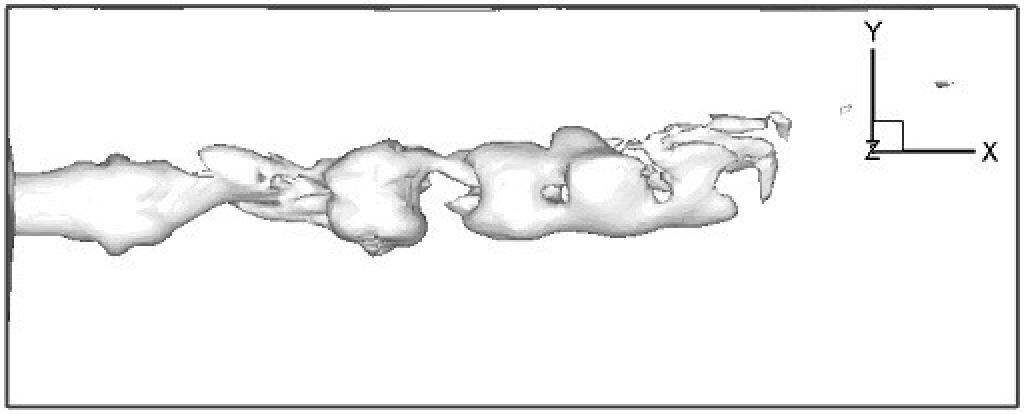

Fig. 6.1(h) Elevation of flow field with an imposed enstrophy value of 0.1.

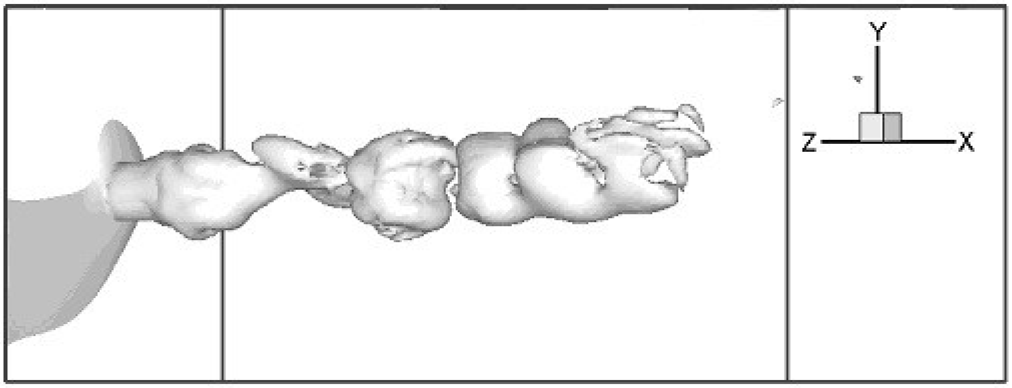

Fig. 6.1(i) Partially rotated view of the flow field with an enstrophy value of 0.1.

Fig. 6.1 Isosurfaces of the vortex structures of the three-dimensional case.

Figure 6.2 represents a streamwise slice through the fully developed flow field at two downstream locations, $x = 11$ and $x = 15$, showing contours of velocity. These x coordinates were chosen so as the slice bisects the 2nd and 3rd vortex structures produced by the actuator at $t = 165$. From figure 6.2(a) and figure 6.2(b) the 'ring-like' structures of each vortex ring are clearly visible. The reduction in intensity as the vortex structures move downstream and the spreading of the vortex ring is also clearly visible when comparing figure 6.2(a) and figure 6.2(b). The asymmetrical nature of these vortex structures can also be noted from these figures.

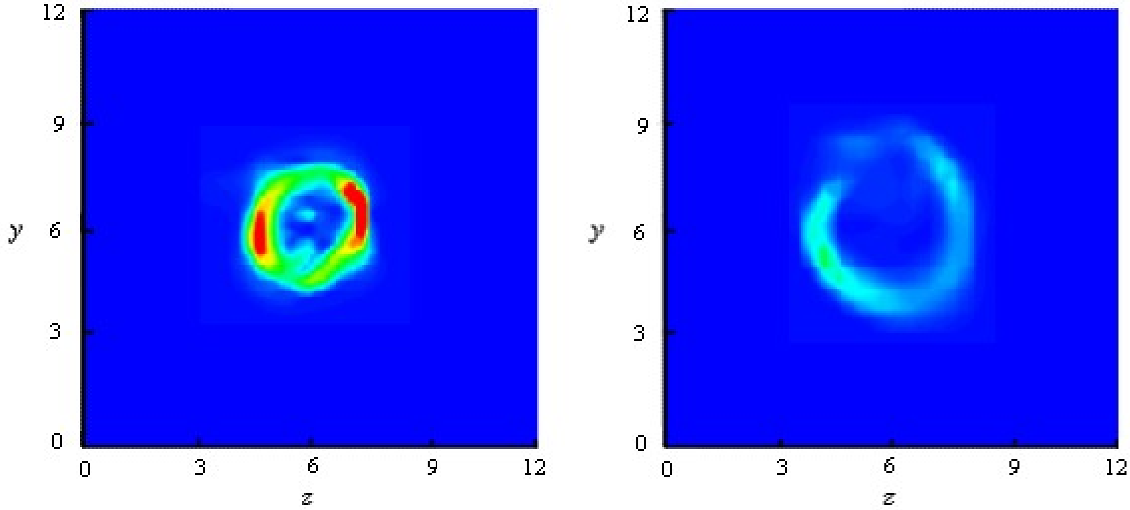

Fig. 6.2(a) $x = 10$ **Fig. 6.2(b)** $x = 15$

Fig. 6.2 Slices showing vortex rings present at $x = 10$ & $x = 15$

The isosurfaces representing the complete jet flow field as shown in figure 6.1 give a very good representation of the nature of the jet flow and the vortices present. However the interior structure of the jet core is concealed as the isosurfaces only display the outer faces of the vortex structures. In order to gain an insight into the interior structure of the jet core, seven evenly spaced slices were taken through the jet core at *z* = 4.5, 5.0, 5.5, 6.0, 6.5, 7.0, 7.5, thus dissecting the entire jet flow and enabling a more detailed view of the internal flow structures. Each of the seven enstrophy slices is displayed in figure 6.3.

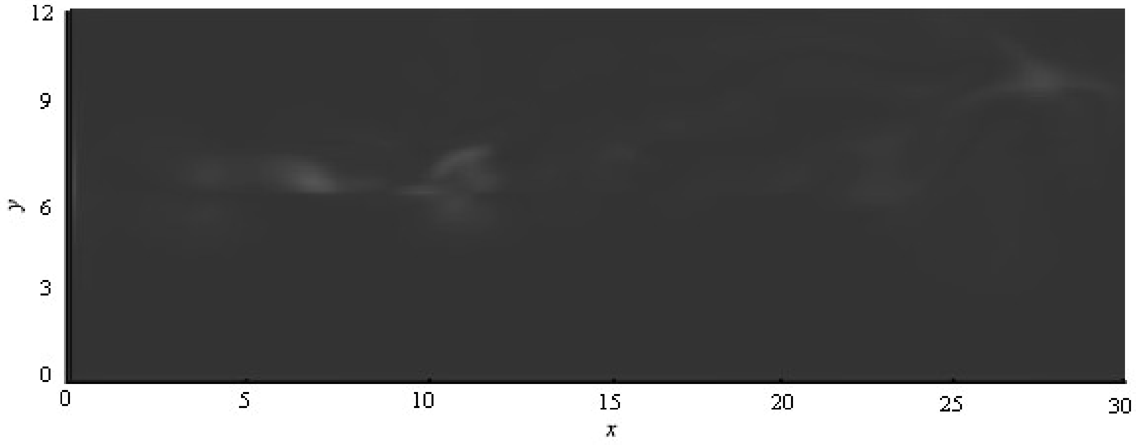

Fig. 6.3(a) *z* = 4.5 slice showing enstrophy

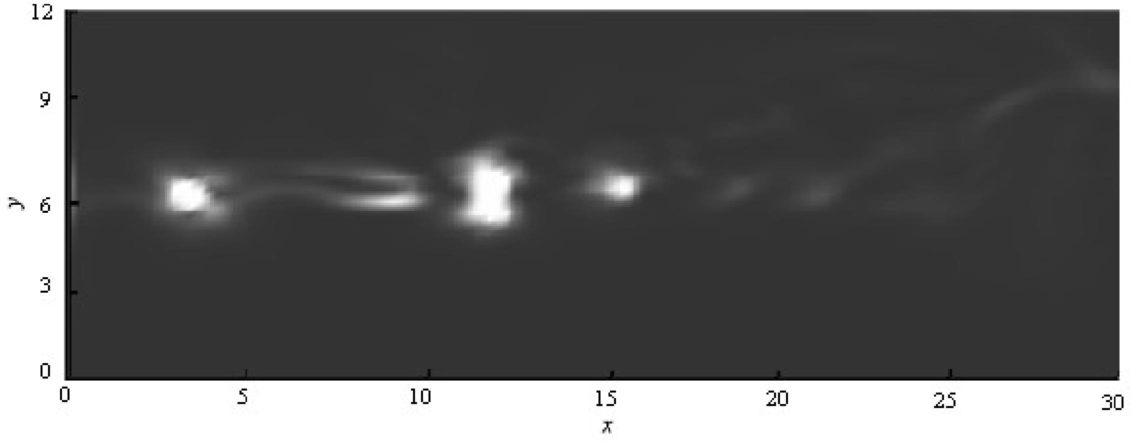

Fig. 6.3(b) *z* = 5 slice showing enstrophy

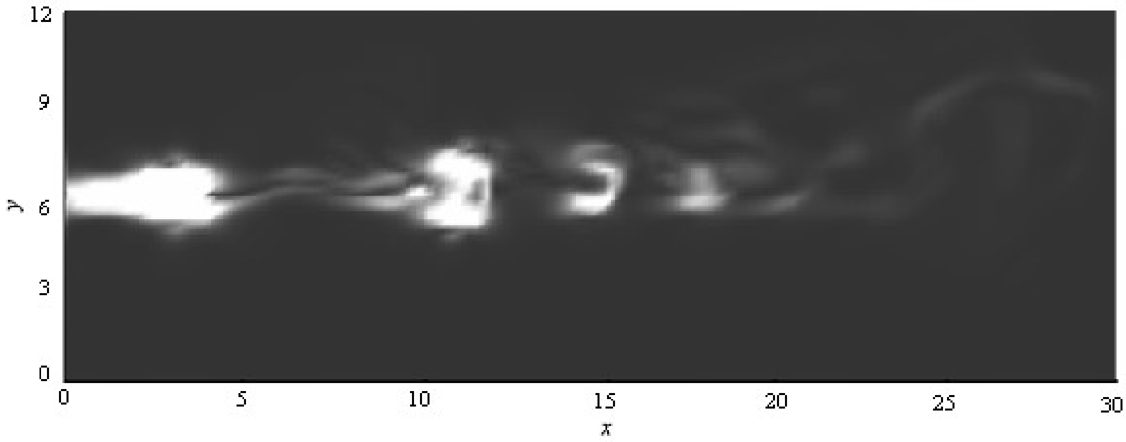

Fig. 6.3(c) *z* = 5.5 slice showing enstrophy

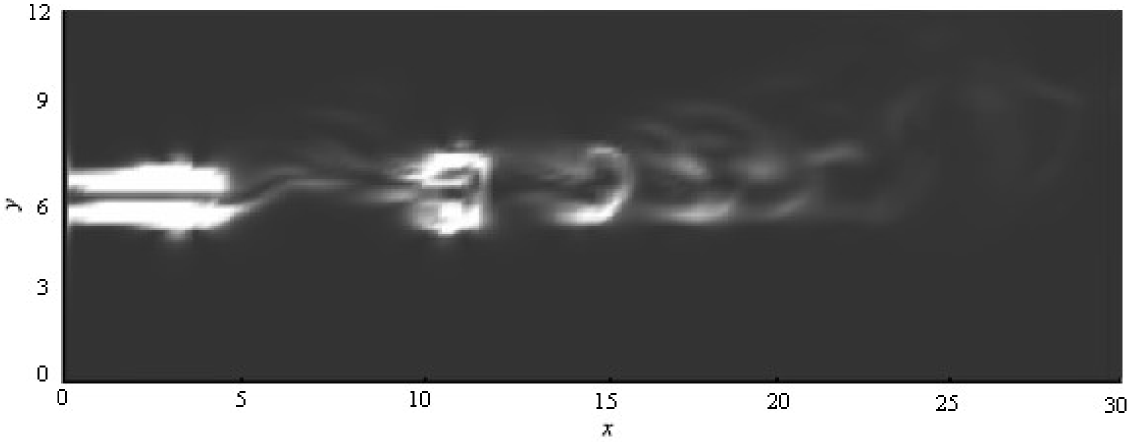

Fig. 6.3(d) *z* = 6.0 slice showing enstrophy

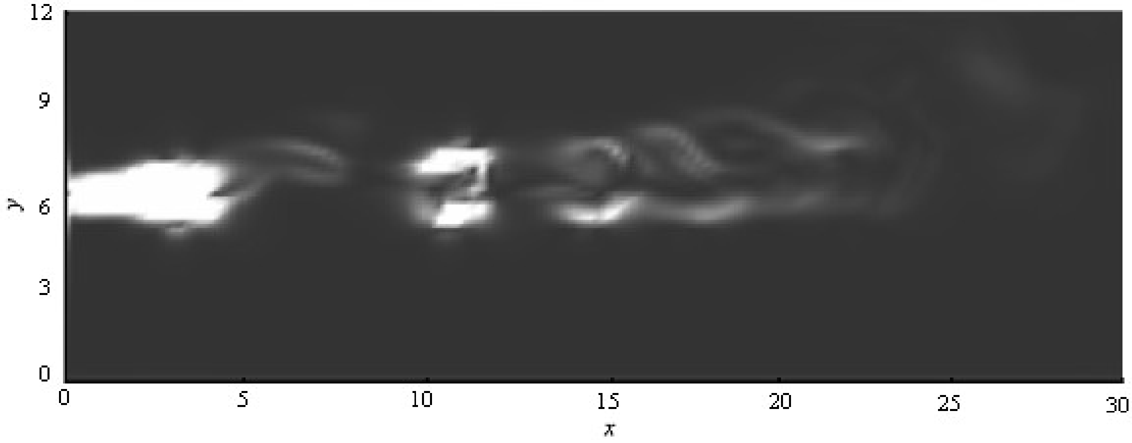

Fig. 6.3(e) *z* = 6.5 slice showing enstrophy

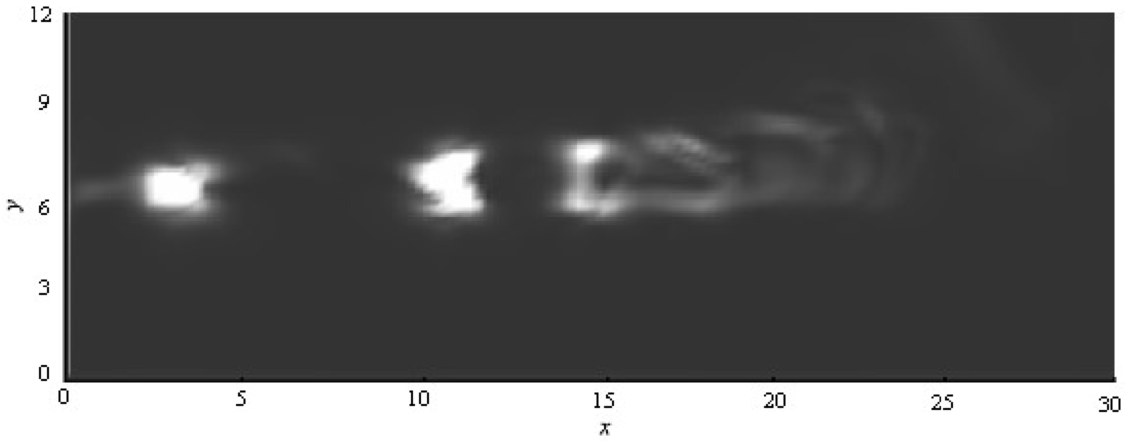

Fig. 6.3(f) z = 7.0 slice showing enstrophy

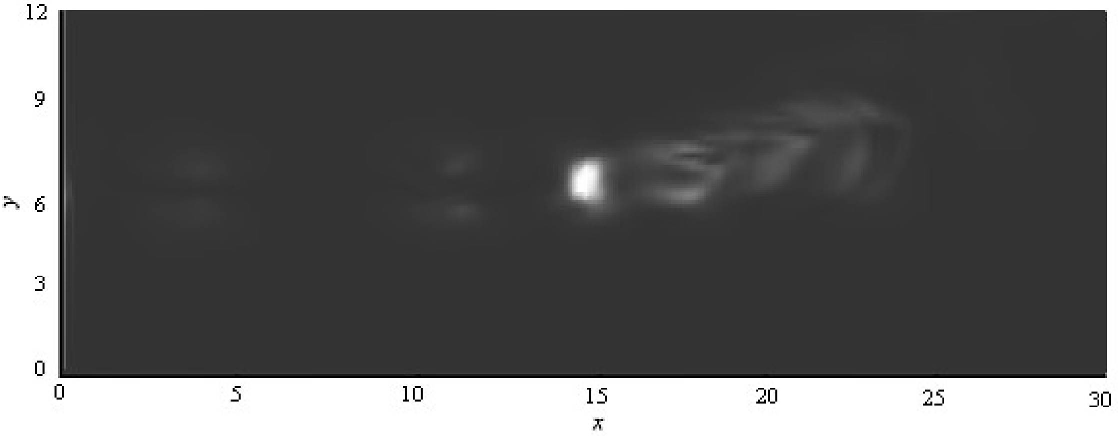

Fig. 6.3(g) z = 7.5 slice showing enstrophy

Fig.6.3 Enstrophy slices of the fully developed jet case at t =165

From figure 6.3(a) & figure 6.3(g) it is clear that the extent of the jet flow in the lateral 'z' direction is almost completely contained within the slices at z = 4.5 and z = 7.5. The jet flow is very weak in the z = 4.5 and z = 7.5 slices suggesting that it is near the outer edge of the core jet flow. This is especially the case in figure 6.3(a) at z = 4.5 where the jet flow is almost indiscernible from the background fluid. The 'ring-like' nature of the synthetic jet flow field was also noted in figure 6.3(c), in this case a clearly defined central core of the jet can be seen adjacent to the actuator orifice extending downstream to $x = 5$. This dark central region surrounded by the highlighted jet flow clearly shows the formation of the initial vortex ring occurs in the region immediately downstream of the actuator orifice. A further developed vortex ring can be noted in figure 6.3(c), figure 6.3(d) and figure 6.3(e) extending from $x = 10$ to $x = 12$.

6.3 JET CENTRELINE VELOCITY

As was the case with the axisymmetric analysis, the jet centreline velocity over a complete actuator cycle has been analysed. From analysis of the jet evolution study it was determined that the flow would be sufficiently developed at $t = 60$ to give a good insight into the flow physics. The jet centreline velocity profile for the start of the next actuation cycle at $t = 75$ was also included in these results for completeness.

The jet centreline velocity for the eight time periods is displayed in figure 6.4. For ease of understanding the entire actuation cycle has been divided into two separate plots. Figure 6.4(a) shows the time instances from $t = 62.5$ up to $t = 68.75$. Over this time period the actuator goes from its fully positive, or outward stroke at $t = 62.5$, to a half negative, or suction stroke at $t = 68.75$. It can be noted that the same overall flow pattern of the jet centreline velocity, as was seen in the axisymmetric case can be seen in this $3D$ study. The jet velocity for the fully positive case at $t = 62.5$ can be seen to increase slightly immediately downstream of the orifice, before rapidly dropping in the region $2 < x < 3$. For all other cases in figure 6.4(a) the jet velocity can be seen to increase rapidly in the region immediately downstream of the orifice. As was noted by Fugal, Smith & Spall [2005] a stagnation point forms between the orifice and the first vortex pair on the suction portion of the cycle. At this location the streamwise velocity component (*u)* is equal to zero. As with the axisymmetric case the streamwise centreline velocity magnitude can be seen to decrease with time as it moves further away from the orifice. However the frequency and pattern of the velocity profile of the 3*D* case is far less regular than that of the axisymmetric case.

Figure 6.4(b) shows the second half of the actuation cycle. In this case the flow is progressing from 100% suction at *t* = 70.3125, to the end of the actuation cycle at *t* = 75. In this region the flow structures show the same oscillating profile as before. In this case the oscillating profile can also be seen to degrade to a near-zero value beyond a point at *x* = 21. Figure 6.4(c) depicts the combined overall jet centreline velocity for the complete actuation cycle. From this figure, the gradual reduction in intensity of the jet centreline velocity and the corresponding vortex structures as they move downstream becomes apparent.

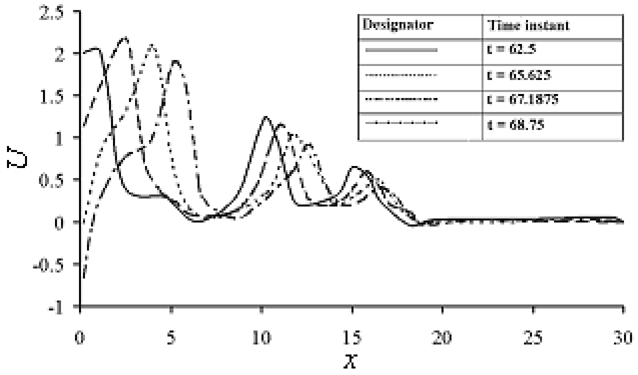

Fig. 6.4(a) Jet centreline velocity, *t* = 62.5 to *t* = 68.75

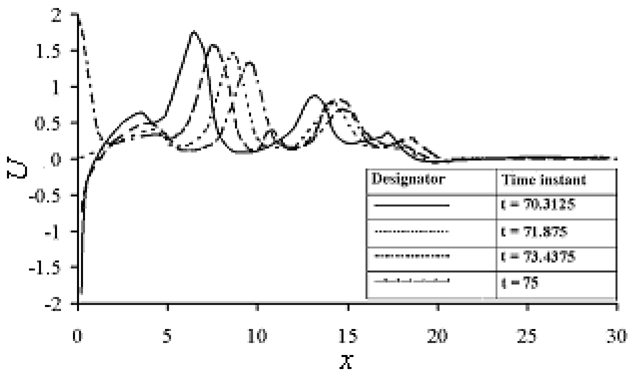

Fig. 6.4(b) Jet centreline velocity, $t = 70.3125$ to $t = 75$

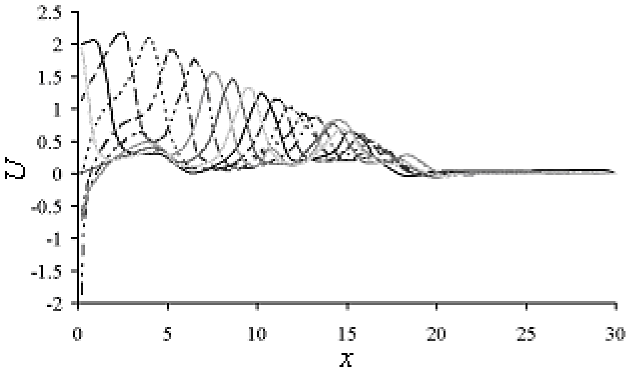

Fig. 6.4(c) Overall Jet centreline velocities, $t = 62.5$ to $t = 75$

Fig. 6.4 Jet centreline velocities.

6.4 THREE-DIMENSIONAL JET EVOLUTION

Following on from the evolution study of the axisymmetric synthetic jet, a comparative study was carried out for the 3*D* case. For this analysis the simulation was stopped at the same time intervals as outlined in the axisymmetric study in Chapter 5.3. The vorticity distributions and flow structures at the particular time instants were analysed.

As can be seen in figures 6.5 to figure 6.12, the formation of a vortex train is clear after $t = 30$. The vorticity magnitude of the vortex cores decreases and each vortex structure can be seen to spread out into the far-field as it moves downstream. As was shown in figure 6.1 the vortex structures present have almost completely dissipated at $x = 25$ due to mixing with the ambient background fluid [Kotapati, 2007].

As with the axisymmetric case, the 3*D* synthetic jet flow established above the jet exit plane is dominated by the time-periodic formation and advection of discrete vortex structures. Successive vortex rings can be seen to form at the actuator orifice and to move downstream under their own momentum. The regions of reverse flow around the outer edges of each vortex structure are evident in the contour plots as the regions of dark navy contour. The large amount of flow asymmetry present in the 3*D* analysis is also clear.

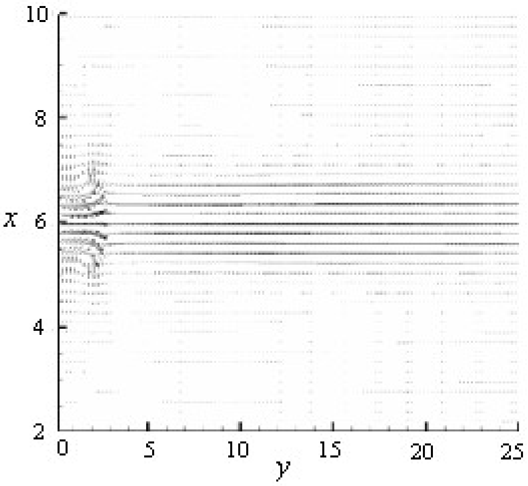

Fig. 6.5(a) Velocity vectors of the Three-dimensional jet evolution at *t* = 15

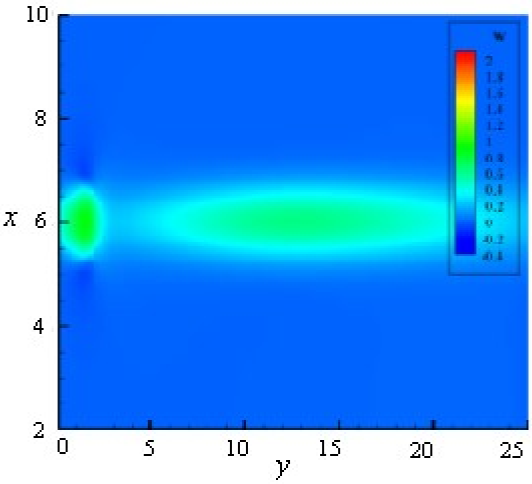

Fig. 6.5(b) Velocity contours of the Three-dimensional jet evolution at *t* = 15

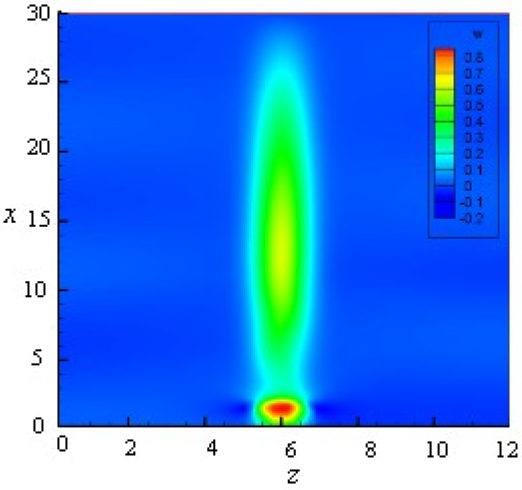

Fig. 6.5(c) Plan view of the velocity contours of the three-dimensional jet evolution at *t* = 15

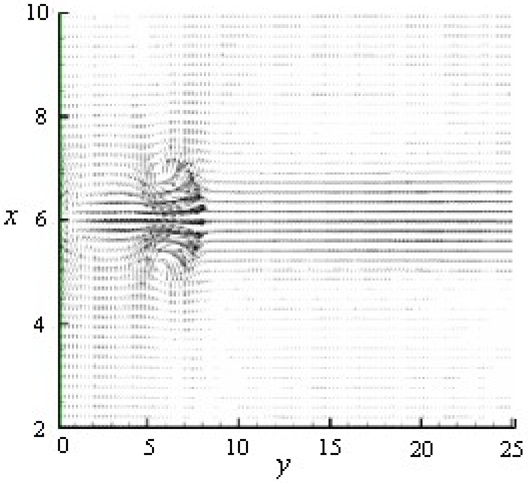

Fig. 6.6(a) Velocity vectors of the three-dimensional jet evolution at *t* = 30

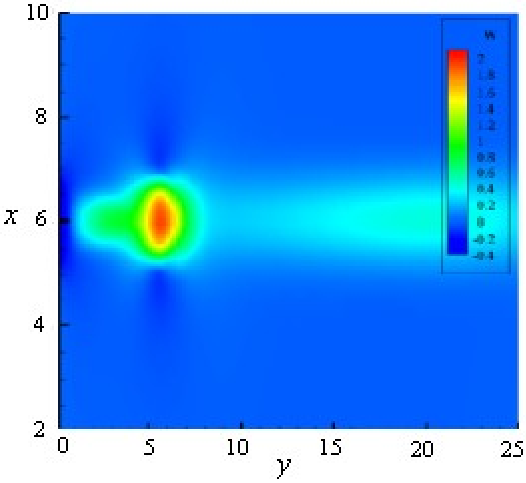

Fig. 6.6(b) Velocity contours of the three-dimensional jet evolution at *t* = 30

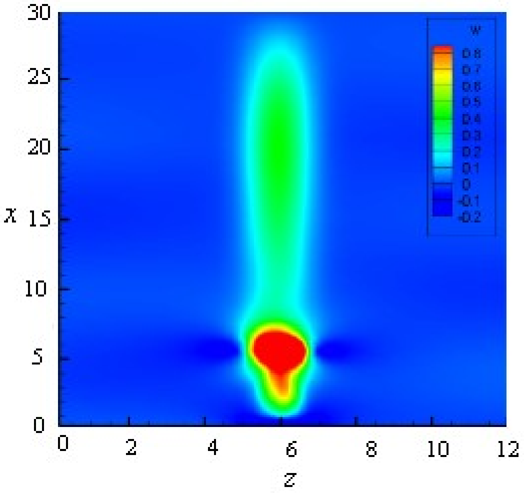

Fig. 6.6(c) Plan view of the velocity contours of the three-dimensional jet evolution at *t* = 30

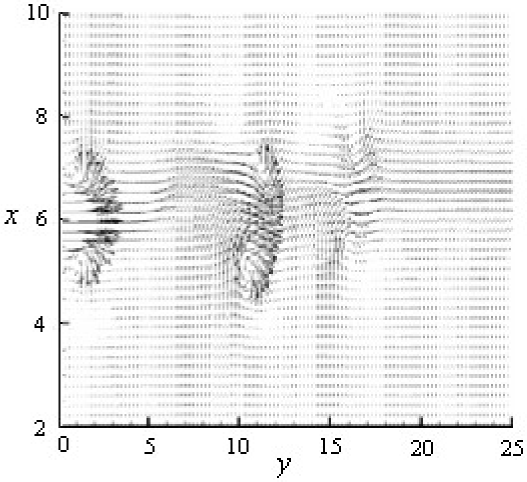

Fig. 6.7(a) Velocity vectors of the three-dimensional jet evolution at *t* = 50

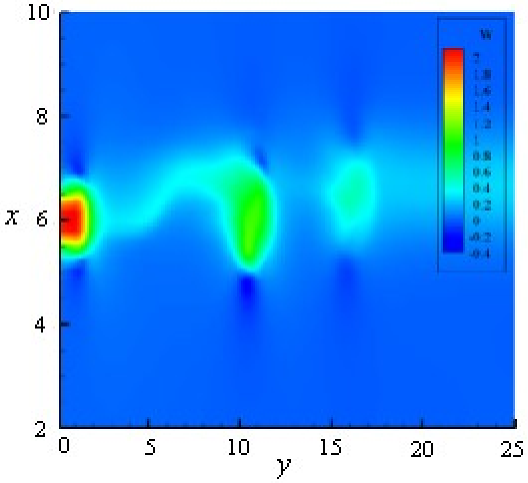

Fig. 6.7(b) Velocity contours of the three-dimensional jet evolution at *t* = 50

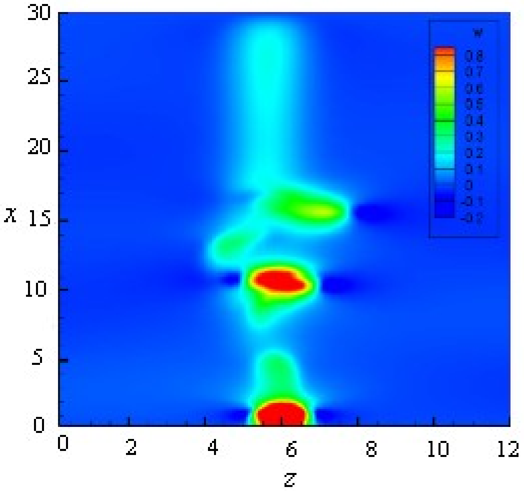

Fig. 6.7(c) Plan view of the velocity contours of the three-dimensional jet evolution at *t* = 50

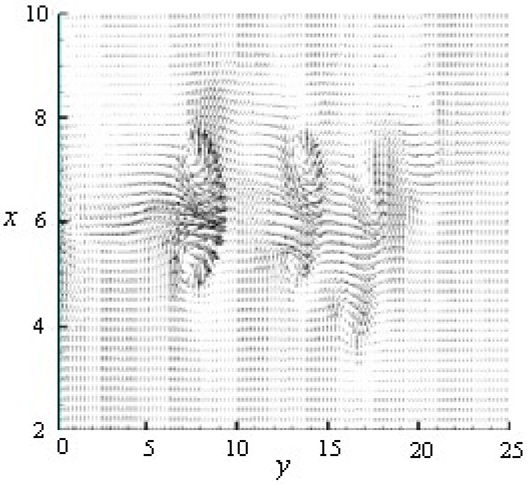

Fig. 6.8(a) Velocity vectors of the three-dimensional jet evolution at $t = 70$

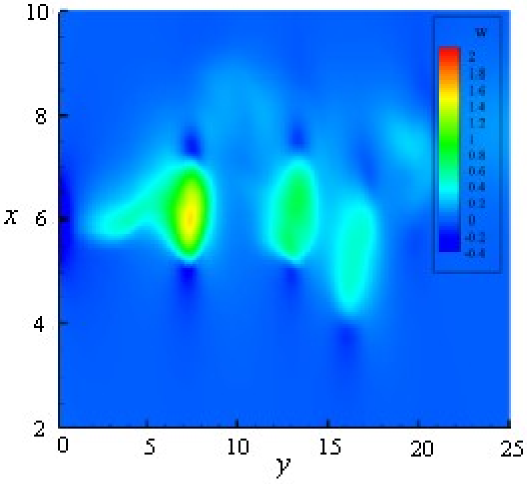

Fig. 6.8(b) Velocity contours of the three-dimensional jet evolution at $t = 70$

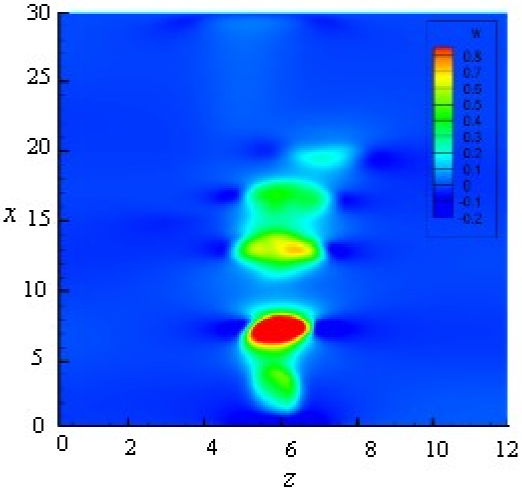

Fig. 6.8(c) Plan view of the velocity contours of the three-dimensional jet evolution at $t = 70$

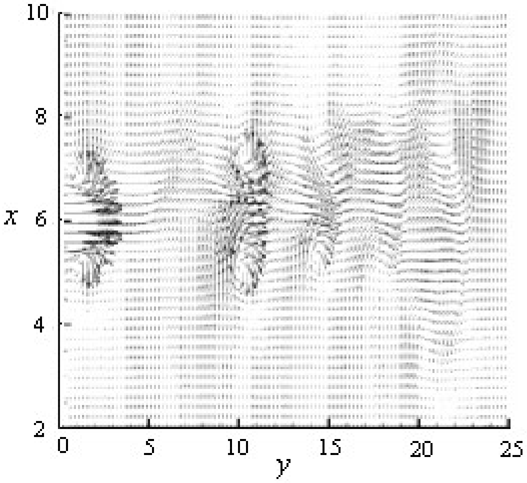

Fig. 6.9(a) Velocity vectors of the three-dimensional jet evolution at $t = 100$

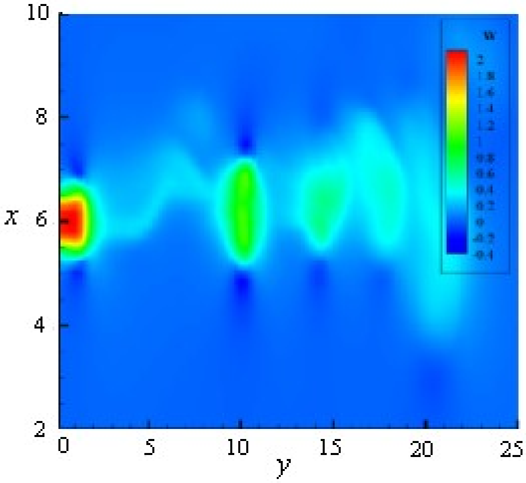

Fig. 6.9(b) Velocity contours of the three-dimensional jet evolution at $t = 100$

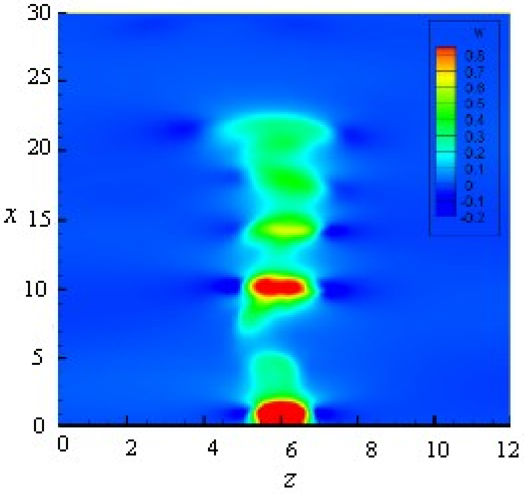

Fig. 6.9(c) Plan view of the velocity contours of the three-dimensional jet evolution at $t = 100$

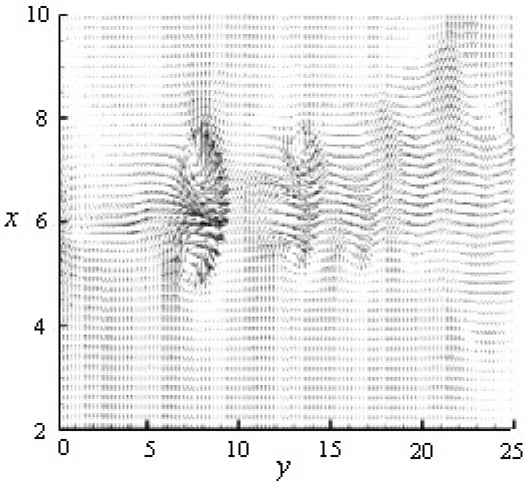

Fig. 6.10(a) Velocity vectors of the three-dimensional jet evolution at $t = 120$

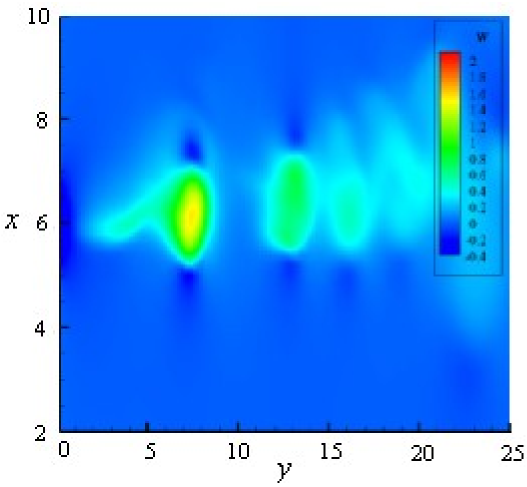

Fig. 6.10(b) Velocity contours of the three-dimensional jet evolution at $t = 120$

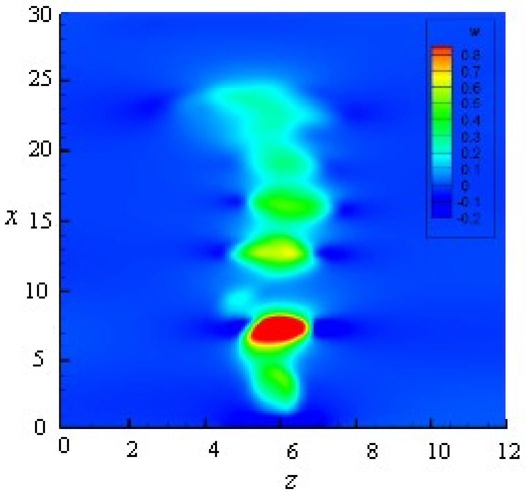

Fig. 6.10(c) Plan view of the velocity contours of the three-dimensional jet evolution at $t = 120$

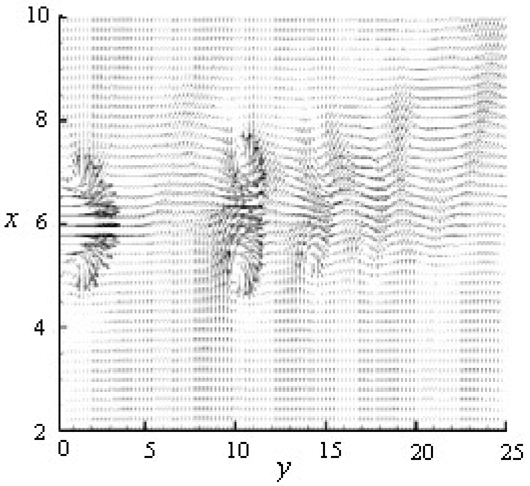

Fig. 6.11(a) Velocity vectors of the three-dimensional jet evolution at $t = 150$

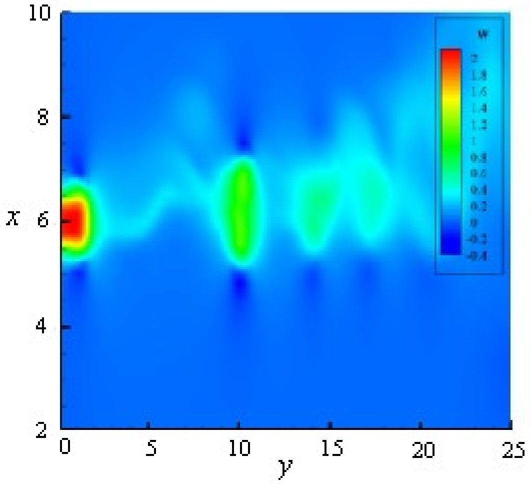

Fig. 6.11(b) Velocity contours of the three-dimensional jet evolution at $t = 150$

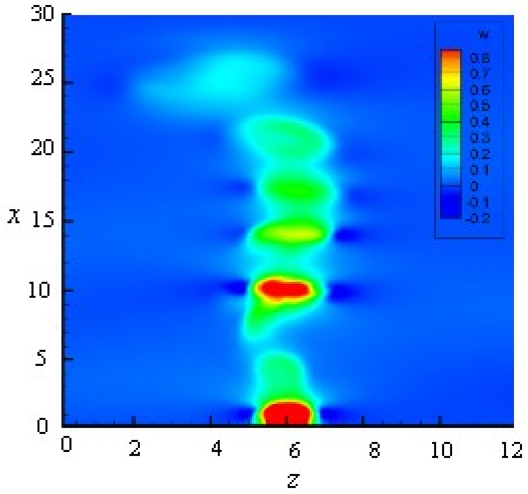

Fig. 6.11(c) Plan view of the velocity contours of the three-dimensional jet evolution at $t = 150$

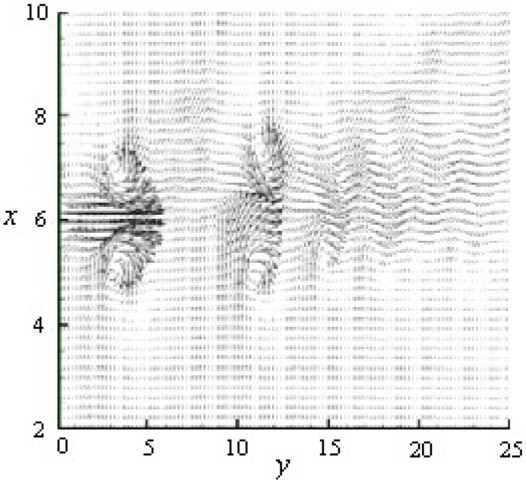

Fig. 6.12(a) Velocity vectors of the three-dimensional jet evolution at t = 165

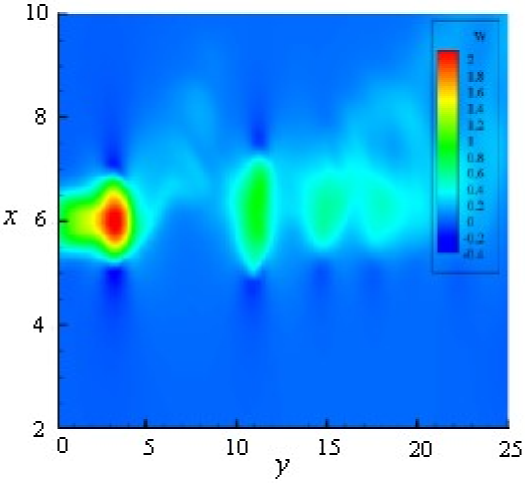

Fig. 6.12(b) Velocity contours of the three-dimensional jet evolution at t = 165

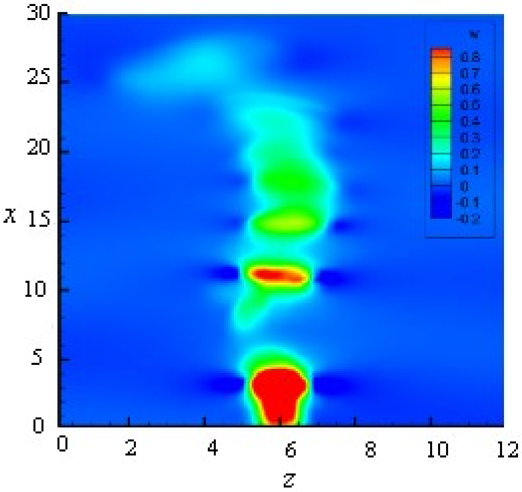

Fig. 6.12(c) Plan view of the velocity contours of the three-dimensional jet evolution at t = 165

6.5 TIME AVERAGED FLOW FIELD RESULTS

In order to further understand the jet flow field, both the time-averaged jet velocity and the spreading of the jet in the cross-streamwise (z) direction have been calculated. These results were taken from a point where the flow field was sufficiently well developed for there to be a true jet-like flow present at $t = 50$ and flow field values were averaged up to $t = 165$.

In figure 6.13 the time averaged jet width (W) can be seen to increase linearly up to a streamwise distance of $x = 10$. From $10 < x < 15$ a decrease in averaged jet width can be seen. This region of decreased W can be noted to be immediately downstream of the region described in Chapter 6.2 to have an unexpectedly large gap between successive vortex cores. This decrease in W in figure 6.13 can also be related to an increase in average streamwise velocity as shown in figure 6.14. It is therefore suggested that the jet perturbation described in Chapter 3.6 directly causes a disturbance to the vortex train in the region between $5 < x < 10$. The time averaged effect of this disturbance is a reduction in the mean streamwise velocity and an associated increase in W in this region. Beyond $x = 15$ the jet flow field can be seen to rapidly grow in the cross-streamwise direction as it mixes with the background fluid.

The time averaged centreline velocity for the same time period is shown in figure 6.14. As expected the averaged velocity profile increases rapidly immediately downstream of the orifice. However a sharp dip and then gradual increase in the velocity profile can be noted in the region $4 < x < 15$. It is in this region that the apparent gap between successive vortex structures was noted in Chapter 6.2, and as previously discussed, it is directly related to the imposed jet perturbation. To further understand the effect of the perturbation, velocity vector plots taken at $x = 10$ and $x = 15$ are shown in figure 6.15. They clearly show strong cross-streamwise flow present in the region around $x = 10$. It is proposed that it is this flow that causes the apparent lack of discernible flow structures present in this region, along with the corresponding drop in centreline velocity.

This flow feature was also noted to be present in $3D$ synthetic jet analysis carried out by Cui & Agarwal [2006]. In their study hot-wire anemometry was compared to a number of numerical modelling schemes. While the CFD modelling methods they used, such as Reynolds Averaged Navier-Stokes (RANS) or Large Eddy Simulation (LES) did not pick up this flow feature, their hot-wire anemometry results predicted the same patten of averaged velocity profile as shown in figure 6.14. This suggests that the disturbance to the flow field caused by the jet perturbation is comparable to that seen in experimental applications.

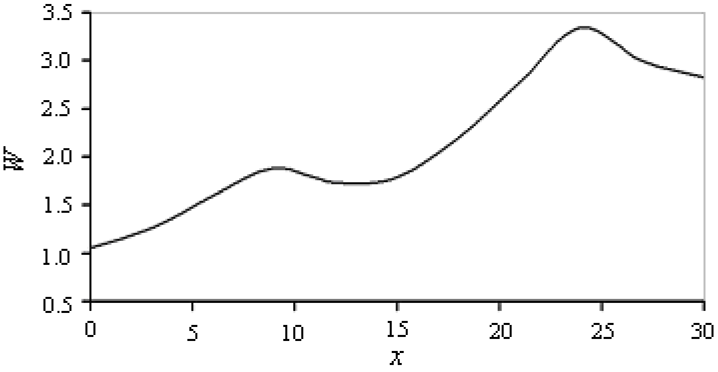

Fig.6.13 Non-dimensionalised jet width.

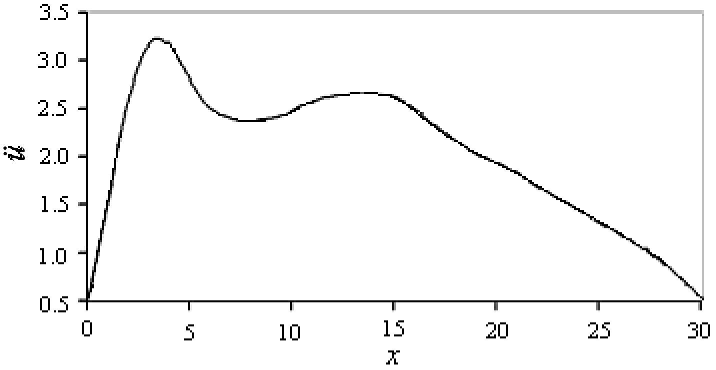

Fig. 6.14 Time averaged centreline velocity from t = 50 to t = 165

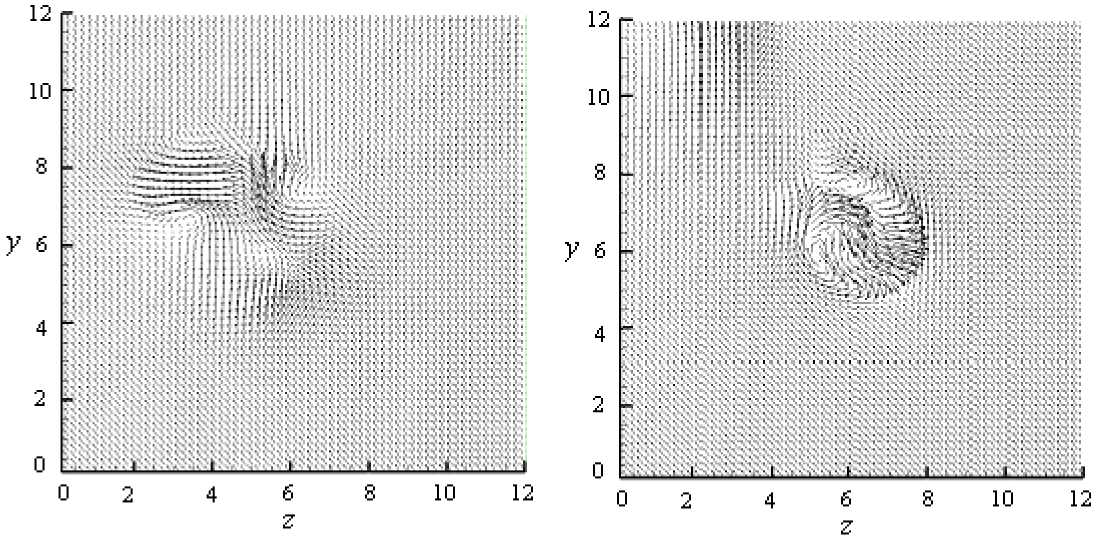

Fig6.15(a) x = 10

Fig6.15(b) x = 15

Fig.6.15 Cross-streamwise vector plots at x = 10 and x = 15

6.6 EFFECTS OF VARYING THE JET PERTURBATION

In order to break the jet centreline symmetry associated with the applied velocity inlet boundary conditions, an oscillating velocity perturbation was added to the flow. This acts to give a more true life representation of the synthetic jet flow field by imposing an asymmetry to the flow field as has been noted in experimental studies by Smith & Glezer [2005]. This perturbation was initially applied at a frequency of $St = 0.32$, which is four times the frequency of the jet actuator itself. In order to deduce the overall effect of the perturbation on the flow field, independent of the main actuator frequency, the perturbation frequency was decreased to $St = 0.08$, while the main actuator frequency was kept constant at $St = 0.08$.

It is clear from comparing the centreline velocity profiles of the idealised axisymmetric case in figure 5.6 and the fully three-dimensional case in figure 6.4(c) along with the time averaged results in figure 6.13 & figure 6.14. that there is a strong drop-off in the velocity profile in the region $x = 5$ to $x = 12$. This is in the region where the 2nd peak of the oscillating velocity profile is present in the axisymmetric simulations. Other than the apparent abnormality present in the velocity profile in this region the typical trend of the slowly degrading oscillating velocity profile present in the axisymmetric is generally followed in the fully three-dimensional case. In the $x = 5$ to $x = 12$ region strong cross streamwise velocity vectors have been noted (figure 6.15) which can be associated with the lack of vortex structures in this region.

Figure 6.16 shows the initial jet flow field for both the original $3D$ jet test case on the left and is compared directly with the test case with the perturbation frequency decreased to $St = 0.08$ (referred to as the 'perturbation case') at $t = 16$. At this early stage of the jet development there are no discernible differences between the two flow fields. Due to this similarity between the flow fields, no further comparison was made between the flow fields until the flow fields were more fully developed at $t = 50$ and $t = 70$. The jet case at $t = 50$ jet case is presented in figure 6.17 – figure 6.21. In figure 6.17 the variations on the flow field become clearer. Two vortex rings are present in both the original and perturbation cases in the region $x = 10$ and $x = 15$. A notable difference in the first vortex structure at $x = 10$ was noted in this figure, with the perturbation case showing a greater asymmetry around the jet centreline. The second vortex structure at $x = 15$ was seen to differ even more considerably; the perturbation case showing a much greater vortex intensity in this region than the original case. Three streamwise slices were taken through each flow field at $z = 10$, $z = 15$ and $z = 20$, thus highlighting the structure of both the second and third vortex ring and the downstream region of the fluid domain. These figures are presented in figure 6.19 – figure 6.21. In figure 6.20 the full extent of the variation between the two flow fields is most visible. Both the location of the jet core and the structure of the vortex ring were noted to have been largely modified by the decrease in the perturbation frequency.

The velocity vectors at $t = 50$ were again analysed at the same locations at $t = 70$. These vector diagrams taken at $t = 70$ are presented in figure 6.22 – figure 6.26. From figure 6.22 and figure 6.23 it can be noted that the original case displays a much greater deal of flow asymmetry in the downstream region beyond $x = 12.5$. Although the perturbation case showed a larger degree of flow asymmetry in the region of the second vortex structure at $x = 10$ at $t = 50$. This high degree of asymmetry in the downstream region of the original jet case can also clearly be noted in the streamwise slices of the flow field displayed in figure 6.24 and figure 6.25. figure 6.26 shows the streamwise slice at x = 20, at this downstream location both the original and perturbation cases show a comparable level of flow asymmetry.

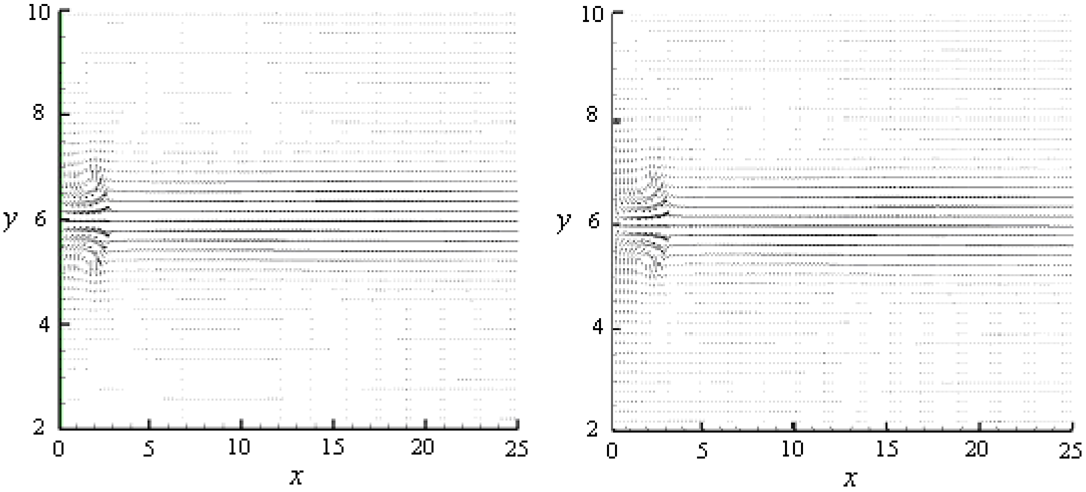

Fig. 6.16 Perturbation case comparison at t = 16. (original on the left, modified case on the right)

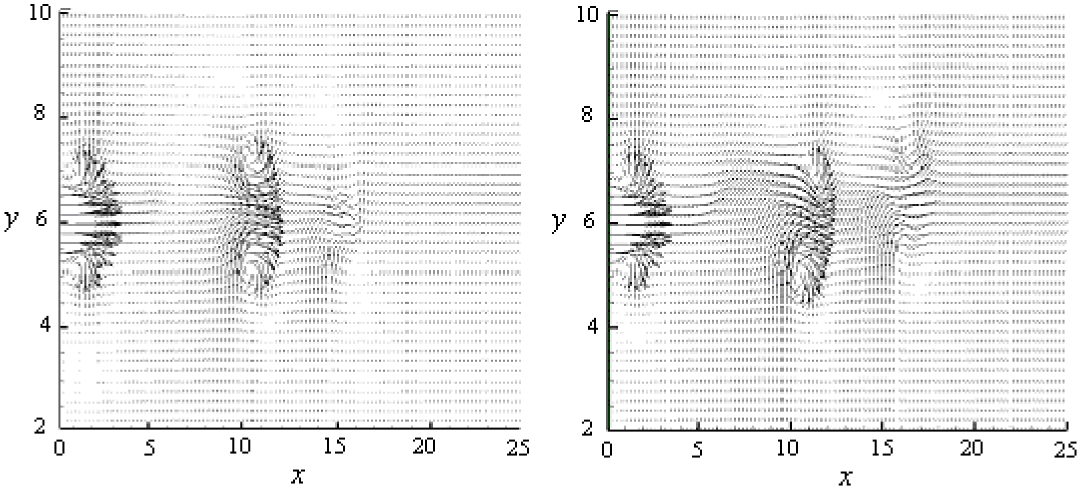

Fig. 6.17 Perturbation case comparison at t = 50 (original on the left, modified case on the right)

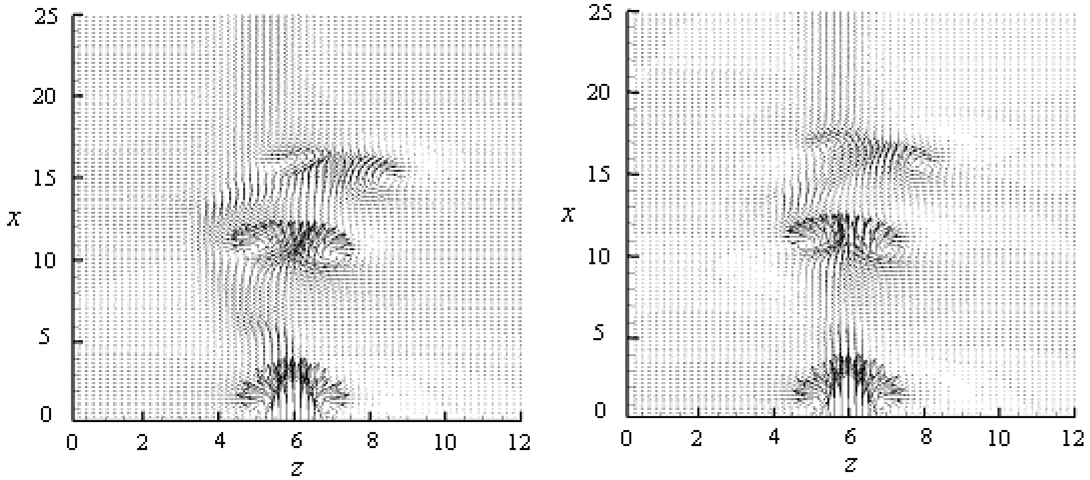

Fig. 6.18 Perturbation case comparison at $t = 50$ (original on the left, modified case on the right)

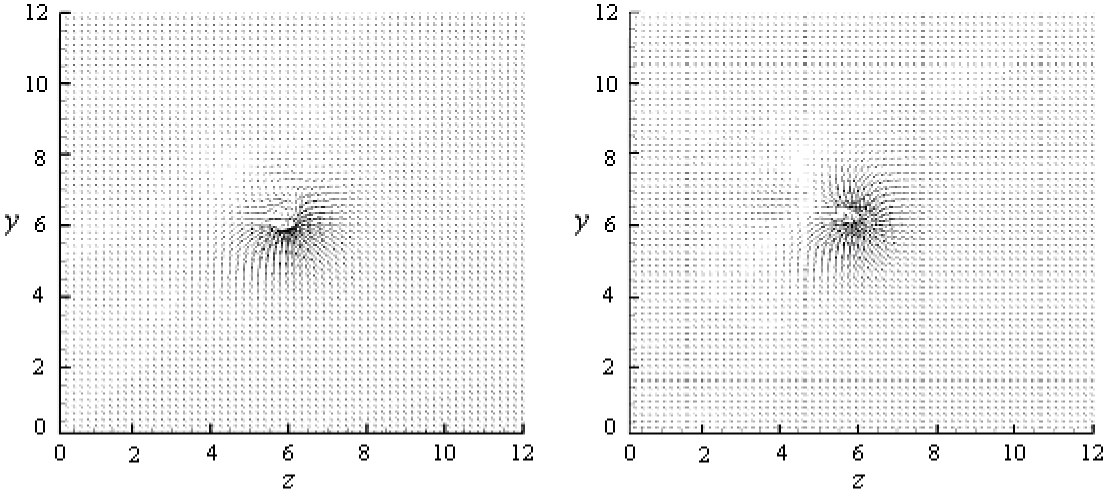

Fig. 6.19 $x = 10$ slice at $t = 50$ (original on the left, modified case on the right)

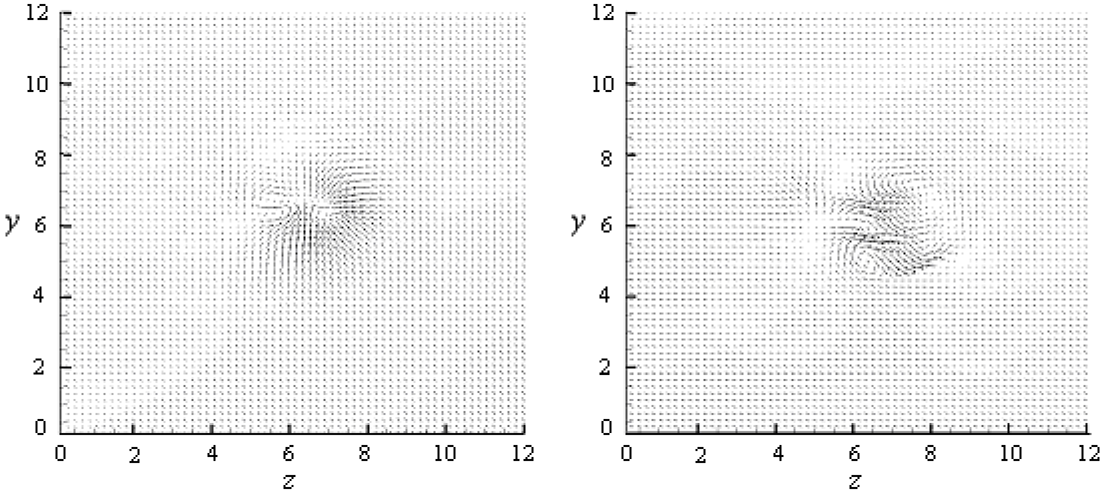

Fig. 6.20 *x* = 15 slice at *t* = 50 (original on the left, modified case on the right)

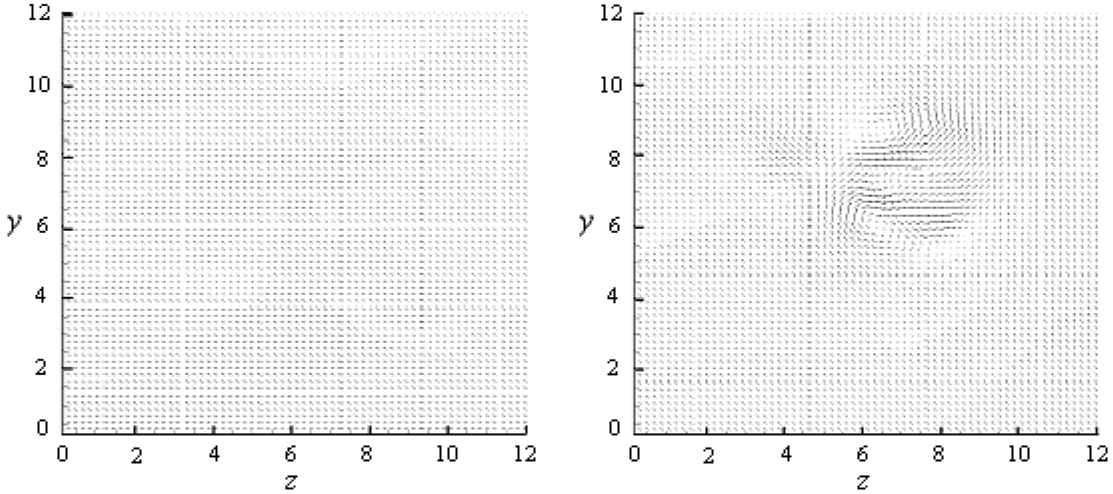

Fig. 6.21 *x* = 20 slice at *t* = 50 (original on the left, modified case on the right)

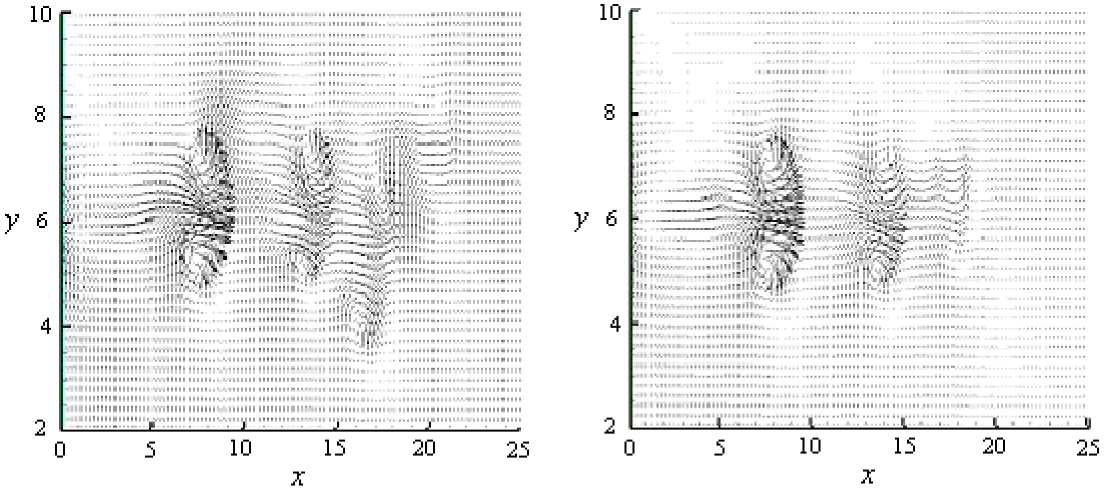

Fig. 6.22 Perturbation comparison at $t = 70$ (original on the left, modified case on the right)

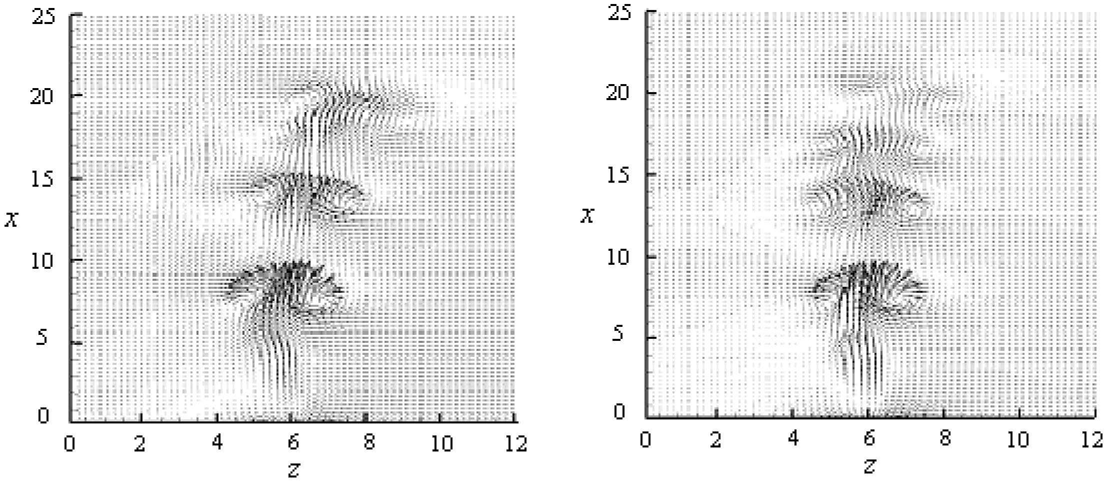

Fig. 6.23 Perturbation comparison at $t = 70$ (original on the left, modified case on the right)

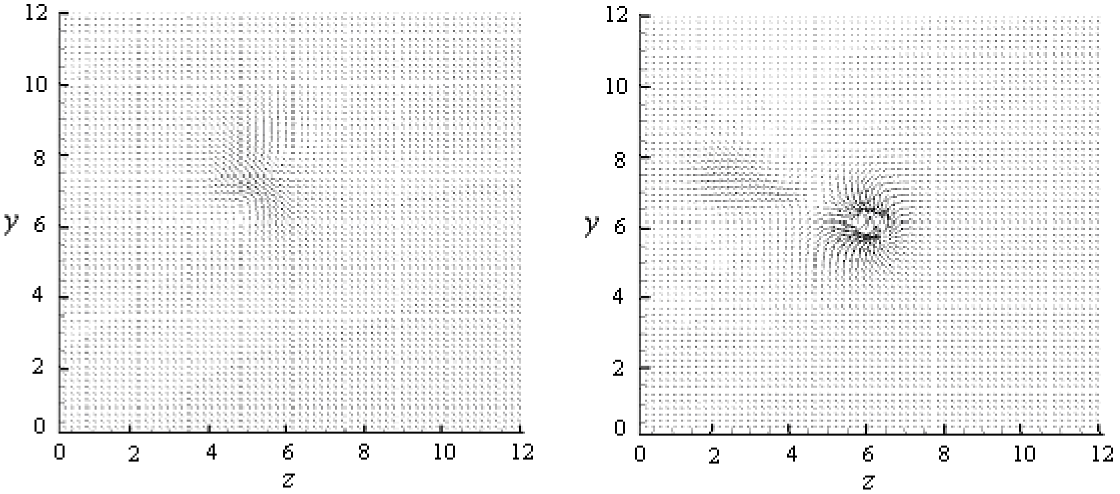

Fig. 6.24 $x = 10$ slice at $t = 70$ (original on the left, modified case on the right)

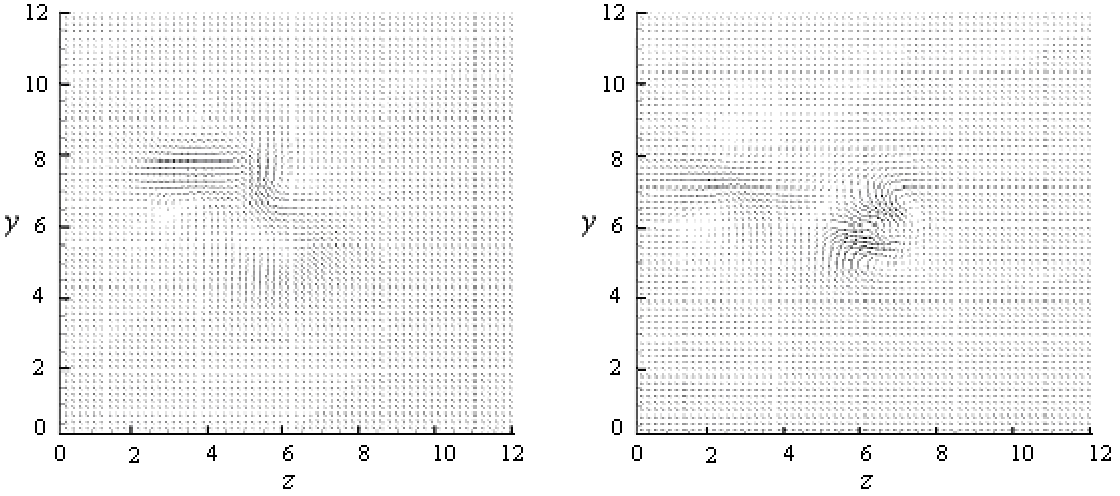

Fig. 6.25 $x = 15$ slice at $t = 70$ (original on the left, modified case on the right)

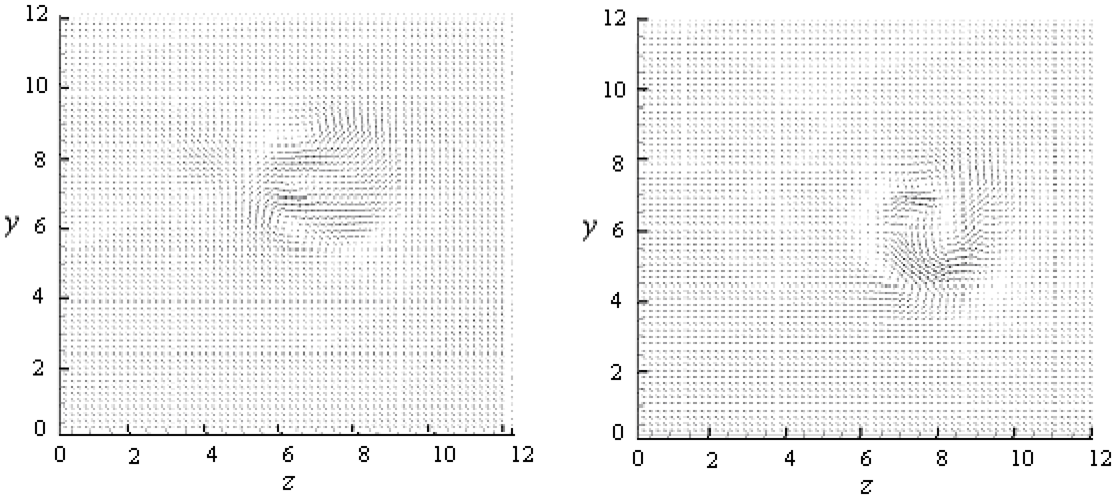

Fig. 6.26 $x = 20$ slice at $t = 70$ (original on the left, modified case on the right)

The modification of the frequency of the jet perturbation made a spatial impact on the vortex structures present in the flow field. The decrease in the jet perturbation frequency has, in most of the results analysed had the effect of reducing the level of asymmetry present in the flow, and also decreased the rate of lateral jet spreading. However, this has not been accompanied with a corresponding visible increase in jet centreline velocity and increase in the longevity of the jet. The results taken at $t = 50$ showed a marginal increase in the downstream extent of the jet perturbation case when compared to the original case. However the results taken at $t = 70$ show a very similar downstream extent for both jet cases, with the original case having slightly larger vortex structures present in the flow field region beyond $x = 20$.

The true effect of this perturbation frequency on the flow in the region $x = 5$ to $x = 10$, more importantly, the variation in flow features present in this region when compared to the axisymmetric case can be analysed from these results. The reduction in the intensity of the perturbation reduced the asymmetry of the flow, bringing it closer in line with the flow field predicted by the axisymmetric analysis, as would be expected. Although a full parametric analysis of this flow perturbation was impossible due to cost constraints, a better visualisation of its effect on the flow field has been achieved.

From this comparative study it can be deduced that; whereas previous numerical studies of synthetic jet actuator have concentrated on accurately modeling the complete jet orifice. A more accurate method of modeling the jet flow field may be achieved by breaking the flow symmetry associated with many numerical simulations. This may act to impose the type of flow asymmetry as noted in the experimental work by Smith & Glezer [2005], which was due to manufacturing tolerances in an otherwise symmetrical jet orifice.

6.7 Summary

In this chapter the boundary conditions and initial conditions for the fully three-dimensional version of the previously optimised axisymmetric jet case have been presented. The 3*D* vortex rings present in the flow field of the fully developed jet case have been analysed and the asymmetric nature of the flow structures noted. The isosurfaces of the fully evolved synthetic jet flow field as shown in figures 6.1(a) -6.1(i) give a good qualitative representation of the vortex structures present in the flow. Close comparisons can be made with the 3*D* DNS work on synthetic jets as carried out by Ravi & Mittal [2004]. A good agreement in terms of the flow structures present and the streamwise extent of the vortex train can be made between the synthetic jet flow field produced from a square actuator orifice, as examined by Ravi & Mittal and the current simulation case.

A further comparison can be made between the current simulation case and the $3D$ synthetic jet flow field results presented Rumsey *et. al.* [2007], in which the URANS results of a $3D$ synthetic jet actuator simulation carried out by NASA LaRC are presented. The NASA results presented by Rumsey *et. al.* have been non-dimensionalised in terms of orifice diameter and jet velocity to allow for comparison with the $3D$ DNS simulations. Although the input jet centreline velocity and Strouhal number did not match exactly between the DNS work in this thesis and the URANS simulations carried out by NASA LaRC as displayed in figure 6.27, a clearly identifiable time averaged velocity profile trend is identifiable with the two cases. It can be seen that both cases presented follow a similar profile of an initial rapid fluid acceleration in the region immediately downstream of the orifice to a peak in the region of $x = 3$. The DNS and NASA cases predict an initial reduction in centreline velocity downstream of this initial peak, followed by a second velocity peak in the region $10 < x < 30$. The more rapid reduction of velocity profile of the DNS case can be explained by the non-slip boundary condition applied at $x = 30$.

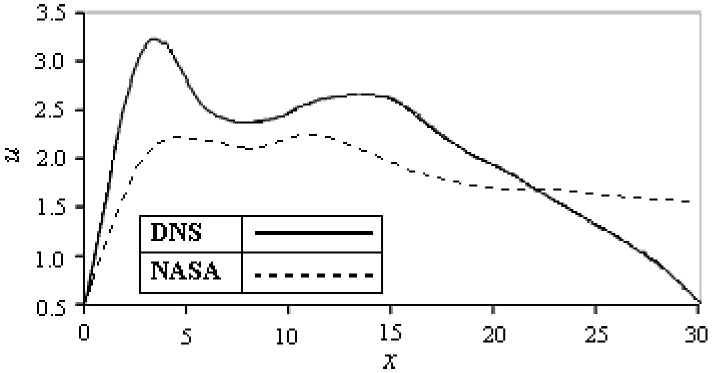

Fig. 6.27 DNS & NASA time averaged centreline velocity from $t = 50$ to $t = 165$

The structure of the interior of the jet core has been analysed by taking a number of lateral slices through the jet flow field. The results attained gave an insight into the *3D* nature of the flow field and the interaction of each vortex structure with the quiescent background fluid.

An evolution study of the three dimensional jet flow has been carried out and the flow development analysed with both velocity contour plots and vector diagrams. This study was further enhanced by an analysis of the centreline velocity of the synthetic jet actuator over a full actuation cycle.

Finally a study of the effect of the perturbation present in the three-dimensional jet actuator was carried out. The purpose of this perturbation is to break up the inherent two dimensional nature of the jet flow imposed by the symmetric actuator velocity profile. The effect on the flow field of reducing the frequency and therefore overall effect of the perturbation was analysed by comparison of the velocity vectors present at a number of locations throughout the flow field for both the original optimised case and a further case in which the perturbation frequency has been decreased by a factor of four.

A comprehensive account of the development of the three-dimensional flow field and flow features present within it have been given. Through this a good understanding of the three-dimensional nature of the flow field has been gained. The data attained in this study along with the data attained in the axisymmetric analysis in Chapter 5 forms the basis of an accurate and direct comparison between an axisymmetric and three-dimensional flow field using matching input parameters. This comparison will be presented in Chapter 7.

CHAPTER 7

AXISYMMETRIC & 3D COMPARISON

7.1 INTRODUCTION

The axisymmetric case gives a good qualitative view of the development of the vortex structures present in the flow. However due to the 3*D* nature of the flow, it is useful to compare the 3*D* vortex topology to that of the axisymmetric case. A direct comparison allows the level of accuracy of the axisymmetric flow field to be determined. Therefore the possible use of axisymmetric simulations for further studies of synthetic jet actuators can be assessed.

The same DNS scheme was used in the computation of both the three-dimensional and axisymmetric cases; however the two-dimensional nature of the axisymmetric case leads to a notable difference in the features present in the flow field. As was noted in Chapter 5, the lack of any cross-streamwise flow features leads to a regular oscillating centreline velocity profile, which gradually decreases in magnitude as the distance from the orifice increases. The same trend is present in the three-dimensional case; however the cross-streamwise flow present due to the influence of the velocity perturbation applied at the orifice results in a less uniform centreline velocity distribution, as can be seen in the 3*D* velocity plots of the flow field presented in Chapter 6.

7.2 JET CENTRELINE VELOCITY

The centreline velocity profile presented in figure 7.1 clearly shows the difference present in the flow field between the axisymmetric and 3*D* cases. The axisymmetric and 3*D* velocity profiles in the region adjacent to the orifice ($x < 5$) produce very similar results. The first velocity peak occurred at the same location in both cases and the same velocity magnitude was predicted. However the velocity profiles in the region $5 < x < 12$ showed a large variation in velocity magnitude. As described in Chapter 6, the axisymmetric case predicted a vortex ring, and its associated velocity peak in this region. However the 3*D* results showed an absence of this vortex ring in this region. This feature is highlighted in figure 7.1 where the stark difference between the axisymmetric and 3*D* centreline velocity profiles is clearly visible. Interestingly the velocity profiles of both the axisymmetric and 3*D* cases can be noted to be in broad agreement in the region downstream of $x = 12$.

Investigations into the effect of the jet perturbation imposed on the actuator flow of the 3*D* case (Chapter 6.7) highlighted the influence of this parameter on the 3*D* flow field in this region.

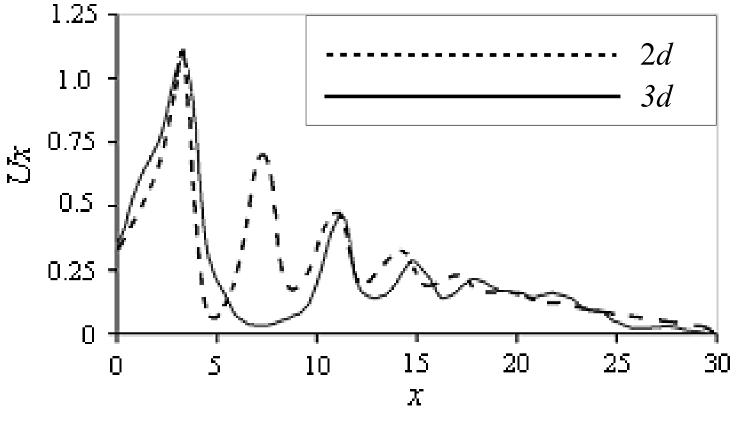

Fig. 7.1 Jet centreline velocity at $t = 165$ of the three-dimensional case.

7.3 FLOW FIELD EVOLUTION OVER A SINGLE ACTUATOR CYCLE

A comparative evolution study of both the axisymmetric and 3*D* jets was carried out in order to accurately visualise the formation and movement downstream of a single vortex ring. A direct comparison between the axisymmetric and 3*D* analysis was made over the same complete actuation cycle as was investigated in Chapter 6.3. Both cases used identical input parameters wherever possible, so any variations in the flow field will purely be due to the differences between the 3*D* and axisymmetric regimes and the perturbation added to the 3*D* simulation.

In this case the study was carried out for a developed jet flow between the time instances of t = 62.5 and t = 75. Therefore, five complete actuation cycles have taken place before the start of the observations; which run for the entire course of the 6th actuation cycle. The time period of the complete actuation cycle is broken down into eight evenly spaced time instances. Therefore the actuation cycle could be monitored at every 100%, 50% and zero deflection point of the actuator input wave. The most relevant five of the eight analysed time instances are displayed in figure 7.2. Starting with the actuator at its 100% outflow point in figure 7.2(a), completing a full actuation cycle before returning to the 100% outflow point in figure 7.2(i).

A series of vector plots, showing the velocity vectors present at the z = 6 jet centreline for the 3*D* case, and a centreline slice for the axisymmetric case are shown in figure 7.2. The 3*D* case is displayed on the left hand plot, while the corresponding axisymmetric case can be seen to the right. It can be noted that although the flow structure is comparable close to the jet orifice, the downstream flow features vary greatly between the 3*D* and axisymmetric cases. The uniform series of vortex structures present in the axisymmetric case is not present in the 3*D* flow field. With the exception of the region between *x* = 5 and *x* = 10 the vortex structures are comparable position along the *x* axis. However the structures present in the 3*D* case are of a greater velocity magnitude.

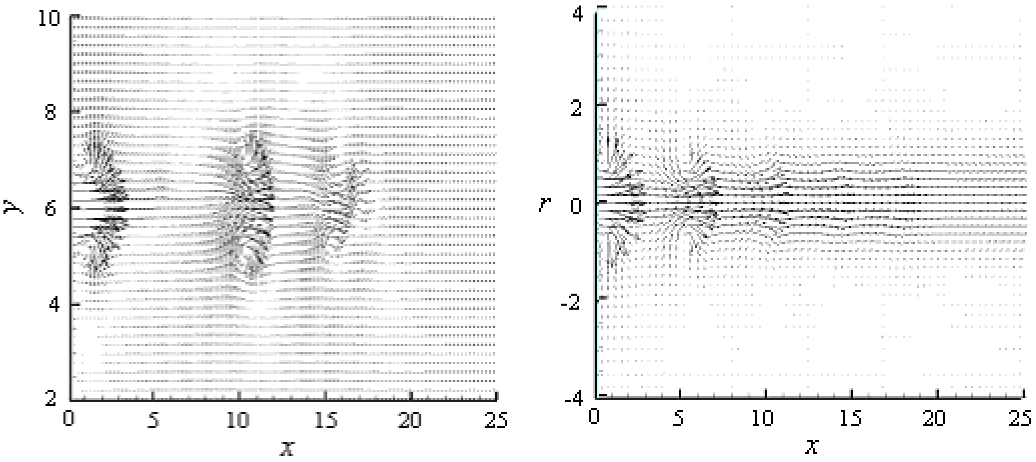

Fig. 7.2(a) Velocity vectors at *t* = 62.5

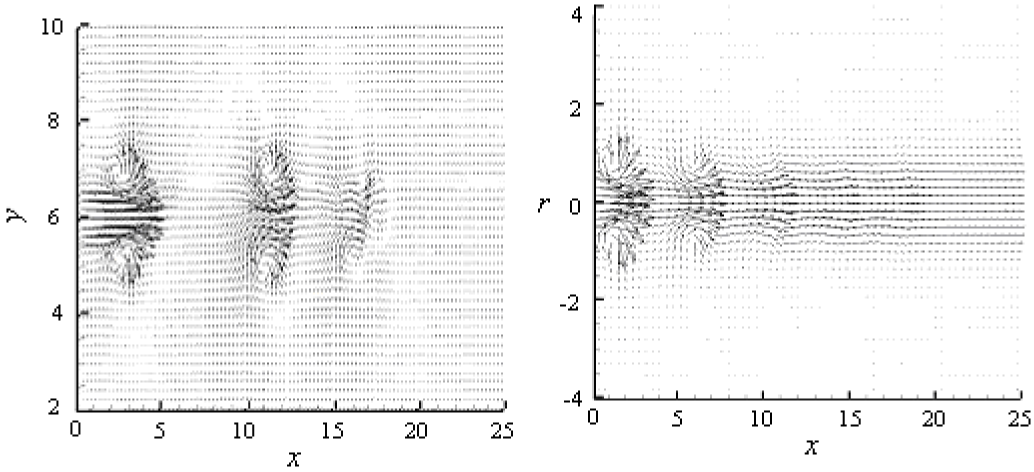

Fig. 7.2(b) Velocity vectors at *t* = 64.0625

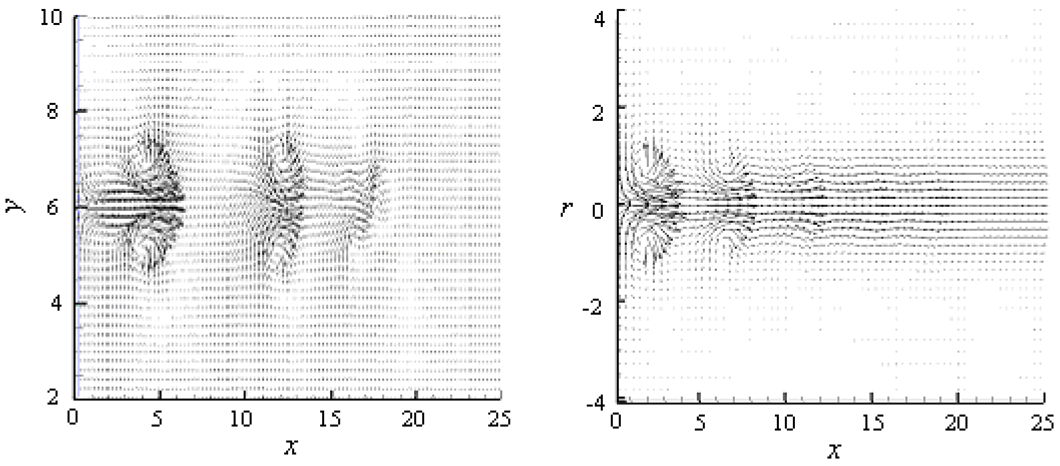

Fig. 7.2(c) Velocity vectors at *t* = 65.625

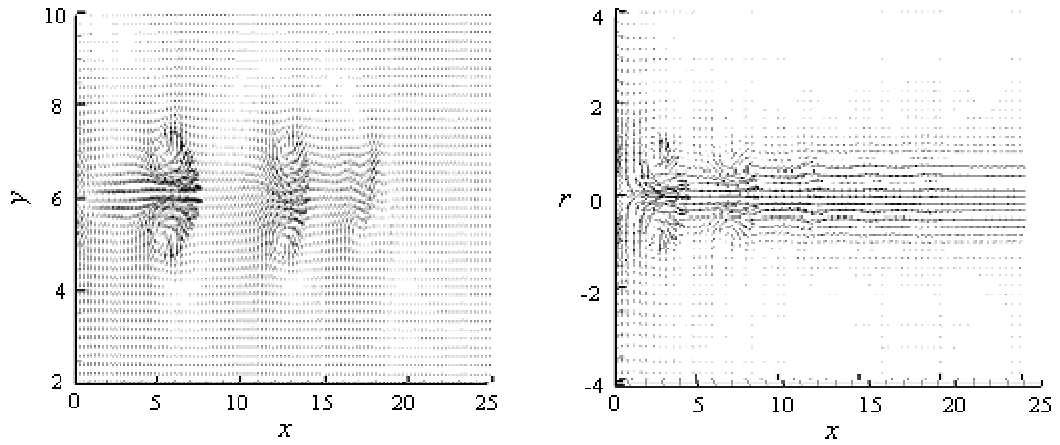

Fig. 7.2(d) Velocity vectors at *t* = 67.1875

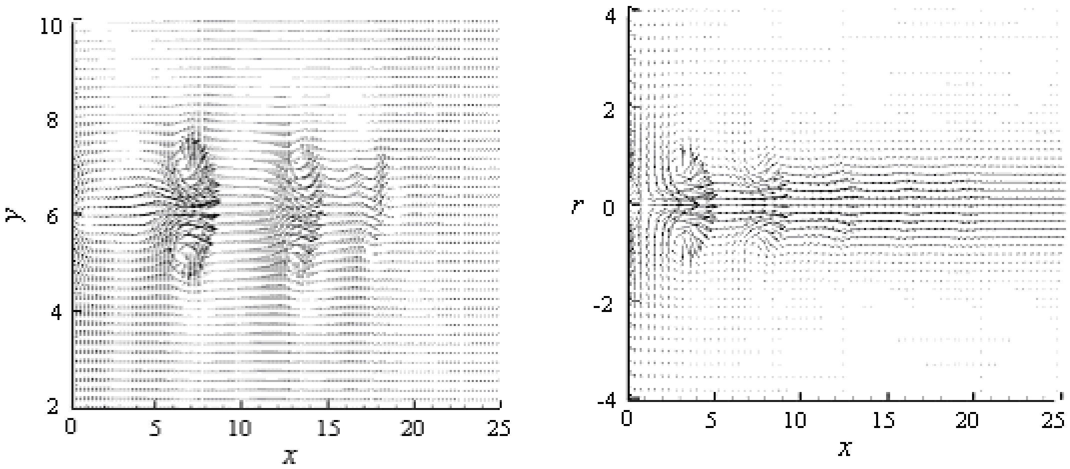

Fig. 7.2(e) Velocity vectors at *t* = 68.75

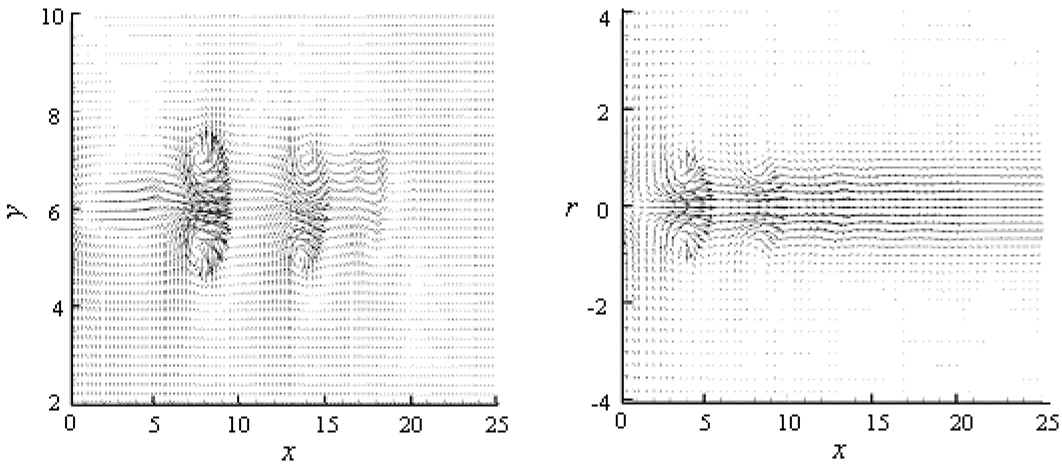

Fig. 7.2(f) Velocity vectors at *t* = 70.3125

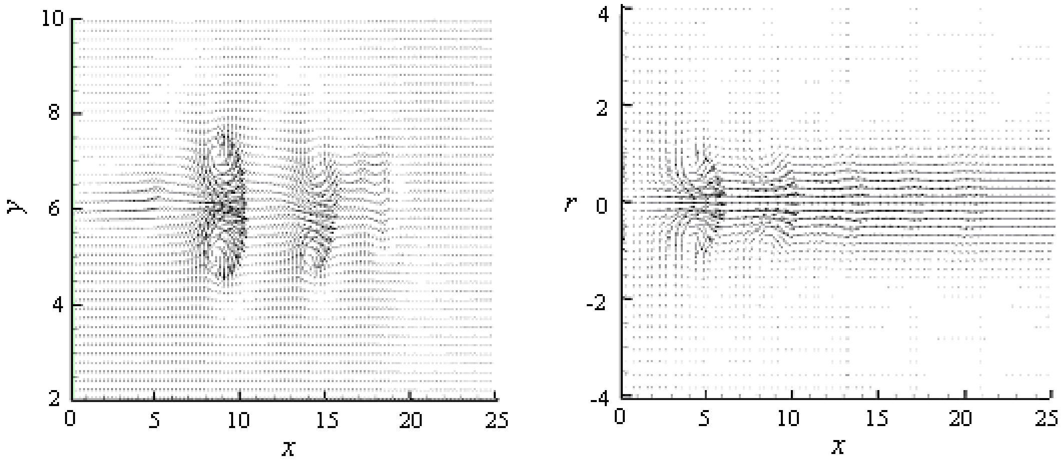

Fig. 7.2(g) Velocity vectors at *t* = 71.875

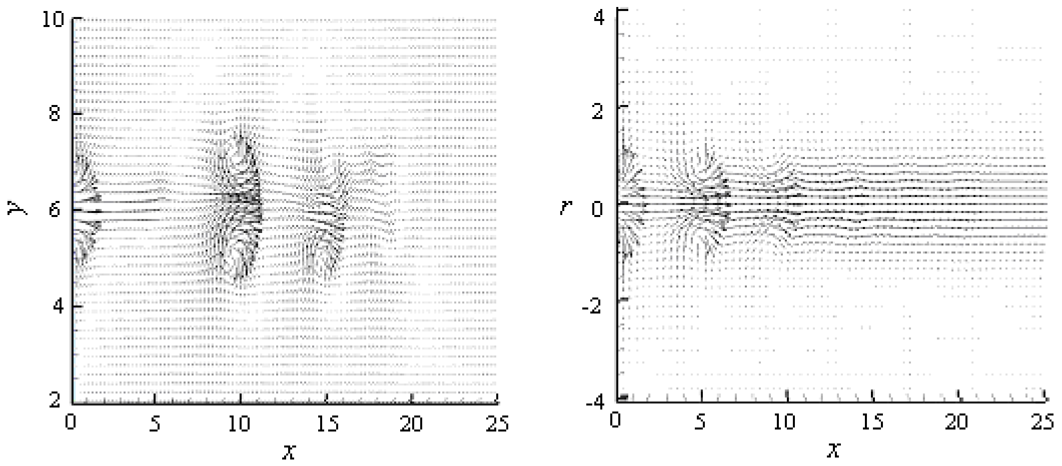

Fig. 7.2(h) Velocity vectors at *t* =73.4375

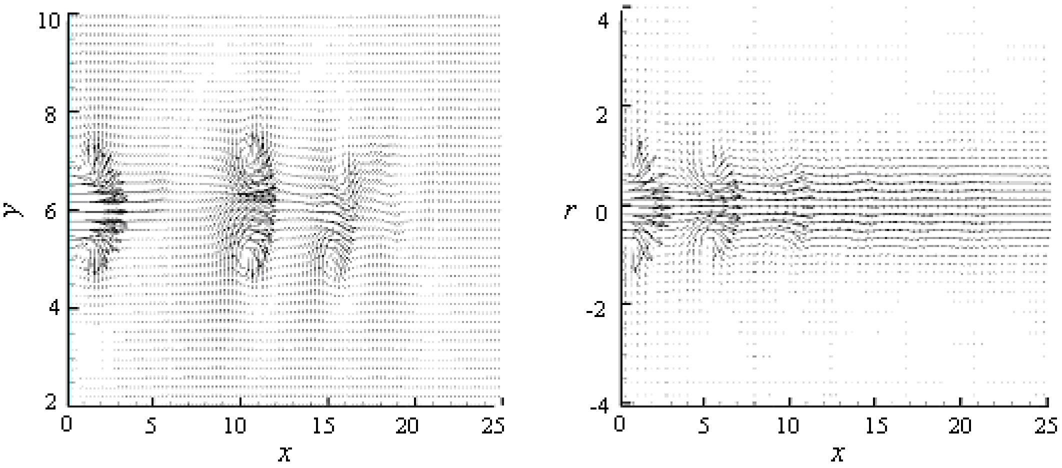

Fig. 7.2(i) Velocity vectors at *t* = 75

Fig.7.2 Velocity vectors over one actuation cycle for the 3*D* and axisymmetric cases

7.4 INITIAL JET FORMATION

Following on from the evolution study of the axisymmetric and 3*D* synthetic jets over a single actuator cycle, a comparison between the initial jet formation of the two cases was carried out. For this analysis the simulation was stopped at regular time intervals over the development of the synthetic jet flow. The vector distributions and flow structure at the particular time instants were analysed with the aim of making a like-for-like comparison.

As can be seen in figure 7.3(a) even in the early stages of the formation of the vortex train, there are notable differences between the two flow fields. A large vortex ring was predicted by the 3*D* analysis in the region x = 7. In the axisymmetric case at the same time instant a pair of vortex rings is predicted at x = 4 & x = 8.

As can be seen in figure 7.3(b) – figure 7.3(d), the formation of a vortex train in both cases is clear after $t = 30$. The intensity of the vortex cores decreases as the fluid slug moves downstream, however each vortex structure present in the flow field can be seen to spread out into the far-field as it moves downstream. It is clear that the size and rate of spreading of each vortex structure differed between the 3*D* and axisymmetric cases. In the case of the 3*D* analysis each vortex structure spreads laterally to the edges of the computational domain. With the axisymmetric case each vortex structure was of a smaller scale with the velocity intensity reducing rapidly away from the jet centreline. This resulted in a much lower extent of vortex spreading in comparison with the 3*D* case, especially in the downstream region.

With the exception of the $4 < x < 10$ region the streamwise location of each vortex ring was comparable between the two cases. The centre of each vortex ring remains constant along the $r = 0$ centreline for the axisymmetric case, whereas the centre of each vortex ring varies laterally along the y axis for the 3*D* case.

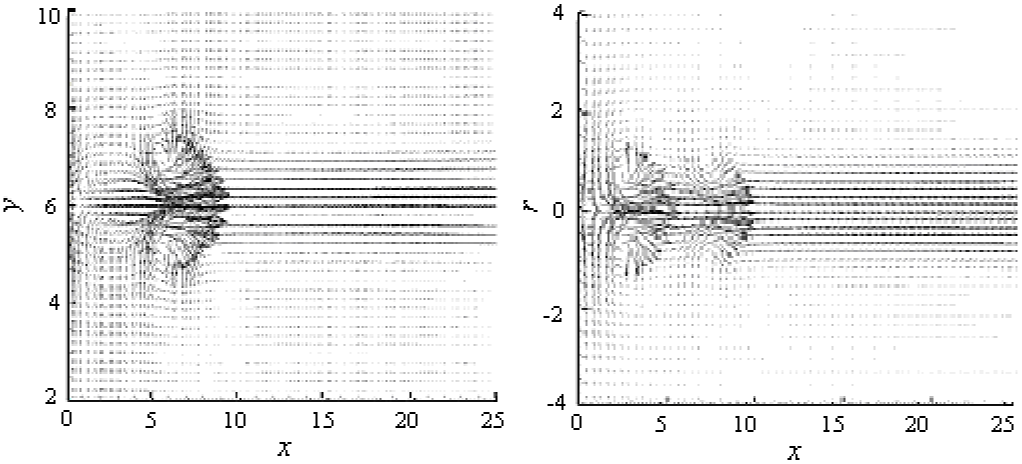

Fig. 7.3(a) Velocity vectors at $t = 30$

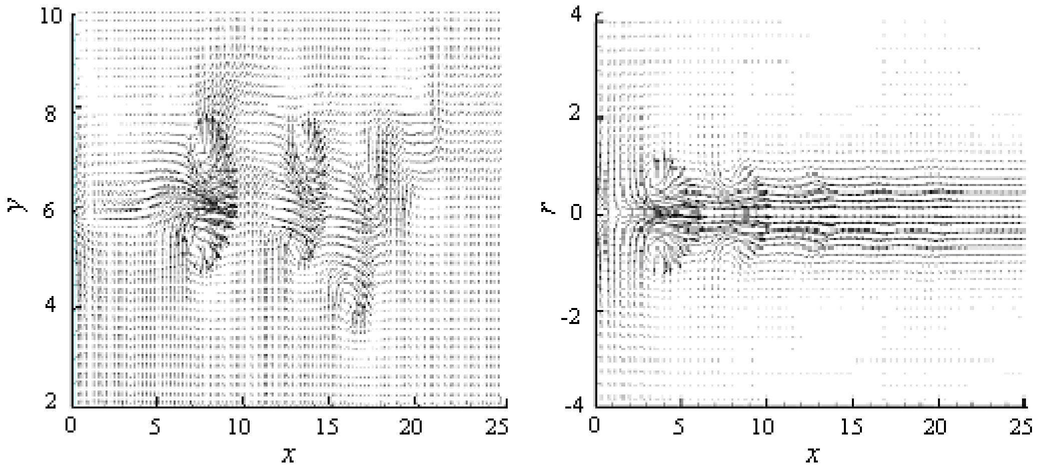

Fig. 7.3(b) Velocity vectors at *t* = 70

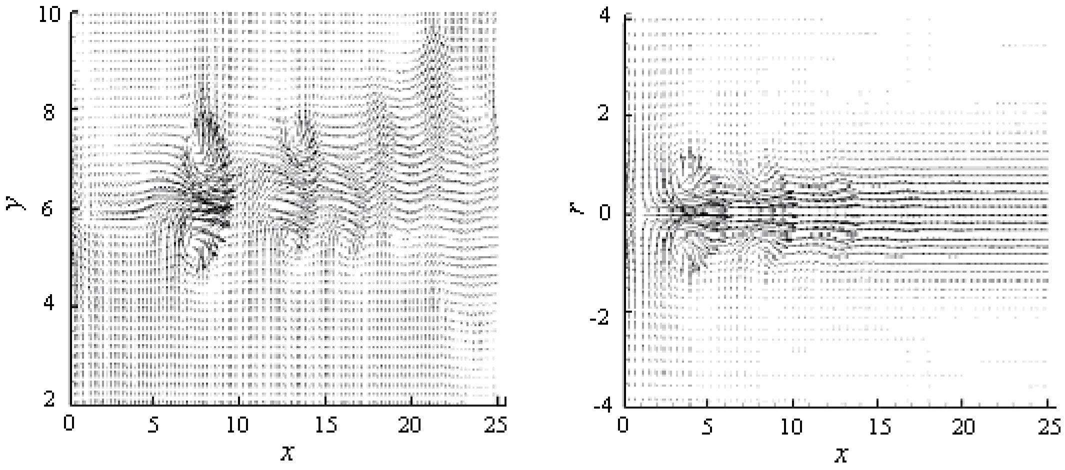

Fig. 7.3(c) Velocity vectors at *t* = 120

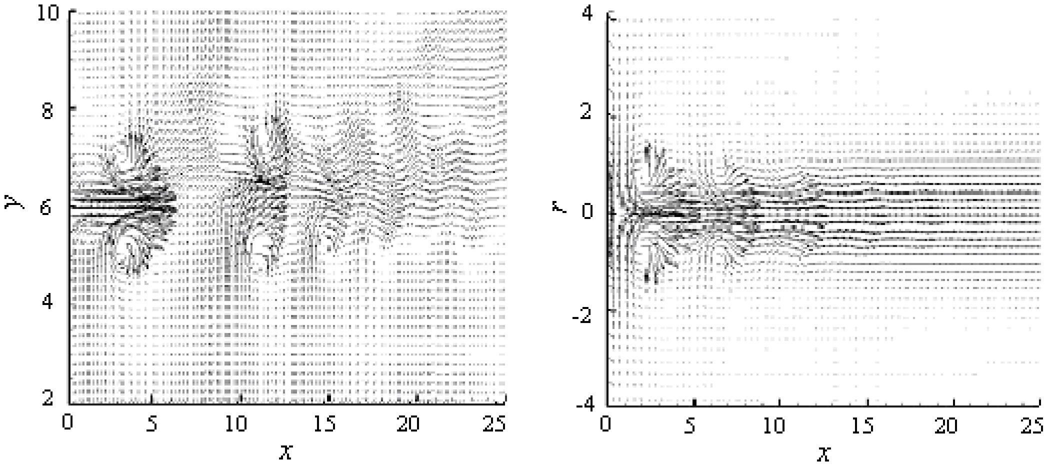

Fig. 7.3(d) Velocity vectors at *t* = 165

Fig.7.3 Time evolution of the vortex structures present in the three-dimensional case (left) and axisymmetric case (right).

A further comparison between the axisymmetric and 3*D* jet simulations is made in figure 7.4. In this diagram the centreline velocity history at $x = 15$ is plotted for both the axisymmetric and 3*D* cases, and also compared to the initial velocity applied at the jet orifice ($x = 0$). The variations between the axisymmetric and 3*D* cases are again clear. The frequency of the vortex train of the axisymmetric and 3*D* cases goes out of phase with each other as time progresses. This is despite the same input actuation frequency being applied to both cases. The oscillations of the streamwise velocity magnitude of the 3*D* case are higher than that of the axisymmetric case throughout the monitored period. This highlights the effects of the 3*D* features in the flow field which act to sustain the vortex train.

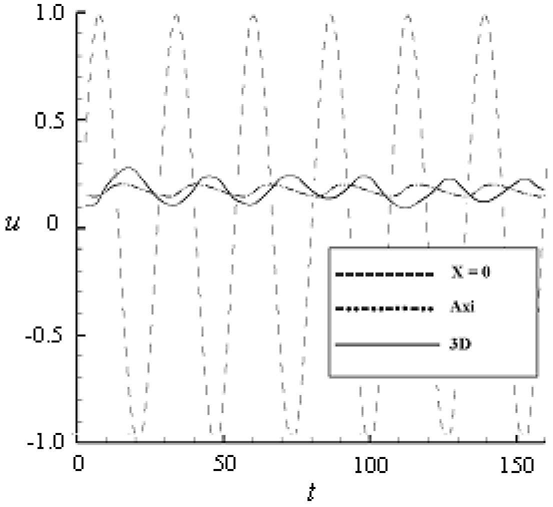

Fig. 7.4 Centreline velocity history of the axisymmetric and 3*D* cases.

7.5 SUMMARY

In this chapter the flow features present for both the axisymmetric and 3*D* cases over a single actuator cycle of a fully evolved synthetic jet flow field were compared. This study was further reinforced with a comparative evolution study between the two cases. For both cases the variations in location and intensity of the vortex structures present in the flow field were analysed.

The rate of vortex spreading for the 3*D* case was found to be much greater than that of the axisymmetric case. The vortex intensity was noted to decrease rapidly away from the jet centreline for the axisymmetric case. This reduction in vortex spreading for the axisymmetric case when compared to the 3*D* can also be noted in previous synthetic jet simulation work described by Rumsey *et. al.* [2007]. For the simulations analysed by

Rumsely *et. al.* [2004] a 3*D* laminar simulation of a synthetic jet was also noted to have a much greater streamwise longevity in terms of streamwise velocity and vorticity components when compared to a 2*D* laminar simulation using the same jet input parameters. However, in the case analysed by Rumsey *et. al.* the peak streamwise velocity was noted to be be higher for the 3*D* case. As shown in figure 7.1, the 2*D* and 3*D* cases analysed in the current simulations display close agreement in terms of the peak streamwise velocity present.

The periodic behavior of both cases was demonstrated at a downstream location. Both cases displayed a clear oscillating velocity fluctuation with respect to time. As was expected the oscillating profile of the axisymmetric case displayed a much greater deal of uniformity than that of the 3*D* case.

CHAPTER 8

PLANAR SYNTHETIC JET SIMULATIONS

8.1 INTRODUCTION

In this chapter a DNS analysis is carried out on a planar 2*d* synthetic jet actuator, using a Strouhal number of $St = 0.08$. Due to computational limitations the Reynolds number used in these cross-flow tests was limited to a maximum value of $Re = 185$. Thus the jet flow field cannot be directly compared to the optimised results of the axisymmetric and 3*D* analysis carried out previously. The evolution of a synthetic jet in the presence of a boundary layer type velocity profile has been examined for a range of input velocities. A number of cross-flow velocities were examined, ranging from the minimum value of 10% of the maximum jet centreline velocity at the orifice, up to a maximum value of 25% of the centreline velocity. These velocities were chosen so as to visually compare the results to the vorticity field presented in Glezer & Amitay's [2002] paper on Synthetic jets.

8.2 PLANAR CASE IN QUIESCENT AIR

In order to allow a comparison to be made of the cross-flow velocity effects on the synthetic jet flow field, the planar jet code was first modelled in a quiescent medium at a Reynolds number of *Re* = 185. The planar flow field is shown in figure 8.1, in this case the flow solution is presented at t = 80. In this case the jet symmetry around the jet centre-line can be noted. The streamwise extent of the vortex structure produced by the actuator can be noted to be in the region of x = 5 at this *Re* value.

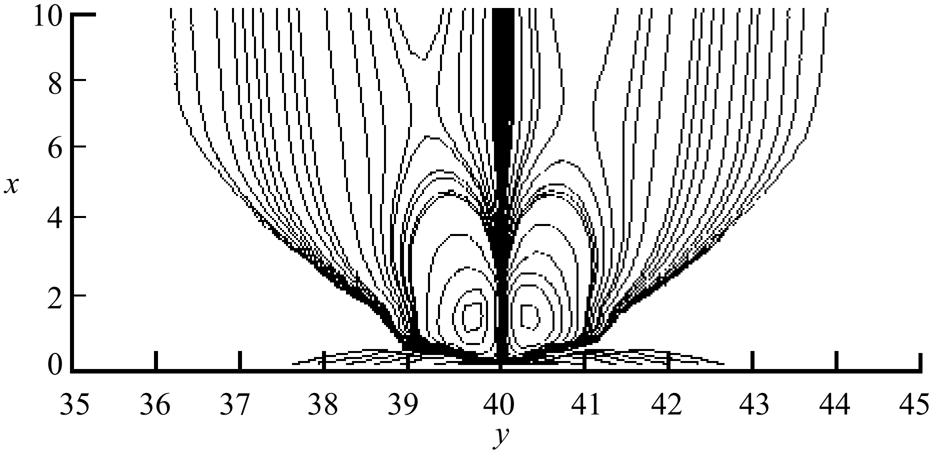

Fig. 8.1 Vorticity contours of the planar case at t = 60.

8.3 PLANAR CASE IN A CROSS-FLOW

Several computational cases have been analysed in order to investigate the flow features of a synthetic jet flow field in a cross-flow. The specification of the velocity profile used in applying the cross-flow velocity is presented in Chapter 3.6.1. A parametric study performed to investigate the effects of varying the cross-flow velocity. In this study 'v' is specified as a function of the maximum streamwise jet velocity: 'u'. Three values of v were examined; $v = 0.1u$, $v = 0.15u$, and $v = 0.25u$. The vorticity distribution at a number of time instances is displayed in figure 8.2 – figure 8.4. These figures capture the effect of the cross-streamwise velocity profile on vortex rings adjacent to the jet actuator.

Figure 8.2 represents the vortex development of the synthetic jet flow field with a v velocity component of $0.1u$ at $t = 60$. In this case the pair of vortices expelled from the orifice can be seen to be distorted and tilted in the direction of the cross-flow. As noted by Glezer & Amitay [2002], the vortex pair are uneven in terms of vortex strength. This has been determined to be due to the ingestion of opposite-sense vorticity by the weaker of the vortex pair.

Figure 8.3 represents the same actuator conditions and the same time instances as displayed in figure 8.2. In this case, however the v velocity component has been increased to $0.15u$. In this case the increased distortion of the vortex pair can be noted in the presence of the cross-stream velocity profile. Further increasing the v velocity component to $v = 0.25u$, as shown in figure 8.4 resulted in a further increase in the distortion of the vortex structures and a tilting of the synthetic jet flow field. In figure 8.4 the first vortex pair can be seen to be developing in the region adjacent to the orifice. In this case the effect of the v velocity component is already clear in this early stage of the vortex development. The effect of the *v* velocity field is to distort and rotate the vortex pair through almost ninety degrees. The stronger of the vortex pair is now be noted to have moved to a location close to the wall.

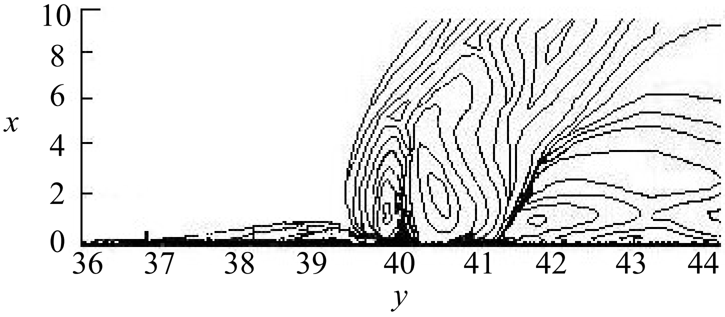

Fig. 8.2 Vorticity contours with a cross-flow velocity of $v = 0.1u$.

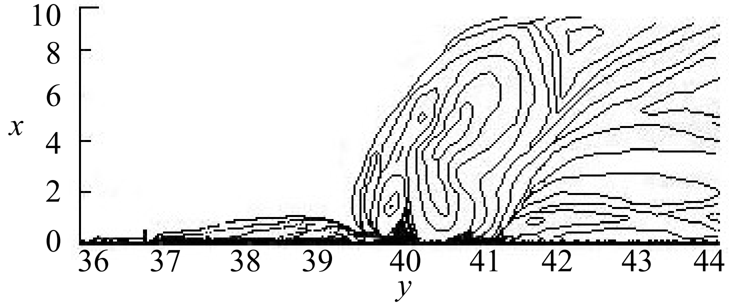

Fig. 8.3 Vorticity contours with a cross-flow velocity of $v = 0.15u$.

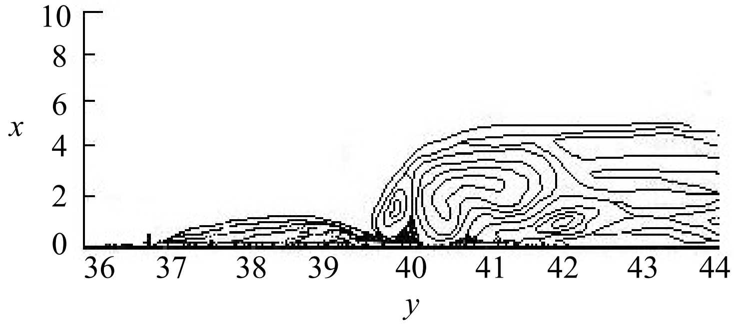

Fig. 8.4 Vorticity contours with a cross-flow velocity of $v = 0.25u$.

8.3.1 CROSS-FLOW VELOCITY PROFILE

In order to deduce the possible application of synthetic jets in stabilising the inflexional velocity profile associated with the low-speed streaks, the v component of velocity has been plotted for nine y locations. These locations range from $y = 36$ to $y = 44$ and are plotted together for each value of v in figure 8.5 – figure 8.7. In these figures the v velocity profile is displayed in the region between the wall at $x = 0$ and $x = 16$, the point at which the effect of the synthetic jet actuator inflow has negligible effect on the cross-streamwise flow. The type of inflexional velocity profile is associated with the lift-off of a low-speed streak is also displayed to the right of each figure (displayed with a dashed line) for purposes of comparison.

In figure 8.5 – figure 8.7 the effect of the synthetic jet actuator flow field on the cross-flow velocity profile can be noted in the region $40 < y < 44$. The velocity profile becomes thinner in the region below $x = 8$. In figure 8.7 the cross-streamwise velocity profile has started to recover and become thicker in the near wall region by $y = 44$. This recovery of the cross-streamwise velocity profile could not be noted in figure 8.5 & figure 8.6. This was deemed to be due to the lower cross-flow velocity profile used in these cases. Therefore the synthetic jet actuator flow field causes a comparatively larger disturbance to the *v* velocity profile in these cases with a lower cross-flow velocity.

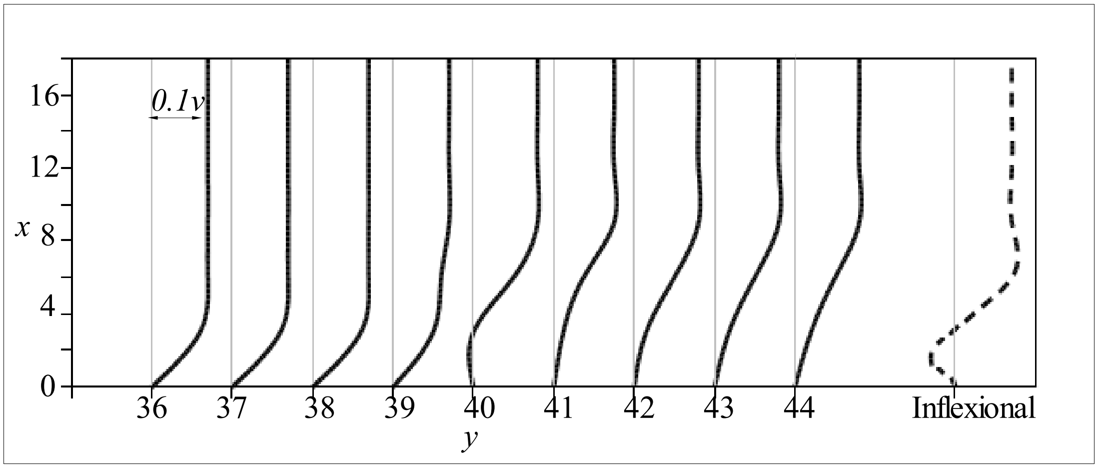

Fig. 8.5 Cross-stream velocity profile for $v = 0.1u$

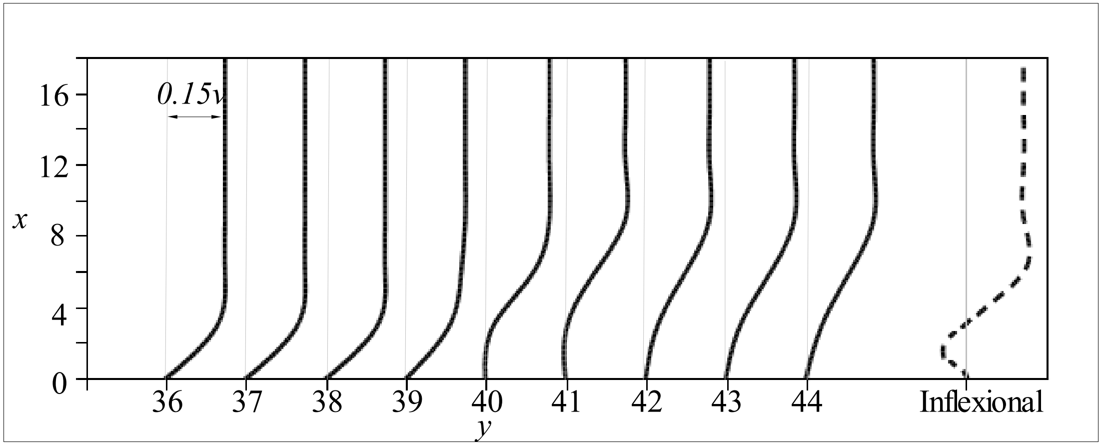

Fig. 8.6 Cross-stream velocity profile for $v = 0.15u$

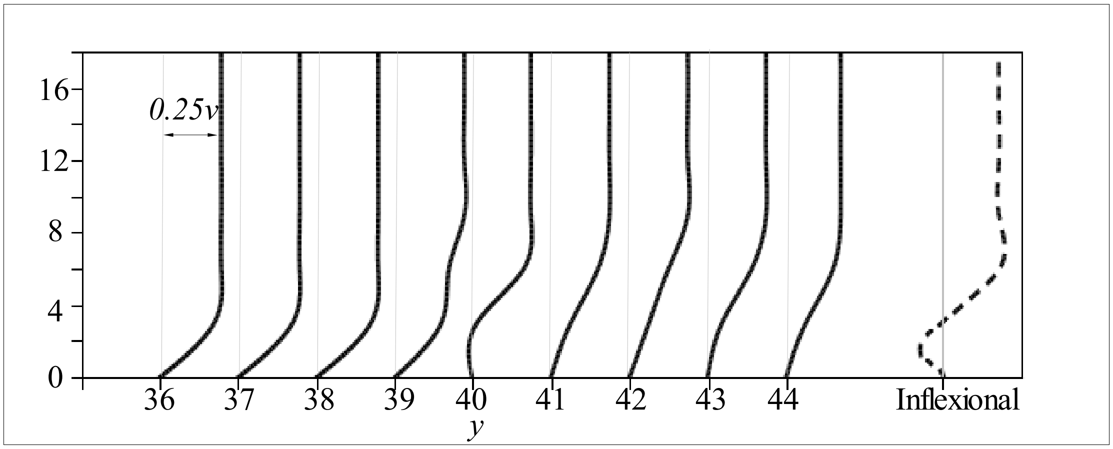

Fig. 8.7 Cross-stream velocity profile for $v = 0.25u$

8.4 STROUHAL NUMBER VARIATION OF A PLANAR SYNTHETIC JET IN A CROSS-FLOW

The compressible, 2*D* Navier-Stokes equations, as presented in Chapter 3, have been solved in order to compute the effect of Strouhal number on synthetic jet evolution in a cross-flow. Three computational cases have been performed, utilising the optimum value of $St = 0.08$, along with two of the other Strouhal numbers that were also investigated in chapter 5.2.1. The details of each cross-flow simulation undertaken are outlined in Table 8.1. As has been demonstrated in section 5.2.1 the synthetic jet displays significantly different vortex structures at a range of Strouhal numbers in a quiescent fluid domain. The aim of this study is to investigate the applicability of this optimal Strouhal number for the evolution a synthetic jet in a cross-flow.

Case	A	B	C
Strouhal number	0.04	0.08	0.16
Reynolds number	300	300	300
CFL number	10	10	10

Table 8.1. The computational cases of the 2*D* cross-flow simulations

Figures 8.8 - 8.10 show contours of vorticity present in the synthetic jet flow field for the three conditions analysed. The effect of an increase in Strouhal number on the flow characteristics at $t = 60$ can be noted in terms of the vorticity magnitude of the structures present in the flow field. However, the Strouhal number effect on the flow field is far less pronounced than for the simulations in a quiescent background fluid. The streamwise extent of the jet in all three cases remains almost constant, with the maximum extent being in the region of $x = 7.5$ for all three cases. The distance between vortex cores can be noted to reduce with an increase of Strouhal number, but to a lesser extent than the quiescent test cases, due to the influence of the cross-flow velocity.

It is clear from the three cases analysed in the presence of a cross-flow that the effect of the Strouhal number is largely overcome by the effect of the cross streamwise velocity component. The addition of a cross-flow velocity dramatically alters the manner in which the suction stroke effects the fluid slug closest to the orifice. In the case of a quiescent background fluid the formation of a synthetic jet vortex train relies on the momentum of each vortex pair having a strong enough streamwise component to overcome the subsequent suction stroke of the orifice. A cross-flow velocity component acts to carry the vortex pair away from the orifice in the primary direction of the cross-flow, thus diminishing the effect of the suction stroke of the orifice on the vortex pair. The result of this is that, at higher Strouhal numbers the high frequency actuation at the orifice does not cause the re-ingestion of the most recently expelled vortex pair. This re-ingestion is evident in a quiescent background fluid. However, as noted in section 8.2, the effect of a cross-flow can also diminish, or indeed completely dissipate the vortex pairs produced by a synthetic jet actuator in cases of a high cross-flow velocity magnitude.

In Figure 8.8 vortices can be seen as they are expelled by the orifice. They can be noted to travel away from the orifice in the streamwise direction, before being stretched and distorted by the cross-flow velocity component. A number of vortices can also be noted in the region between $40 < y < 47$. The trajectories of the vortex pairs can be noted to split in the region of $x = 2$. One side of the vortex train advects further into the cross-flow in the x direction than the other. The second side of the vortex train remains closer to the wall and begins to move towards the wall as it moves downstream in the cross-flow direction. Experimental work carried out on synthetic jets by Zhong *et. al.* [2005] noted that in some cases this second trajectory of vortices evolve to form hairpin vortices in the region close to the wall.

A secondary trajectory of vortices present in the synthetic jet flow field has been noted by Tomar *et. al.* [2004] at Strouhal numbers above $St = 0.19$. Tomar *et. al* referred to this feature as a 'multiple trajectory' structure. It was noted by that the secondary trajectory emerges from the primary trajectory at an acute angle and does not extend as far in the streamwise direction. This behaviour matches closely with behaviour of the vortex cores in the three cases analysed in this section. The vorticity profiles of all three cases analysed suggest that the secondary trajectory structure noted by Tomar *et. al.* is formed by the splitting of the vortex pairs as they move away from the orifice. The vorticity contours present in figure 8.8 clearly show the presence of the secondary trajectory of vortices present at *St* = 0.04 suggesting that the secondary trajectory structures are also present at lower values of Strouhal number than previously suggested. It can also be noted in all three cases analysed that the initial angle between the primary and secondary trajectories remains almost constant as the Strouhal number increases. In figures 8.8 – 8.10 the locus of the primary vortex cores is indicated in red, and the locus of the secondary vortex cores is indicated in green in order to ease visualisation.

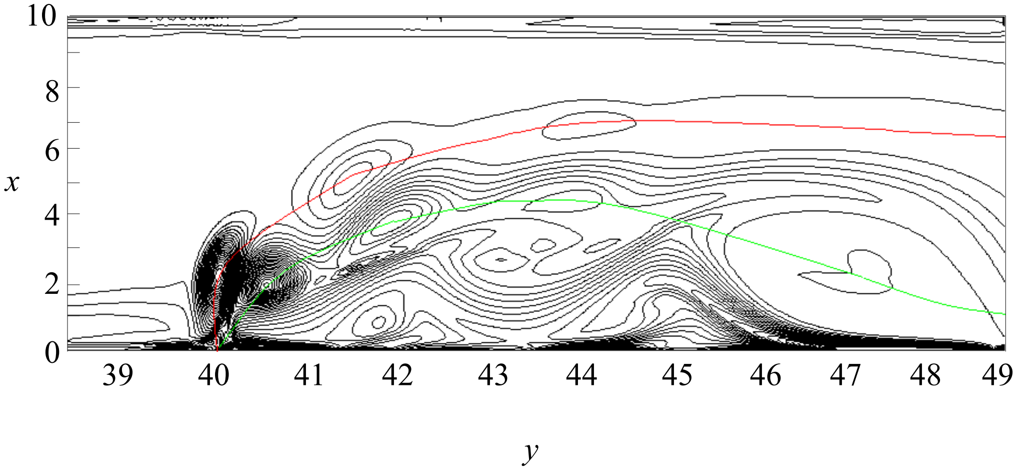

Fig. 8.8 Vorticity contours of a synthetic jet in a cross-flow indicating two vortex trajectories, *St* = 0.04

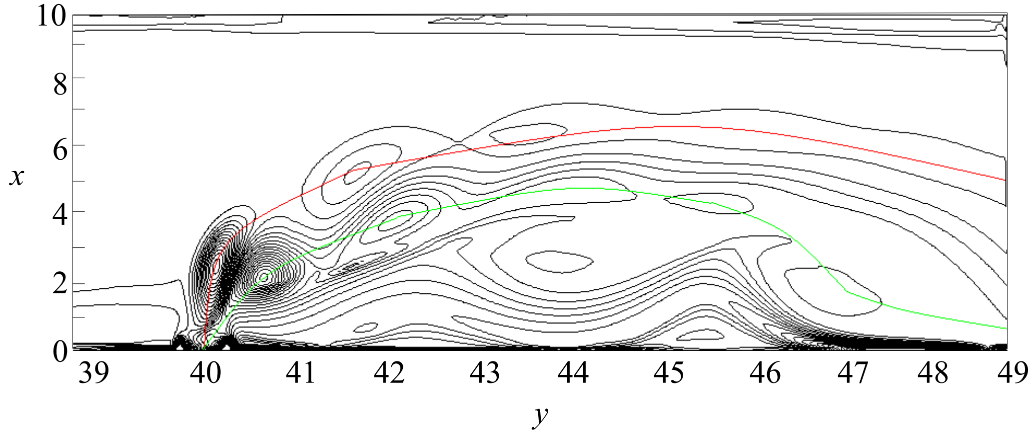

Fig. 8.9 Vorticity contours of a synthetic jet in a cross-flow indicating two vortex trajectories , *St* = 0.08.

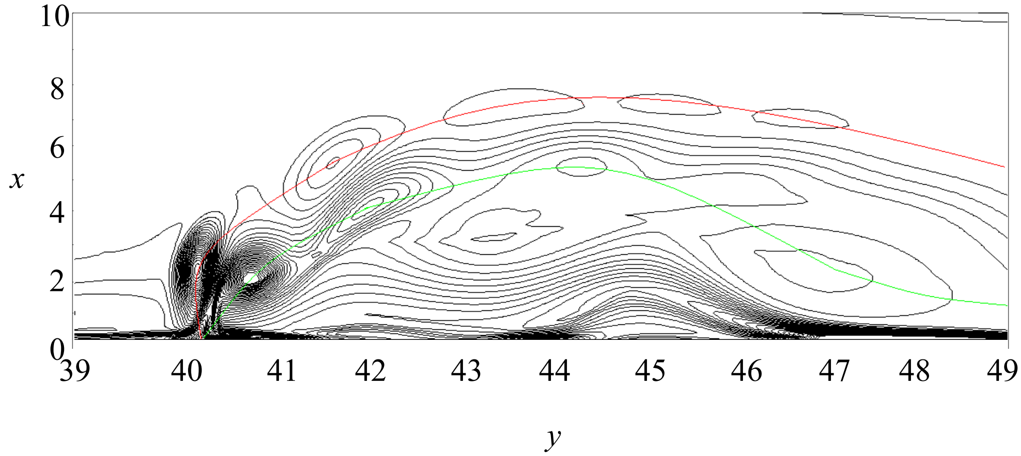

Fig. 8.10 Vorticity contours of a synthetic jet in a cross-flow indicating two vortex trajectories , *St* = 0.16.

8.5 DISCUSSION

The flow field associated with a synthetic jet actuator in both quiescent fluid and with an imposed cross-flow has been produced. In the case of the jet issuing into a cross-flow, the formation of a clearly definable vortex train does not occur above a cross-flow velocity of $v = 0.1u$. When the v velocity was increased to $v = 0.25u$, the vortex structures produced by the actuator were noted to travel less than five orifice diameters from the orifice. However when the cross-flow velocity is reduced to $v = 0.05u$ the vortices produced by the synthetic jet actuator can be noted to have an increased temporal longevity in comparison. In this case the vortex structures have sufficient strength and are not rapidly dissipated by the cross-flow. The vortices are distorted and carried away by the v component of velocity, however they remain persistent in the flow field up to a streamwise distance of $x = 15$. Experimental work on the effect of a cross-flow on a synthetic jet flow field, such as that carried out by Tomar *et. al*. [2004] has shown that a synthetic jet flow field can exist up to cross-flow velocities of $v = 0.5u$ at Reynolds numbers in the region of $Re = 2000$. This highlights a limitation of the numerical methods used in the current simulation work, particularly the limited Reynolds number of $Re = 300$. In low Reynolds number flows such as this dissipation plays a greater role than in practical high Reynolds number flows. Therefore, this increased dissipation can explain the lack of a true synthetic jet flow field at $Re = 300$ and $v > 0.05u$ as it will remove the smallest scales present in the flow field.

Although the synthetic jet does not form a true vortex train at these conditions, its application in the stabilisation of low-speed streaks is still possible. The vortex pair ejected from the jet orifice was noted to become distorted and begin to move in the cross-streamwise direction in proximity to the wall. As the jet leaves the orifice its *v* velocity component was noted to be lower than that of the background fluid. It is this generated region of low cross-streamwise velocity that yields the possibility of reducing the inflexional velocity profile associated with the unstable low-speed streaks. This has been shown in figure 8.5 – figure 8.7, where the application of the synthetic jet flow field in a cross-flow has been demonstrated. In the cases analysed the synthetic jet flow field was noted to cause a thinning of the cross-flow velocity component in the region close to the wall. It is suggested that modifying the type of unstable inflectional *v* velocity profile associated with the movement of low-speed streaks away from the wall with the velocity profile associated with the synthetic jet flow field will act to stabilise the streaks and thus delay flow transition. However, the possible formation of hairpin vortices by the secondary set of synthetic jet vortices also suggests a method by which with the correct control scheme, turbulence could be artificially triggered by a synthetic jet in regions prone to flow separation.

The effect of increasing the cross-flow velocity in relation to the streamwise jet flow has the effect of reducing the region of influence of the synthetic jet at low Reynolds number conditions. Therefore, although the synthetic jet can be determined to have an ability to influence the transition to turbulence, its effects at higher cross-flow velocities may be reduced.

CHAPTER 9

CONCLUSIONS & RECOMMENDATIONS

9.1 CONCLUSIONS

The optimisation of various input parameters of an axisymmetric synthetic jet actuator has been carried out, along with a study into the formation and evolution of the vortex train associated with synthetic jets. These results have then been directly compared with a fully three-dimensional synthetic jet case using the same input parameters as the axisymmetric case. Analysis of the mean centreline jet velocity at the orifice compared to data recorded at a downstream location has also shown the development of the positive streamwise momentum flux from the initial zero mass flux of the jet actuator at the domain inlet. The results attained have allowed a number of assertions to be made about the input characteristics which yield the optimal streamwise vortex train in terms of vortex strength, momentum flux and longevity.

Throughout the range of physical parameters examined, various vortex structures have been observed in the flow field. The input parameter which was noted to have the greatest effect on jet formation in a quiescent fluid was the actuator oscillation frequency. At low actuation frequencies the vortex structures present in the flow field were of a larger size; however a true ‘vortex train’ was not produced as the vortex structures travel downstream as a lone vortex ring. At high frequencies the jet was under expanded in the region near the actuator. In this case vortex structures in the flow field were less coherent and did not persist in the downstream region due to re-ingestion of the expelled fluid from the actuator on the subsequent suction stroke. Both the high frequency and low frequency cases displayed a lower magnitude momentum flux compared to the optimal case, which had an actuation frequency of $St = 0.08$. The results also showed that synthetic jets with zero mass flow at the orifice behave in a significantly different manner from jets with non-zero mass flow. For a synthetic jet with a zero mean velocity at the inlet, the jet developed significant vortex structures at much lower frequencies than other forms of non-zero mean velocity jets such as continuous or pulsed jets.

Analysis of the evolution of the optimised jet case at regular time intervals shows the initial development and propagation of the individual vortex rings which make up the fully developed synthetic jet. The jet was defined as being fully developed at a time when increasing the overall run time simulation will result in no further downstream propagation of the vortex structures present in the flow. The jet evolution study showed that in the optimised case, the jet could be defined as fully developed beyond $t = 60$.

Through the comparative studies of the axisymmetric and three-dimensional cases, it can be noted that beyond the flow field region immediately adjacent to the jet orifice, the vortex structures present in the flow field vary greatly. The three-dimensional jet flow field, as was expected showed a high degree of asymmetry around the jet centreline. The intensity of the vortex structures in the downstream region was far greater in the three-dimensional case. Vortex structures were present in the flow of the three-dimensional case beyond the point that the axisymmetric case had predicted that the jet flow had reduced to almost the level of the background fluid. This was due to the spanwise mixing of the fluid sustaining the vortex train in the 3*D* case.

The axisymmetric case also predicted a different streamwise location for the second vortex structure compared to the 3*D* case. Analysis of jet perturbation applied to the 3*D* case suggests that it is this imposed asymmetry that is the cause of the different streamwise location of this vortex structure. This finding highlights the importance of breaking the flow symmetry at the jet inlet. This is in order to correctly predict causes of asymmetry in experimental synthetic jet actuators caused by influences such as manufacturing tolerances. This also suggests that the focus of 3*D* synthetic jet CFD simulations should be on a method of accurately breaking the flow symmetry at the jet orifice, and not modelling the full actuator orifice. Downstream of the second vortex structure, the axisymmetric and 3*D* cases were in general agreement, however the 3*D* case featured a slightly higher magnitude of streamwise velocity.

Analysis of a 2*D* synthetic jet in a cross-flow showed the deformation of the vortex structures in the presence of varying levels of cross-stream velocity. However, a region of fluid with a low cross-streamwise component of velocity was formed adjacent to the orifice of the synthetic jet. This suggests a potential application of synthetic jets in the control of low-speed streaks. The vortex pairs of the synthetic jet were identified as the possible source of the secondary jet trajectory as noted in previous studies on synthetic jets. However, in all the low Reynolds number cases of synthetic jets operating in a cross-flow analysed in this thesis the cross-flow velocity was much lower than the jet centreline velocity. The effect of the synthetic jet flow field on the cross-stream velocity was reduced as the cross-stream velocity was increased. This suggests that 'real life' full scale applications operating at aircraft type velocities, would require a jet centreline velocity beyond what is capable of current actuator designs.

9.2 RECOMMENDATIONS FOR FURTHER WORK

9.2.1 IMPROVED ACTUATOR MODELLING

For all the cases analysed in this thesis the synthetic jet actuator was simplified by modelling it as an oscillating velocity profile. In practice this velocity profile closely matches the velocity profile present at the orifice of a complete synthetic jet actuator. However, it was established that several modifications could be made to the model. Firstly, that the actuator diaphragm could be modelled completely. The governing equations for the jet actuator should be determined and applied in order to accurately model a full actuator diaphragm and cavity. If this information can be calculated using an accurate model, and combined with a modified fluid domain to represent the cavity and orifice of the actuator, a more detailed study of the formation criterion would be possible. In this case analysis of the diaphragm, cavity dimensions and volume along with the actuator frequency and amplitude would be possible. This would also allow for a direct comparison between the imposed velocity profile used in this thesis and a full cavity model, with the aim of proving that the imposed top-hat velocity profile is an accurate representation of the flow at the jet orifice.

9.2.2 OTHER TYPES OF FLOW CONTROL ACTUATOR

Comparisons and evaluations of jet formation using various different types of jet actuator could be carried out with the same DNS code in order to investigate other types of flow control device. Devices such as micro-valves or continuous jets, could be modelled by a minimal adaptation of the current techniques. If used in conjunction with a boundary layer model, further comparisons could be drawn from the modelling of surface elements, such as bumps and ridges.

9.2.3 PARAMETRIC STUDY ON PERTURBATION EFFECTS

In this thesis a perturbation was added to the $3D$ synthetic jet flow field in order to break the symmetry associated with the top-hat input velocity profile used. It was found that this perturbation had a large effect on the synthetic jet flow field and the formation of a vortex train. Analysis into varying the frequency of this perturbation further highlighted its large effect on the flow field.

Previous computational work on synthetic jets has largely concentrated on the effects of the design of the jet cavity on the flow field. The flow field produced at the orifice by these computational models is largely $2d$ and is comparable to the top-hat velocity profile used in this thesis. However, experimental models have been noted not to share this two-dimensionality at the orifice due to effects caused by surface roughness and other disturbances. These disturbances are suggested to have a greater effect on the evolution of a synthetic jet flow field than the design of the cavity itself. It is therefore suggested to perform a parametric study into the effect introducing varying levels of disturbance to the synthetic jet flow field, with focus concentrated on applying surface roughness at the jet orifice.

9.2.4 SUITABILITY OF SYNTHETIC JETS

The limitation of synthetic jets in terms of the jet centreline velocity required to form a true vortex train at low Reynolds numbers and in the presence of a cross-flow has been highlighted. In this thesis, the cross-stream velocity was not increased beyond 25% of the jet centreline velocity due computational limitations.

Further uses of synthetic jets in flow control consist of applying a synthetic jet to an artificially generated low-speed streak. It is suggested to carry out this analysis at a range of jet centre-line velocities in order to directly analyse the possible use of synthetic jets in stabilising these low-speed streaks.

BIBLIOGRAPHY

Acarlar, M. S. & Smith, C. R., “A study of hairpin vortices in a laminar boundary layer. Part 2. Hairpin vortices generated by fluid injection,” *J. Fluid Mech.*, Vol. 175, 1987, pp. 43–83.

Anderson, J.D.: *Computational Fluid Dynamics*. *The Basics with Applications*. McGraw-Hill, 1995.

Braslow, A. L., “A History of suction-type laminar-flow control with emphasis on flight research,” NASA History Division, Monographs in Aerospace History, No. 13, 1999.

Carlson, H. A., & Lumley, J. L., “Flow over an obstacle emerging from the wall of a channel,” *AIAA,* 0001-1452, Vol.34 no.5, 1996, pp. 924-931.
doi: 10.2514/3.13169

Catalano, P., Wang, M., Iaccarino, G., Sbalzarin, I. F., & Koumoutsakos, P., “Optimization of cylinder flow control via actuators with zero-net mass flux,” *Centre for Turbulence Research, Proceedings of the Summer Program 2002*. pp. 297 – 303, 2002.

Cater, J. E. & Soria, J., “The Evolution of Round Zero-Net-Mass-Flux Jets,” *J. Fluid Mech.*, Vol. 472, Dec. 2002, pp. 167-200.
doi:10.1017/S0022112002002264

Cattafesta, L., Mathew, J., & Kurdila, A., “Modeling and Design of Piezoelectric Actuators for Fluid Control,” *World Aviation Conference*, San Diego, CA, October 2000.

Choi, H., Moin, P. & Kim, J., “Active turbulence control for drag reduction in wall – bounded flows*,”* *J. Fluid Mech.*, Vol. 262, 1994, pp. 75-110.

Choudhari, M. & Kerschen, E. J. “Instability-wave patterns generated by interaction of sound waves with three-dimensional wall suction or roughness.” *AIAA Paper* 1990-0119, 28th *Aerospace Sciences Meeting and Exhibit*, Reno, NV, Jan. 8-11, 1990, 11 p.

Conte, S.D. and deBoor, C.: *Elementary Numerical Analysis*. McGraw-Hill, 1972.

Cui J. & Agarwal R. K., “Three-dimensional computation of a synthetic jet in quiescent air,” *AIAA Paper,* 0001-1452, Vol. 44, no. 12, Dec. 2006, pp. 2857-2865.
doi:10.2514/1.14213

Danaila, I., Boersma, B.J., “Direct numerical simulation of bifurcating jets,” *Phys. Fluids,* Vol. 12, Issue 5, 2000, pp. 1255-1257.
doi:10.1063/1.870377

Dandois, J., Garnier, E., & Sagaut, P., "Numerical simulation of active separation control by a synthetic jet," *J. Fluid Mech.,* Vol. 574, 2007, pp 25-58.
doi:10.1017/S0022112006003995

Doligalski, T. L., Smith, C. R. & Walker, J. D. A., "Production mechanism for turbulent boundary-layer flows," *Viscous flow drag reduction; Symposium, Dallas, Texas ;* 7-8 1979. pp. 47-72. 1980.

Farrell, B. F, & Loannou, P. J., "Turbulence suppression by active control," *Phys. Fluids*, Vol. 8, no. 5, pp1257-1268.

Fugal, S.R., Smith, B.L, & Spall, R.E., "Displacement amplitude scaling of a two-dimensional Synthetic Jet," *Phys. Fluids,* Vol. 17, Issue 4, 2005, 045103.
doi:10.1063/1.1872092

Gad-El-Hak, M. & Blackwelder, R. F. "Selective suction for controlling bursting events in a boundarylayer," *AIAA. J.*0001-1452, Vol.27, no.3, 1989, pp. 308-314.
doi: 10.2514/3.10113

Gad-el-Hak, M. & Hussain, A. K. M. F., "Coherent structures in a turbulent boundary Layer, Part I: Generation of Artificial Bursts," *Phys. Fluids*, Vol. 29, pp. 2124-2139.

Glezer A. & Amitay M., “Synthetic jets,” *Annu. Rev. Fluid Mech.,* Vol. 34, 2002, pp. 503-529.

Goldstein, M. E. & Hultgren L. S., “Boundary layer receptivity to long wave free stream disturbances,” *Ann. Rev. Fluid Mech*. Vol. 21, 1989, pp. 137 -166.

Ho, C-M, & Tai, Y-C., “REVIEW: MEMS and Its Applications for Flow Control,” *Fluids Engineering*, Vol. 118, Issue 3,1996, pp. 437-448.
doi:10.1115/1.2817778

Hon T. L., & Walker, J. D. A., “Evolution of hairpin vortices in a shear flow,” *Computers and Fluids*, Vol. 20, no. 3, 1991, pp. 343–358.

Hon, T. L. & Walker, J. D., “An Analysis of the Motion and Effects of Hairpin Vortices,” *Interim rept. Jul 85-Jul 87*, *Leigh University Bethlehem, Pa. Dept. of Mechanical Engineering and Mechnics.* 1987.

Jacobson, S. A. & Reynolds, W. C., “Active control of streamwise vortices and streaks in boundary layers,” *J. Fluid Mech.,* Vol. 360, 1998, pp. 179–211.

Jiang, X., Zhao, H., & Cao, L., “Numerical simulations of the flow and sound fields of a heated axisymmetric pulsating jet,” *Computers & Mathematics with Applications,* Vol. 51, Issues3-4, 2006, pp. 643-660.
doi:10.1016/j.camwa.2005.03.022

Jiang, X. & Luo, K.H., "Direct numerical simulation of the puffing phenomenon of an axisymmetric thermal plume," *Theoretical and Computational Fluid Dynamics,* Vol.14, 2000, pp. 55-74.

Jiang, X., Avital, E.J. & Luo, K.H., "Sound generation by vortex pairing in subsonic axisymmetric jets," *AIAA J.,* Vol. 42, 2004, pp. 241-248.

Kim, H.T., Kline, S.J. & Reynolds, W.C., "The production of turbulence near a smooth wall in a turbulent boundary layer," *J. Fluid Mech.*, Vol. 50, no. 1, 1971, pp. 133-160.

King, R., & Breuer, S., "Acoustic receptivity of a Blasius boundary layer with 2-D and oblique surface waviness," *Fluids 2000 Conference and Exhibit*, Denver, CO; UNITED STATES; 19-22 June 2000.

Kline, S.J. & Reynolds, W. C., "The structure of turbulent boundary layers," *J. Fluid Mech.*, Vol 30, part 4, 1967, pp. 741-773.

Kotapati, R., Mittal, R., & Cattafesta, L., "Numerical study of a transitional synthetic jet in quiescent external flow," *J. Fluid Mech*. Vol 581, pp. 287-321.
doi:10.1017/S0022112007005642

Koumoutsakos, P., “Active control of vortex–wall interactions,” *Phys. Fluids,* Vol. 9, Issue 12, 1997, pp. 3808.
doi:10.1063/1.869515

Kral, L. D., Donovan, J. F., Cain, A. B. & Cary, A. W., “Numerical simulation of synthetic jet actuators*,” AIAA Paper,* 97-1824, 1997.

Lele, S. K., “Compact finite-difference schemes with spectral-like resolution, *J. Comput. Phys.*, Vol. 103, 1992, pp. 16-42.

Luo, K.H. & Sandham, N.D, “Direct numerical simulation of supersonic jet flow.” *J. Eng. Mathematics* **32**, 121-142, 1997.

Meissner, A., “Uber piezo-elektrische kristalle bei hoch-frequenz*,” Z. Tekh. Fiz. 7,* 1926, p. 585.

Offen, G. R., & Kline, S. J., “A proposed model of the bursting process in turbulent boundary layers,” *J. Fluid Mech.*, Vol. 70, no. 2, 1975, pp. 209-228.

Orlandi, P. & Jimienez, J. “On the generation of turbulent wall friction,”*Phys. Fluids,* Vol. 6*,* 1994, pp. 634–641.

Poinsot, T. J., & Lele, S. K., Boundary Conditions for Direct Computations of Compressible Viscous Flows, *J. Comput. Phys.*, vol. 101, pp. 104-129, 1992.

Rathnasingham, R. & Breuer, K. S., "Active control of turbulent boundary layers," *J. Fluid Mech.*. Vol. 495, 2003, pp. 209-233.
doi:10.1017/S0022112003006177

Rathnasingham, R. & Breuer, K. S., "System identification and control of turbulent flows," *Phys. Fluids*, vol. 9, no. 7, 1997, pp. 1867-1986.

Ravi, B. R., Mittal, R. & Najjar, F. M., "Study of three-dimensional synthetic jet flowfields using direct numerical simulation," *AIAA Paper 2004-0091, Aerospace Sciences Meeting and Exhibit, 42nd, Reno, NV,* Jan. 5-8, 2004.

Ritchie, B. D., Mujumdar D. R. & Seitzman J. M., "Mixing in coaxial jets using synthetic jet actuators," *AIAA Paper 2000-0404, Aerospace Sciences Meeting and Exhibit, 38th, Reno, NV*, Jan. 10-13, 2000.

Rizzetta, D. P., Visbal, M. R. & Stanek, M. J., "Numerical investigation of synthetic-jet flowfields," *AIAA J.* 0001-1452, vol.37, no.8, 1999, pp. 919-927.
doi: 10.2514/2.811

Robert, J.P., “Drag reduction : an industrial challenge,” AGARD Report 786, March, 1992.

Romano, G. P., “PIV and LDA velocity measurements near walls and in the wake of a delta wing”, *Optics and Lasers in Engineering,* Vol. 16, Issues 4-5, 1992, pp. 293-309.

Rumsey, L. C., “Proceedings of the 2004 Workshop on CFD Validation of Synthetic Jets and Turbulent Separation Control,” NASA/CP-2007-214874, 2007.

Rupesh, K-A. B., Ravi, B. R., Mittal, R., Raju, R., Gallas, Q., & Cattafesta, L., “Proceedings of the 2004 workshop on CFD validation of synthetic jets and turbulent separation control – Case 1: Time-accurate numerical simulations of synthetic jets in quiescent air,” NASA/CP-2007-214874, pp. 1.9.1 - 1.9.5, 2007.

Sandham, N.D. & Reynolds, W.C., “A numerical investigation of the compressible mixing layer.” Report No: TF-45, Stanford University, 1989.

Schoppa, W., & Hussain, F., “Coherent structure dynamics in near-wall turbulence,” *Fluid Dynamics Research*. Vol. 26, Issue 2, Feb. 2000, pp. 119-139.
doi: 10.1016/S0169-5983(99)00018-0

Smith C. R. & Walker J. D. A., “Sustaining mechanisms of turbulent boundary layers - The role of vortex development and interactions,” *AIAA Paper*-1998-2959, *Fluid Dynamics Conference, 29th, Albuquerque, NM*, June 15-18, 1998.

Smith, B. L. & Glezer, A., “Jet vectoring using synthetic jets,” *J. Fluid Mech*. Vol. 458, 2002, pp. 1-34.
doi:10.1017/S0022112001007406

Smith, B., & Glezer, A., “Vectoring of adjacent synthetic jets,” *AIAA, J.* 0001-1452, Vol.43 no.10, 2005, pp. 2117-2124.
doi: 10.2514/1.12910

Smith, C.R, Walker, J.D.A, Haidairi, A.H & Sobrun, U., “On the dynamics of near-wall turbulence,” *Philosophical Transactions: Turbulent Flow Structure near Walls*. Part II, Aug. 15, 1991, pp. 131-175.

Smith, J. H. B., “Theoretical modelling of three-dimensional vortex flows in aerodynamics,” *Royal Aero. Soc. J.*, Vol. 88, no. 874, 1984, pp. 101-116.

Subhasish D. & Tushar K. N., “Turbulence characteristics in flows subjected to boundary injection and suction,” *J. Engrg. Mech.,* Vol. 136, Issue 7, 2010, pp. 877-888

Swearingen, J. D & Blackwelder, R. F., “The growth and breakdown of streamwise vortices in the presence of a wall,” *J. Fluid Mech.,* Vol. 182, 1987, pp. 255-290.

Tang, H. & Zhong, S., “2D numerical study of circular synthetic jets in quiescent flows,” *The Aeronautical Journal,* Vol. 109, Feb 2005, pp. 89-97.

Tomar S. Arnaud J. & Soria J., “Structure of a zero-net-mass-flux round jet in crossflow,” *15th Australasian Fluid Mechanics Conference.* Dec 2004.

Uchiyama, T., “Three-dimensional vortex simulation of bubble dispersion in excited round jet,” *Chemical Engineering Science,* Vol. 59, 2004, pp. 1403-141. doi:10.1016/j.ces.2003.12.024

Uttukar, Y., Holman, R., Mittal, B. Carroll, M. Sheplak, & L. Cattafesta, A., “Jet formation criterion for synthetic jet actuators,”*AIAA paper,* 2003-636, *41st Aerospace Sciences Meeting and Exhibit, Reno, Nevada,* Jan. 6-9 2003.

Warhaft, Z.,”The engine and the atmosphere: An introduction to thermal-fluid engineering,” *Cambridge University Press,* 1997, pp68-70. ISBN: 0521581001.

Williamson, J. H., Low-storage Runge-Kutta schemes, *J. Comp. Phys*., Vol. 35, pp. 48-56, 1980.

Williamson, J.H.: Low-storage Runge-Kutta schemes. *J. Comp. Physics* 35, 1-24, 1980.

Wray, A.A.: Very low storage time-advancement schemes. *Internal Report, NASA Ames Research Center,* Moffett Field, California, 1986.

Wũrz, W., Herr, S., Wōrner, A., Rist, U., Wagner, S. & Kachanov, Y. S., "Three-dimensional acoustic-roughness receptivity of a boundary layer on an airfoil: experiment and direct numerical simulations," *J. Fluid Mech.*, Vol. 478, 2003, pp. 135-163. doi:10.1017/S0022112002003348

Yang W., Meng H, & Sheng J., "Dynamics of hairpin vortices generated by a mixing tab in a channel flow," *Experiments in Fluids.,* Vol. 30, 2001, pp705-722.

Zhong S., Millet F. & Wood N.J., "The behaviour of circular synthetic jets in a laminar boundary layer," *The Aeronautical Journal,* Paper no. 2980, 2005, pp461-470.